Magnetic imaging of domain wall structure and dynamics in nanotubes

Mahdi Jaber

THÈSE

Pour obtenir le grade de

DOCTEUR DE L'UNIVERSITÉ GRENOBLE ALPES

École doctorale : PHYS - Physique
Spécialité : Nanophysique
Unité de recherche : Spintronique et Technologie des Composants

Imagerie magnétique de la structure et de la dynamique de parois dans les nanotubes magnétiques

Magnetic imaging of domain wall structure and dynamics in nanotubes

Présentée par :

Mahdi JABER

Direction de thèse :

Aurélien MASSEBOEUF CHARGE DE RECHERCHE HDR, CNRS DELEGATION ALPES	Directeur de thèse
Olivier FRUCHART DIRECTEUR DE RECHERCHE, CNRS DELEGATION ALPES	Co-directeur de thèse

Rapporteurs :

DANIEL LACOUR
DIRECTEUR DE RECHERCHE, CNRS DELEGATION CENTRE-EST
CHRISTOPHE GATEL
MAITRE DE CONFERENCES HDR, UNIVERSITE TOULOUSE III - PAUL SABATIER

Thèse soutenue publiquement le **7 décembre 2023**, devant le jury composé de :

MARTIEN DEN HERTOG, DIRECTRICE DE RECHERCHE, CNRS DELEGATION ALPES	Présidente
DANIEL LACOUR, DIRECTEUR DE RECHERCHE, CNRS DELEGATION CENTRE-EST	Rapporteur
CHRISTOPHE GATEL, MAITRE DE CONFERENCES HDR, UNIVERSITE TOULOUSE III - PAUL SABATIER	Rapporteur
SYLVIE BEGIN-COLIN, PROFESSEURE DES UNIVERSITES, UNIVERSITE DE STRASBOURG	Examinatrice
LAURENT RANNO, MAITRE DE CONFERENCES HDR, UNIVERSITE GRENOBLE ALPES	Examinateur

Abstract

Ferromagnetic nanotubes are emerging as potential components for domain-wall (DW) based solid-state, low-power memory devices. This field of study, more broadly part of 3D nanomagnetism, is gaining attention due to the discovery of new topologies and curvature-induced phenomena. Our research primarily addresses cylindrical nanotubes, which represent an interesting interplay between curvature effects and core-shell interfaces conducive to spintronic applications. Our focus lies in examining the azimuthal curling of magnetisation, a result of curvature-induced magneto-elastic anisotropy, leading to a low stray field for applications and non-reciprocal spin wave propagation from an academic standpoint.

We have used CoNiB nanotubes via electroless plating in ion-track-etched polycarbonate templates. The tube dimensions range from 160 to 500 nm in diameter, 20 to 80 nm in wall thickness, and span several tens of micrometres in length. Post template dissolution, nanotubes were characterized using Transmission Electron Microscopy (TEM) and Focused Ion Beam (FIB) methods. The structural analysis indicated good consistency in diameter and tube thickness, with minor variations at the tube edges, an expected feature due to diffusion limitations during synthesis. Energy-dispersive X-ray spectroscopy (EDX) and Electron energy-loss spectroscopy (EELS) revealed a gradient in the CoNi composition across the tube thickness. Nickel was found to be more concentrated near the tube surfaces, while the Cobalt content was comparatively lower near the inner surface. This non-homogeneity across the tube wall may induce varied magnetic properties, as observed in some thin films.

The nanotube wall thickness introduces an additional degree of freedom compared to nanowires that only rely on diameters. Consequently, controlling wall thickness can be a significant parameter in adjusting their properties. We have tested and benchmarked multiple electron microscopy methods to measure the wall thickness accurately.

Magnetic flux mapping and quantification during magnetic reversal were conducted using electron holography. This analysis confirmed azimuthal domains in the remanent state, with a 35 mT field required for axial magnetisation of the tube. The application of smaller fields (2-10 mT) triggered DW transformations, motion, and partial magnetisation rotation along the nanotube axis. The nature and width of the domain walls were experimentally determined and cross-verified using micromagnetic modelling translated into phase images. Essential parameters were further extracted using analytical models.

This thesis provides the foundational groundwork for future studies on DW dynamics and spin-wave propagation. It also contributes to the conceptual development of racetrack memories that would operate by shifting magnetic domain walls in nanotubes.

Résumé

Les nanotubes ferromagnétiques pourraient être utilisés dans des composants pour des mémoires basés sur des paroi de domaines magnétiques (DW), consommant peu d'énergie. Ce champ d'étude se positionne dans le domaine plus large du nanomagnétisme 3D, qui gagne en attention grâce à la découverte de nouvelles topologies et de phénomènes induits par la courbure. Notre recherche aborde principalement les nanotubes cylindriques, qui présentent une assosciation intéressante entre les effets de courbure et les interfaces cœur-coquille propices aux applications spintroniques. Nous nous concentrons sur l'examen du curling azimutal de l'aimantation, un résultat de l'anisotropie magnéto-élastique induite par la courbure. Ce curling permettrait d'éviter les champs de fuite dans le cadre d'applications mémoire denses, et en terme de physique devrait conduire à des effets dynamiques non-réciproques des ondes de spin.

Nous utilisons des nanotubes CoNiB produits par dépôt electroless dans des membranes en polycarbonate gravées par faisceau d'ions. Les dimensions des tubes varient de 160 à 500 nm de diamètre, de 20 à 80 nm d'épaisseur de paroi, et s'étendent sur plusieurs dizaines de micromètres en longueur. Après dissolution de la membrane, les nanotubes ont été caractérisés en utilisant la microscopie électronique à transmission (TEM) et des méthodes de faisceau d'ions focalisés (FIB). L'analyse structurelle a indiqué une bonne uniformité en diamètre et épaisseur du tube, avec néanmoins de légères variations aux extrémités du tube, une caractéristique attendue en raison des limitations de diffusion lors de la synthèse. La spectroscopie de rayons X à dispersion d'énergie (EDX) et la spectroscopie de perte d'énergie d'électrons (EELS) ont révélé un gradient dans la composition CoNi à travers l'épaisseur du tube. Le nickel a été trouvé plus concentré près des surfaces du tube, tandis que le contenu en cobalt était comparativement plus bas près de la surface intérieure. Cette non-homogénéité à travers l'épaisseur du tube peut induire des propriétés magnétiques variées, comme observé dans certains films minces.

L'épaisseur du nanotube introduit un degré de liberté supplémentaire par rapport aux nanofils qui ne reposent que sur des diamètres. Par conséquent, le contrôle de l'épaisseur de la paroi peut être un paramètre significatif pour ajuster leurs propriétés. Nous avons testé et établi une comparaison de plusieurs méthodes de microscopie électronique pour mesurer avec précision cette dimension cruciale.

La cartographie et la quantification du flux magnétique lors du renversement d'aimantation ont été réalisées en utilisant l'holographie électronique. Cette analyse a confirmé l'existence de domaines azimutaux dans l'état rémanent, avec un champ de 35 mT nécessaire pour établir l'aimantation dans la direction axiale du tube. L'application de champs plus petits (2-10 mT) a déclenché des transformations de parois, le mouvement, et une rotation partielle de l'aimantation le long de l'axe du nanotube. La nature et la largeur des parois de domaine ont été déterminées expérimentalement et vérifiées en utilisant des modèles micromagnétiques traduits en images de phase. Des paramètres essentiels ont été en outre extraits en utilisant des modèles analytiques.

Cette thèse fournit les bases pour les futures études sur la dynamique de DW et la propagation des ondes de spin. Elle contribue également au développement conceptuel des mémoires à registre qui fonctionneraient en déplaçant les parois de domaine magnétique dans les nanotubes.

Acknowledgements

First, I would like to express my profound gratitude to my thesis supervisors, Dr. Aurélien Masseboeuf and Dr. Olivier Fruchart, for their continuous support and guidance throughout my research. Your mentorship was paramount in providing a well-rounded and in-depth learning experience. Your insightful feedback pushed me to sharpen my thinking and brought my work to a higher level.
I would like to thank my academic committee members for their valuable comments and suggestions. Their criticisms and encouragement were essential to the completion of this research study.
Thanks also to the doctoral school of physics, and I extend my gratitude to the University of Grenoble Alpes for providing an excellent academic environment and resources that greatly contributed to my research.
I am deeply grateful to the Spin Textures Team at SPINTEC and NÉEL institutes and the LEMMA team at PFNC. Their hard work and expertise have been vital to my research. I admire their commitment to advancing our field. I also want to thank all staff and colleagues at the SPINTEC and PFNC labs. The cooperative atmosphere and their willingness to share knowledge greatly helped my work.
I sincerely thank our colleagues in Darmstadt and Erlangen, Germany. Their work on sample fabrication has significantly enriched our research, and your support has been vital.
I'm thankful to our colleagues at the Centre d'Elaboration de Matériaux et d'Etudes Structurales (CEMES) in Toulouse, France. Their collaboration has greatly benefited this work. A special thanks to Dr. Christophe Gatel, who provided essential software for our research.
Lastly, I want to recognize the financial support from the French Alternative Energies and Atomic Energy Commission (CEA) and the French National Centre for Scientific Research (CNRS). Their funding was key to conducting this research.
A special word of thanks goes to my family, who have given me their unequivocal support, both emotionally and materially. To my parents, I am eternally grateful for your love and faith in me.
Finally, I wish to thank my friends who supported me during this process. Their companionship, patience, and understanding were a consistent source of strength and helped me overcome many challenging times.
This work would not have been possible without all of you. Your support and encouragement have played a crucial role in my journey, and for that, I am deeply grateful.
Thank you.

Contents

Abstract i

Résumé iii

Acknowledgements v

1 Introduction 1
1.1 Introduction (English) . . . 1
1.2 Introduction (Français) . . . 4

2 Theoretical background and state of the art 9
2.1 Ferromagnetic nanotubes . . . 9
2.1.1 Geometry and application benefits . . . 9
2.1.2 Magnetic configurations in nanotubes . . . 10
2.1.2.1 Magnetic textures and magnetisation phase diagram . . . 11
2.1.2.2 End-Vortex Domains and Mixed State in Nanotubes . . . 12
2.1.2.3 Azimuthal domains in nanotubes . . . 13
2.1.2.4 Domain walls in nanotubes . . . 15
2.1.3 Theoretical and experimental advances in nanotubes . . . 18
2.1.4 Nanotubes synthesis and materials . . . 20
2.1.4.1 Electroless plating deposition . . . 20

3 Methods and instrumentation 23
3.1 Transmission Electron Microscopy . . . 23
3.1.1 Scanning Transmission Electron Microscopy (STEM) . . . 25
3.1.1.1 Energy Dispersive X-Ray Analysis (EDX) . . . 25
3.1.1.2 Electron energy-loss spectroscopy (EELS) . . . 25
3.1.2 Magnetic imaging in TEM . . . 27
3.1.3 Electron holography . . . 28
3.1.3.1 Off-axis electron holography . . . 28
3.1.3.2 Phase reconstruction . . . 29
3.1.3.3 Separation of phase contributions . . . 31
3.2 Scanning transmission X-ray microscopy (STXM) . . . 31
3.3 Sample preparation for TEM . . . 34
3.3.1 Dissolving of the nanotube membranes . . . 34
3.3.2 Focused Ion Beam (FIB) fabrication . . . 34

4 Structural and chemical analysis of nanotubes **37**
4.1 Introduction . . . 37
4.2 TEM-Based Methods for Assessing Thickness . . . 38
4.2.1 The image-contrast method by TEM . . . 39
4.2.2 The Log-ratio method by EELS . . . 39
4.2.3 Electron Holography . . . 41
4.2.4 Defining the integrated thickness . . . 42
4.3 Results and discussion . . . 44
4.3.1 Ferromagnetic Nanotubes . . . 44
4.3.2 Chemical analysis by STEM-EDX and STEM-EELS . . . 47
4.3.3 Thickness measurement and discussions . . . 50
4.4 Determination of important parameters for a known material thickness . . . 55
4.4.1 MIP of polycrystalline samples . . . 55
4.4.2 Density (composition) of a known sample thickness . . . 56
4.5 Conclusion . . . 57

5 Magnetic imaging of CoNiB ferromagnetic nanotubes **59**
5.1 Magnetic imaging of nanotubes . . . 59
5.2 STXM imaging of CoNiB nanotubes . . . 62
5.2.1 Analytical models of XAS and XMCD imaging . . . 62
5.2.1.1 STXM profile of nanotubes with azimuthal domains . . . 62
5.2.1.2 XAS profile of nanotubes . . . 62
5.2.1.3 XMCD profile of nanotubes . . . 65
5.2.2 Experimental STXM of CoNiB nanotubes with azimuthal domains . . . 66
5.3 TEM magnetic imaging of CoNiB nanotubes . . . 68
5.3.1 Analytical model of Magnetic phase profile of nanotube with axial magnetisation . . . 68
5.3.2 Magnetic phase shift: unwrapping and the cosine displays . . . 71
5.3.3 Examples of electron holography measurements . . . 72
5.4 Electron holography experiments on nanotubes under fields . . . 74
5.4.1 Electron holography of CoNiB thin nanotubes: from azimuthal to mixed state 74
5.4.2 Domain walls: First experimental evidence by electron holography . . . 76
5.4.3 Domain wall type and width . . . 78
5.5 Conclusion and outlook . . . 80

6 General conclusion and perspectives **83**
6.1 General conclusion and perspectives (English) . . . 83
6.1.1 Conclusion . . . 83
6.1.2 Perspectives . . . 84
6.2 Conclusion générale et perspectives (Français) . . . 85
6.2.1 Conclusion . . . 85
6.2.2 Perspectives . . . 86

A The calculation of the density of materials **87**
A.1 Appendix A: Density Calculation of CoNiB Nanotubes . . . 87

B The calculation of the XAS profile function 89

Chapter 1

Introduction

1.1 Introduction (English)

Traditional digital data storage has depended on magnetic hard disk drives (HDDs) and electronic flash memory, such as solid-state drives (SSDs), to handle the vast amount of worldwide data. A primary goal in advancing data storage technologies is to increase areal storage density by minimizing component sizes down to the nanoscale. This objective addresses several crucial factors, including fulfilling the growing demand for data storage capacity, enhancing cost efficiency for better accessibility and affordability, improving energy efficiency to reduce power consumption and environmental impact, increasing speed and performance through shorter signal paths for quicker data access and transfer, and facilitating more portable and compact device designs using smaller components. One major concern is power dissipation, which can lead to increased energy consumption and potential device failure due to overheating. Additionally, these devices face challenges in scaling beyond certain dimensions, limiting their performance and further miniaturization. Charge-based memory devices, such as dynamic random access memory (DRAM), also require continuous refresh cycles to maintain stored data, which can be energy-intensive and negatively affect device reliability. As a result, researchers explore alternative approaches like spintronics to address these limitations and develop more efficient and versatile nanoscale devices.
Spintronics is a research area that harnesses both the electrical properties and the spin of electrons, providing an additional degree of freedom for potential devices. The nanoscale spintronic is particularly significant due to its inclusion of characteristic lengths of magnetism, like magnetic domain wall sizes. The discovery of the giant magnetoresistance (GMR) effect in 1986 pioneered spintronics [1] and several other phenomena, such as tunnelling magnetoresistance (TMR) [2], spin-transfer torque (STT) [3], spin Hall effect (SHE) [4, 5], and spin Seebeck effect (SSE) [6], have since emerged and contributed substantially to advancements in fast, low-power consumption magnetic memory applications. These phenomena have enabled the development of various energy-efficient and scalable memory technologies, including magnetic random access memory (MRAM), spin-transfer torque MRAM (STT-MRAM), and spin-orbit torque MRAM (SOT-MRAM), as well as potential applications in thermally driven spintronic devices and energy harvesting. In 2004, Parkin et al. introduced an innovative concept for a non-volatile magnetic device called racetrack memory [7]. This design encodes information as magnetic domains separated by domain walls in cylindrical nanowires, which can be moved using an electric current. The wires are vertically arranged in a large interconnected array, creating a three-dimensional (3D) system with impressive storage density. Another variation of racetrack memory involves magnetic nanotubes with

azimuthal flux-closure domains [8, 9]. These nanotubes consist of numerous domains, each with a domain wall size on the order of tens of nanometers, enclosed within a long tube extending several tens of micrometres. This magnetic nanotube-based racetrack memory offers exceptional storage capacity and performance in a compact form factor by storing information as azimuthal domains with opposing circulation of magnetisation.

Although racetrack memory holds considerable promise, it is still mostly restricted to research laboratories and mainly exists as a theoretical concept due to the substantial fabrication challenges involved in transitioning to a 3D architecture. Initial development efforts aimed at racetrack memory components centred on domain wall movement within flat, two-dimensional (2D) nanostrips produced through lithography in order to streamline the fabrication and observation processes. While these attempts provided valuable insights into wall structures and current-induced STT, the magnetically soft nanostrips are inherently unsuitable for racetrack memory applications. The domain walls in nanostrips become dynamically unstable above a certain field or current threshold, called the Walker breakdown limit, resulting in periodic magnetic structure transformations and reduced mobility. In contrast, studies have shown that nanowires and nanotubes offer high domain wall speeds of up to a kilometre per second and the ability to control the domain wall above the Walker breakdown limit [10]. Combined with the 3D structure, these features make nanowires and nanotubes promising candidates for future low-power consumption and high-density magnetic memories. Researchers are also exploring other curved geometries [11], the relationship between curvature and magnetism, and three-dimensional nanomagnetism [12]. These intersecting research areas present new challenges and opportunities for innovative magnetic configurations, enhanced understanding of physics, and the potential for higher areal density in 3D spintronic devices.

Ferromagnetic nanotubes, similar in cylindrical geometry to nanowires, have been less explored, despite their extensive potential in fields like biomedicine, catalysis, sensors, and data storage [11, 13–15]. Their individual magnetic properties have not been adequately investigated, with theoretical studies and simulations suggesting that the behaviour of domains and domain walls in nanotubes mirrors that in cylindrical nanowires due to their shared geometry. These nanotubes can be synthesized from various ferromagnetic materials such as Fe, Ni, or Co, which influences their magnetic anisotropy, coercivity, and magnetization reversal mechanisms.

In addition to their shared geometry with nanowires, ferromagnetic nanotubes offer several advantages, particularly in uncovering new physics and designing innovative devices. Their magnetic properties can be fine-tuned by altering the tube wall thickness, and their hollow structure allows the creation of more complex architectures, thus expanding their application possibilities. Nanotubes are known for their controllable velocity of domain walls (DWs), even at high speeds, surpassing the Walker breakdown threshold. This characteristic makes them particularly suitable for spintronic applications, including the design of racetrack memory devices that operate on the shifting of domain walls [11].

Flux-closure (azimuthal) magnetic domains in CoNiB nanotubes were experimentally discovered through XMCD-PEEM (X-ray Magnetic Circular Dichroism Photo-Emission Electron Microscopy). Despite the expectation of axial magnetisation for elongated tubes made of soft magnetic materials, a series of azimuthal domains were observed. This discovery could have significant implications for dense data storage and curvature-induced magnetic phenomena [9].

In this thesis, we focus on the study of Co-rich CoNiB ferromagnetic nanotubes with various thicknesses, diameters, and high aspect ratios. We employ transmission electron microscopy (TEM) as the primary investigative tool. Owing to its high resolution and sensitivity, TEM provides a comprehensive understanding of the structural, chemical, and magnetic properties of these nanotubes.

Moreover, electron holography, a TEM-based technique, is utilized for magnetic imaging to detect the magnetic domain structure in the nanotubes.
One key motivation behind this thesis is the need to observe and understand the domain walls in nanotubes. Although these walls were not observed experimentally in previous studies, we managed to observe a domain wall and study various states and transformations from the azimuthal state to the axial state under the field, including the appearance of intermediate states at small fields and the detection of mixed-state curling at the tube ends.
By utilizing advanced electron microscopy techniques, this thesis aims to deepen our understanding of the magnetic properties of ferromagnetic nanotubes and their potential applications in spintronics. We aim to reveal new insights into the unique properties and behaviour of nanotubes, particularly regarding their domain wall characteristics.
Following this introductory chapter (Chapter 1), the thesis is organized into five additional chapters as follows:
In chapter 2, entitled "Theoretical background and state of the art", we set the stage for discussing magnetic nanotubes. We investigate their unique geometry, benefits, applications, magnetic textures, phase diagrams, and domain structures. The chapter concludes with state-of-the-art theoretical and experimental studies and nanotube synthesis methods, providing a solid foundation for understanding the research presented in subsequent chapters.
Chapter 3, "Methods and Instrumentation," provides an overview of the various experimental techniques employed in this thesis. We begin with an introduction to TEM and STEM, followed by a discussion on magnetic imaging in TEM. We emphasize the importance of electron holography, focusing on off-axis electron holography as the main magnetic imaging technique used in this thesis. We describe phase image reconstruction and the separation of electrostatic and magnetic contributions. Additionally, we briefly discuss STXM as another method for studying nanotubes, using XAS and XMCD signals, particularly for azimuthal domains. Furthermore, we address chemical characterization techniques, such as EDX and EELS, and discuss TEM sample preparation, including the FIB fabrication of cross-section nanotubes.
Chapter 4, entitled “Structural and Chemical Analysis of Nanotubes”, emphasizes the importance of understanding the thickness and composition of CoNiB magnetic nanotubes to learn their magnetic properties. The nanotube thickness dramatically influences its magnetic behaviours, making a precise thickness measurement crucial. In this chapter, we introduce the thickness cross-section function and review existing TEM microscopy methods for measuring the thickness. Chemical characterization using EDX and EELS is included in determining material density, which affects thickness calculation. The benefits and drawbacks of each method are discussed, and the calculated thickness is employed to estimate composition, including boron content. In this chapter, we discuss obtaining a theoretical estimation of the mean inner potential of polycrystalline material. We also explain using the contrast transfer function concept to identify phase contrast in the data resulting from microscope aberrations.
Chapter 5, entitled "Magnetic imaging of CoNiB ferromagnetic nanotubes", explores the world of magnetic domain walls in ferromagnetic CoNiB nanotubes. Our pioneering research, using advanced electron microscopy techniques, primarily electron holography, offered the first experimental evidence of these domain walls in ferromagnetic nanotubes. Through an intricate study encompassing experimental observations and theoretical simulations, we identified the interplay of Néel and Bloch domain walls within the nanotubes. This investigation not only deepened our understanding of magnetic phenomena at the nanoscale but also underscored the crucial role of such analytical models used to extract important parameters from both electron holography and STXM

techniques.
For the sake of transparency and ethics, I want to mention that the writing of this manuscript made use of artificial intelligence, specifically OpenAI's ChatGPT, for proofreading, translating texts, reformulating sentences, and ensuring grammatical accuracy.

1.2 Introduction (Français)

Le stockage traditionnel des données numériques s'effectue sur des disques durs magnétiques (HDDs) et de la mémoire flash électronique, telle que les disques à état solide (SSDs), pour gérer la grande quantité de données à l'échelle mondiale. Un objectif important dans les technologies de stockage de données est d'augmenter la densité de stockage surfacique en minimisant la taille d'un bit d'information jusqu'à l'échelle nanométrique. Cet objectif répond à plusieurs préoccupations, en particulier la satisfaction de la demande croissante en capacité de stockage de données, l'amélioration de l'efficacité des coûts pour une meilleure accessibilité et abordabilité, l'amélioration de l'efficacité énergétique pour réduire la consommation d'énergie et l'impact environnemental, l'augmentation de la vitesse et de la performance grâce à des circuits de transfert de l'information plus courts pour un accès et un transfert de données plus rapides, et la facilitation de conceptions de dispositifs plus portables et compacts à l'aide de composants plus petits. Ensemble, ces améliorations répondent aux besoins diversifiés des consommateurs et des entreprises. Cependant, les dispositifs nanométriques traditionnels, qui dépendent de la manipulation de la charge électronique, rencontrent plusieurs limitations à mesure qu'ils continuent de réduire en taille. Une préoccupation majeure est la dissipation de l'énergie, qui peut entraîner une augmentation de la consommation d'énergie et une défaillance potentielle du composant due à la surchauffe. De plus, ces dispositifs rencontrent des défis pour évoluer en deçà de certaines dimensions, limitant leur performance et une miniaturisation plus poussée. Les dispositifs de mémoire basés sur la charge, tels que la mémoire à accès aléatoire dynamique (DRAM), nécessitent également des cycles de rafraîchissement continus pour maintenir les données stockées, ce qui peut être couteux en énergie et affecter négativement la fiabilité de l'appareil. Par conséquent, les chercheurs explorent des approches alternatives comme la spintronique pour surmonter ces limitations et développer des dispositifs nanométriques plus efficaces et polyvalents.
La spintronique est un domaine de recherche qui exploite à la fois les propriétés électriques et le spin des électrons, offrant un degré de liberté supplémentaire pour les dispositifs potentiels. La spintronique à l'échelle nanométrique est particulièrement pertinente en raison despetites longueurs caractéristiques du magnétisme, comme les tailles des parois de domaine magnétique. La découverte de l'effet de magnétorésistance géante (GMR) en 1986 a été pionnière en spintronique [1] et plusieurs autres phénomènes, tels que la magnétorésistance tunnel (TMR) [2], le couple de transfert de spin (STT) [3], l'effet Hall de spin (SHE) [4, 5], et l'effet Seebeck de spin (SSE) [6], sont depuis apparus et ont largement contribué aux avancées dans les applications de mémoire magnétique rapide et à faible consommation d'énergie. Ces phénomènes ont permis le développement de diverses technologies de mémoire évolutives et écoénergétiques, y compris la mémoire à accès aléatoire magnétique (MRAM), la MRAM à couple de transfert de spin (STT-MRAM), et la MRAM à couple de spin-orbite (SOT-MRAM), ainsi que des applications potentielles dans les dispositifs spintroniques thermiquement activés et la récupération d'énergie. En 2004, Parkin et al. ont introduit un concept innovant pour un dispositif magnétique non-volatile appelé mémoire à circuit de course [7]. Dans ce concept, l'information serait codée sous forme de domaines magnétiques

séparés par des parois de domaine dans des nanofils cylindriques, qui peuvent être déplacés à l'aide d'un courant électrique. Les fils seraient disposés verticalement dans un grand réseau interconnecté, créant un système tridimensionnel (3D) avec une densité de stockage impressionnante. Une variante de ce concept impliquerait des nanotubes magnétiques avec des domaines à fermeture de flux azimutal [8, 9]. Ces nanotubes consistent en de nombreux domaines, chacun avec une taille de paroi de domaine de l'ordre de dizaines de nanomètres, enfermés dans un long tube s'étendant sur plusieurs dizaines de micromètres. Cette mémoire à registre défilant basée sur des nanotubes magnétiques pourrait offrir une capacité de stockage et des performances exceptionnelles dans un format compact en stockant l'information en tant que domaines azimutaux avec une circulation opposée de l'aimantation.

Bien que la mémoire à circuit de course soit très prometteuse sur le papier, elle est encore au stade de recherche en laboratoire. Les efforts de développement initiaux ciblant les composants de mémoire à registre défilant utilisaient le déplacement de parois de domaine dans des nanobandes plates, bidimensionnelles (2D), produites par lithographie afin de rationaliser les processus de fabrication et d'observation. Bien que ces tentatives aient fourni des informations précieuses sur les structures des paroi et le phénomène de transfert de spin (STT) induit par le courant, les nanobandes magnétiquement douces sont intrinsèquement inadaptées à ces application. En effet, les parois de domaine dans les nanobandes deviennent dynamiquement instables au-dessus d'un certain seuil de champ ou de courant, appelé la limite de Walker, entraînant des transformations périodiques de structure magnétique et une mobilité réduite. En revanche, des études théorique ont prédit que les nanofils et les nanotubes pourraient permettre des vitesses de paroi de domaine élevées jusqu'à un kilomètre par seconde et la capacité de contrôler la paroi de domaine au-dessus de la limite de Walker [10]. Combinés à la capacité de les réaliser en réseaux 3D denses, ces caractéristiques font des nanofils et des nanotubes des candidats intéressant pour les futures mémoires magnétiques à faible consommation d'énergie et à haute densité. Les chercheurs explorent également d'autres géométries courbées [11], la relation entre la courbure et le magnétisme, et le nanomagnétisme tridimensionnel [12]. Ces domaines de recherche qui se croisent présentent de nouveaux défis et opportunités pour des configurations magnétiques innovantes, une compréhension améliorée de la physique, et le potentiel d'une densité surfacique plus élevée dans les dispositifs spintroniques 3D. Les nanotubes ferromagnétiques, similaires en géométrie cylindrique aux nanofils, ont été moins explorés, malgré leur potentiel considérable dans des domaines comme la biomédecine, la catalyse, les capteurs, et le stockage de données [11, 13–15]. Leurs propriétés magnétiques individuelles n'ont pas été très étudiées expérimentalement. De leur côté, des études théoriques et des simulations suggérent que le comportement des domaines et des parois de domaine dans les nanotubes est similaire à celui des nanofils cylindriques en raison de leur géométrie commune. Ces nanotubes peuvent être synthétisés à partir de divers matériaux ferromagnétiques tels que Fe, Ni, ou Co, ce qui influence leur anisotropie magnétique, leur coercivité, et leurs mécanismes de renversement de l'aimantation.

En plus de leur géométrie commune avec les nanofils, les nanotubes ferromagnétiques offrent plusieurs avantages, notamment dans la découverte de nouvelles physiques et la conception de dispositifs innovants. Leurs propriétés magnétiques peuvent en effet être changées en modifiant l'épaisseur de la paroi du tube, et leur structure creuse permet la création d'architectures plus complexes, élargissant ainsi leurs possibilités d'application. Les nanotubes pourraient ainsi permettre une vitesse contrôlable des parois de domaine (DWs), même à des vitesses élevées, dépassant le seuil de Walker. Cette caractéristique les rend particulièrement adaptés aux applications spintroniques, y compris la conception de dispositifs de mémoire à registre à défilement qui fonctionne sur

le principe de déplacement des parois de domaine [11].
Les domaines magnétiques à fermeture de flux (azimutaux) dans les nanotubes de CoNiB ont été révélés expérimentalement par le biais de la microscopie XMCD-PEEM (X-ray Magnetic Circular Dichroism Photo-Emission Electron Microscopy), ceci malgré l'attente initiale d'une aimantation axiale pour des tubes allongés fabriqués à partir de matériaux magnétiques doux. Cette découverte pourrait avoir des implications significatives pour le stockage de données dense et les phénomènes magnétiques induits par la courbure [9].
Dans cette thèse, nous nous concentrons sur l'étude des nanotubes ferromagnétiques CoNiB riches en Co avec diverses épaisseurs, diamètres et grands rapports d'aspect. Nous utilisons la microscopie électronique à transmission (TEM) comme principal outil d'investigation. Grâce à sa haute résolution et sa sensibilité, le TEM offre une compréhension globale des propriétés structurelles, chimiques et magnétiques de ces nanotubes. De plus, l'holographie électronique, une technique basée sur le TEM, est utilisée pour l'imagerie magnétique, offrant ainsi un aperçu des détails complexes de la structure des domaine magnétique dans les nanotubes.
Une motivation clé derrière cette thèse est le besoin d'observer et de comprendre les parois de domaine dans les nanotubes. Bien que ces parois n'aient pas été observées expérimentalement dans les études précédentes, nous avons réussi à observer une paroi de domaine et à étudier divers états et transformations de l'état azimutal à l'état axial sous champ magnétique, y compris l'apparition d'états intermédiaires à petits champs et la détection de curling de l'aimantation aux extrémités du tube.
En utilisant des techniques avancées de microscopie électronique, cette thèse vise à approfondir notre compréhension des propriétés magnétiques des nanotubes ferromagnétiques et de leurs applications potentielles en spintronique. Nous visons à révéler de nouvelles perspectives sur les propriétés et le comportement uniques des nanotubes, en particulier en ce qui concerne leurs caractéristiques de parois de domaine.
Après ce chapitre d'introduction (Chapitre 1), la thèse est organisée en cinq chapitres supplémentaires comme suit :
Dans le chapitre 2, intitulé "Contexte théorique et état de l'art", nous préparons le terrain pour discuter des nanotubes magnétiques. Nous étudions leur géométrie unique, leurs avantages, leurs applications, leurs textures magnétiques, leurs diagrammes de phase et leurs structures de domaine. Le chapitre se conclut par des études théoriques et expérimentales de pointe ainsi que des méthodes de synthèse de nanotubes, fournissant une base solide pour comprendre la recherche présentée dans les chapitres suivants.
Dans le chapitre 3, "Méthodes et instrumentation", nous fournissons un aperçu des différentes techniques expérimentales employées dans cette thèse. Nous commençons par une introduction à la MET et à la MET en balayage, suivie d'une discussion sur l'imagerie magnétique en MET. Nous soulignons l'importance de l'holographie électronique, en nous concentrant sur l'holographie électronique hors axe comme principale technique d'imagerie magnétique utilisée dans cette thèse. Nous décrivons la reconstruction de l'image de phase et la séparation des contributions électrostatiques et magnétiques. De plus, nous discutons brièvement du STXM comme une autre méthode pour étudier les nanotubes, en utilisant les signaux XAS et XMCD, en particulier pour les domaines azimutaux. En outre, nous abordons les techniques de caractérisation chimique, telles que l'EDX et l'EELS, et discutons de la préparation des échantillons pour la MET, y compris la fabrication de nanotubes en coupe transversale par FIB.
Le chapitre 4, intitulé « Analyse structurale et chimique des nanotubes », souligne l'importance de comprendre l'épaisseur et la composition des nanotubes magnétiques CoNiB pour apprendre leurs

propriétés magnétiques. L'épaisseur du nanotube influence fortement ses comportements magnétiques, ce qui rend une mesure précise de l'épaisseur cruciale. Dans ce chapitre, nous introduisons la fonction de section transversale de l'épaisseur et passons en revue les méthodes existantes de microscopie TEM pour mesurer l'épaisseur. La caractérisation chimique utilisant EDX et EELS est incluse dans la détermination de la densité du matériau, qui affecte le calcul de l'épaisseur. Les avantages et les inconvénients de chaque méthode sont discutés, et l'épaisseur calculée est employée pour estimer la composition, y compris la teneur en bore. Dans ce chapitre, nous discutons de l'obtention d'une estimation théorique du potentiel moyen interne du matériau polycristallin. Nous expliquons également comment utiliser le concept de fonction de transfert de contraste pour identifier le contraste de phase dans les données résultant des aberrations du microscope.
Le Chapitre 5, intitulé "Imagerie magnétique des nanotubes ferromagnétiques CoNiB", explore le monde fascinant des parois de domaines magnétiques dans les nanotubes ferromagnétiques CoNiB. Notre travail utilise des techniques avancées de microscopie électronique, principalement l'holographie électronique, a fourni la première preuve expérimentale directe de la structure de ces parois de domaine dans les nanotubes ferromagnétiques. À travers une étude complexe englobant des observations expérimentales et des simulations théoriques, nous avons identifié l'interaction des parois de domaine de Néel et de Bloch au sein des nanotubes. Cette étude non seulement approfondit notre compréhension des phénomènes magnétiques à l'échelle nanométrique, mais a également souligné le rôle crucial des modèles analytiques utilisés pour extraire des paramètres importants à partir des techniques d'holographie électronique et STXM.
Par souci de transparence et d'éthique, je tiens à mentionner que la rédaction de ce manuscrit a utilisé l'intelligence artificielle, en particulier le ChatGPT d'OpenAI, pour la relecture, la traduction de textes, la reformulation de phrases et l'assurance de l'exactitude grammaticale.

Chapter 2

Theoretical background and state of the art

This chapter is dedicated to the exploration of magnetic nanotubes and their unique properties. While the broader field of nanomagnetism, including phenomena such as magnetic domains, domain walls, and curvilinear magnetism, provides a rich context for this discussion, those topics are extensively covered in key literature. For an in-depth understanding of these foundational concepts, the reader is referred to the following seminal works: [16–18] for magnetism; [19–21] for domain walls in nanostrips; [20, 22] for domain walls in nanowires; and [12, 23] for 3D spintronics and curvilinear magnetism.
This chapter explores the world of magnetic nanotubes. We delve into their distinct geometry, which offers numerous advantages for applications. The magnetic textures and magnetisation of nanotubes are defined, elucidating their geometrical and magnetic behaviours. Special attention is given to the magnetic domains within nanotubes, including the end-vortex, azimuthal domains, and the domain walls they host. In synthesizing this knowledge, we also consider the latest theoretical and experimental studies that shed light on the properties of magnetic nanotubes. The chapter concludes with a review of the methods employed for their synthesis, including chemical techniques like electroless plating and atomic layer deposition, which are pivotal for practical applications.

2.1 Ferromagnetic nanotubes

In this section, we will delve into the world of ferromagnetic nanotubes, exploring the unique geometry of these structures and the magnetic configurations they exhibit. We will examine the magnetic phase diagram and the various magnetic states, including axial, azimuthal, mixed and End-vortex states, along with the corresponding DWs. A comprehensive review of the existing literature on ferromagnetic NTs, encompassing both theoretical and experimental studies, will also be presented. Additionally, we will discuss the materials and synthesis techniques used to create these NTs. The primary emphasis will be on ferromagnetic metallic tubes made of NiCoB, as well as their potential combination with other materials. We will not delve into carbon nanotubes, for which readers can refer to the book "Magnetism in Carbon Nanostructures" [24].

2.1.1 Geometry and application benefits

Ferromagnetic nanotubes (NT)s are cylindrical structures composed of magnetic materials that exhibit ferromagnetic behaviour. The geometry of these structures plays a crucial role in determining

their magnetic properties and potential applications. Unlike 2D nanostrips, NTs have a 3D geometry with a distinct topology that enables the creation of more complex structures and devices. With a large aspect ratio length (l) / diameter (d), the outer radius (R) and inner radius (r) of a NT determine its overall size. At the same time, the wall-thickness ($t = R - r$) gives us control over its magnetic properties (Figure 2.1). Despite the fact that the NTs have cylindrical geometry similar to the nanowires, the wall thickness gives the NTs an additional degree of freedom compared to the wires, making it possible to tailor the magnetic properties of the sample. Moreover, due to the lack of magnetic material around the axis of symmetry, magnetic singularities (Bloch points) associated with vortex states and vortex-like domain walls are not present [25, 26]. It makes it possible to properly account for magnetostatic effects, leading to changes in the static and dynamic properties and enabling magneto-chiral effects [27, 28].

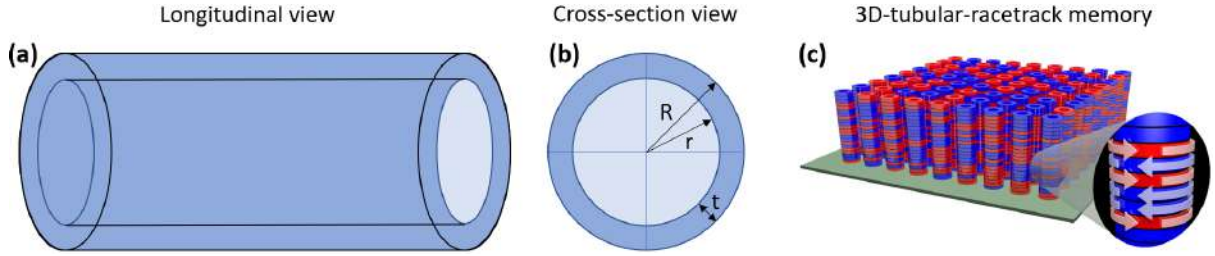

Figure 2.1: A schematic illustration of a cylindrical nanotube, showing (a) a view along its length (longitudinal view), and (b) a cross-sectional view. The figure indicates the outer radius (R), inner radius (r), and thickness (t) of the tube. (c) Magnetic racetracks in tubes with flux-closure domains for data storage. (c) is adapted from [8].

Racetrack memories are a promising type of data storage technology that utilizes NTs to store data in magnetic domains [7]. The data is stored by shifting azimuthal domains along the nanotube, where the magnetic field direction represents the binary digits "0" or "1" (Figure 2.1.c). By selectively applying electric current, the magnetic domains along the nanotube can be moved and shifted, enabling the writing, reading, and erasing of data.
In biotechnology and nanomedicine, NTs have gained significant interest due to their unique properties [29, 30].

2.1.2 Magnetic configurations in nanotubes

In this section, attention is focused on the magnetic states present in nanotubes. By examining the magnetic textures and phase diagrams, we can gain a deeper understanding of various magnetic states, including axial, azimuthal, and mixed domains, as well as end-vortex domains. Furthermore, the behaviour of domain walls in nanotubes exhibiting axial or azimuthal domains will be analyzed to provide a comprehensive understanding of the magnetic properties of these tubes. Different magnetic arrangements can occur within a nanotube, as depicted in Figure 2.2. However, it is important to note that not all of these configurations may be stable, and other more intricate arrangements may exist under specific anisotropic conditions. In many long NTs, a mixed magnetic state is prevalent. This state consists of axial magnetisation in the central part of the tube, with vortices appearing at the ends. The application of a transverse magnetic field may lead to the formation of an onion state, which could become a transverse state if the field strength increases. The radial state, however, is not as prevalent because of its high dipolar energy. Nevertheless, it

can still appear as a meta-stable domain wall in some parts of the tube. It is worth noting that the depicted magnetic configurations in this illustration are purely theoretical predictions and that only a subset of these domains has been substantiated through experimental observation [8, 13, 31, 32].

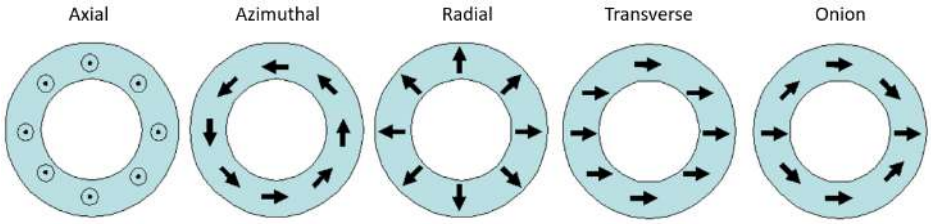

Figure 2.2: This figure displays potential magnetisation states in a nanotube. It only shows a cross-section view of the tube. The final magnetisation state may be an axial (longitudinal) state, azimuthal (vortex) state, or a combination of both (mixed state), depending on the geometry of the nanotube. Adapted from [31].

2.1.2.1 Magnetic textures and magnetisation phase diagram

Researchers have published phase diagrams that demonstrate the relationship between the magnetic properties of soft nanotubes and their geometries [31, 33–37]. One such phase diagram, presented by Landeros [36], illustrates that magnetisation in nanotubes can exist in three distinct magnetic states. depending on the length l, the outer radius R and the shape factor ($\beta = r/R$) of the tube. These arrangements include (1) an axial state (AS), (2) a mixed state (MS), or (3) an azimuthal (vortex) state (VS). These findings were based on calculations of the interplay between dipole and exchange energies and did not consider any magnetocrystalline anisotropy.

The AS is characterized by uniform magnetisation along the axis of the nanotube, while the mixed state has both axial magnetisation and azimuthal magnetisation at the ends of the tube. The global azimuthal state is characterized by an azimuthal magnetisation throughout the entire nanotube. The studies conducted on the magnetisation phase diagrams of NTs have indicated that, for elongated nanotubes, the mixed state is energetically more favourable compared to the axial and azimuthal states for a broad range of geometries. Long NTs with small radii are predicted to exhibit an almost uniform axial magnetisation along their axis. In contrast, the uniform azimuthal state is the ground state for short NTs with a large diameter (small aspect ratio) and thick tube walls [36]. Moreover, Wyss et al. [38] conducted experimental research that confirmed the trends in the geometrical dependence of the preferred magnetic state, either axial or azimuthal, in NTs. Additionally, the existence of magnetic states like transverse magnetisation or onion state has been theoretically investigated [31]. Still, they can only be stabilised under the influence of an external transverse magnetic field. In comparison, a uniformly magnetised domain (axial, azimuthal or mixed) is energetically favoured over a multidomain state with DWs [31]. The latter may persist as a metastable state or in larger structures, or in the presence of additional anisotropy, such as magnetocrystalline anisotropy. The next section will delve deeper into the End-vortex domains, which have been observed at the ends of NTs, including those with axial magnetisation, such as in the case of the mixed state.

2.1.2.2 End-Vortex Domains and Mixed State in Nanotubes

The finite nature of cylindrical structures has been studied by Micromagnetic simulations, as the reversal of magnetisation begins at the tube ends [25, 39]. Subsequently, another research found evidence of "bamboo-like" magnetic states, characterized by an axial magnetisation that curves near the tube's ends and creates azimuthal-like (vortex) domains with the same or opposite chirality [40]. Further studies using micromagnetic simulations and mathematical models delved into the magnetic phase diagram and its connection to the creation of azimuthal-like DWs [36, 37, 41–43]. These mixed states, which consist of a combination of the uniform-axial state along the tube and end-vortex states at the tube's ends, are of interest because they offer insight into the reversal of magnetisation. Modelling the magnetisation of the end-vortex domains allows for a better understanding of the entire reversal process.

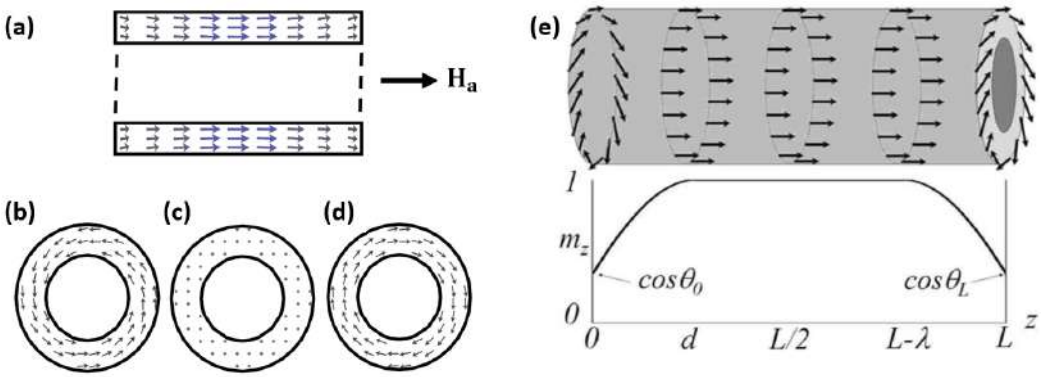

Figure 2.3: (a-d) Micromagnetic simulation of magnetisation for a nanotube (diameter $\approx 100\,\text{nm}$) in the twisted bamboo phase, under an applied magnetic field $\mathbf{H}_a$ of 5 mT parallel to the tube axis. (a) A longitudinal view along the length of the tube. Cross-sectional views of (b) the bottom, (c) middle, and (d) top of the nanotube, normal to the tube axis. (e) Illustration of a mixed state in magnetic NTs. The centre of the tubes shows uniform-axial magnetisation, while the tube's ends contain partial azimuthal domains. Where m_z is the axial component of the magnetisation, d and lambda represent the size of the areas where the axial component of the magnetisation (m_z) deviates from the z-axis. θ_0 and θ_L are the angles at which the magnetisation is aligned with the z-axis, as evaluated at the ends of the tube. (a-d) are adapted from [40]. (e) is adapted from [36].

Additionally, the end-vortex domains of cylindrical structures play a vital role in the reversal of magnetisation, which is initiated by propagating azimuthal domain walls. The characteristics of these domains are influenced by factors such as geometry, magnetic material, and external stimuli. A model can be used to estimate the internal energy of the mixed state [36], taking into account parameters such as the size of the end-vortex domains, the polar angles of the magnetisation at the tube ends, and other parameters, which depend on the geometry and materials. On the other hand, the chirality of the azimuthal domains at the tube ends is determined by the distribution of the azimuthal magnetisation component distribution [27], which is connected to the radial component and results in chiral magnetic configurations. These chiral terms reflect the coupling of different types of magnetic charges, including the geometrical charge inherent in a curved nanomagnet [44]. Micromagnetic simulations show that opposite azimuthal (vortex) chiralities are preferred dynamically [37, 40, 41, 45]. However, the challenge is to determine the chirality of these domains experimentally.

The relative chirality of the azimuthal domains at the tube ends, and the polarity of the axial magnetisation component could have practical implications for storage purposes. The mixed state of magnetic configurations in NTs has three binary attributes, including polarity and two chiralities, which can be arranged in eight different ways. Therefore, an array of nanotubes presents an enormous number of possible configurations that could have practical applications in magnetic data storage. While there has been a significant amount of theoretical research on End-Vortex domains in ferromagnetic NTs, there is currently a lack of experimental studies in this area. This is due to the technical difficulties associated with detecting the chirality of these azimuthal domains, which can be very small in size and located at the ends of NTs. However, we have been able to perform electron holography, and we have observed some evidence of these End-vortex domains in CoNiB long NTs under an applied magnetic field. The results of this research will be discussed in detail in Chapter 5. As a result, finding a way to observe and characterize these domains experimentally remains a significant challenge in the field.

2.1.2.3 Azimuthal domains in nanotubes

Most research efforts, both theoretical and experimental, have centred around NTs with axial magnetisation. This is the standard alignment for elongated NTs unless they display specific forms of anisotropy, like magnetocrystalline anisotropy. This section will delve into NTs that exhibit azimuthal magnetisation.

The work of Li et al. [46] involved the preparation of single-crystalline-electroplated Co NTs. They analyzed the tubes using global magnetometry on arrays of tubes, selective area electron diffraction, and magnetic force microscopy (MFM) on individual tubes and concluded that the tubes exhibited azimuthal magnetisation (flux-closure state) due to a magnetocrystalline easy axis perpendicular to the tube axis. The findings from magnetometry and diffraction supported this conclusion, but the interpretation of the MFM results is debatable. The electron microscopy images of the tubes after dissolution in sodium hydroxide showed signs of oxidation, which raised questions about the validity of the MFM results. In other words, their previous experiments with nanowires led them to estimate the cobalt oxide layer to be 3 nm thick [46]. However, this may not accurately apply to NTs, especially thin-walled ones like the ones they studied, as both the inner and outer surfaces of the tubes can be exposed to hydroxide, leading to complete oxidation. This leads to the likelihood that the weak signal they measured by MFM came from an electrostatic contribution rather than a magnetic one. This conclusion is strengthened by the lack of change in contrast after annealing and the absence of contrast expected for azimuthal domains.

Additionally, Wyss et al. [38] conducted research on short magnetic NTs using synchrotron magnetic microscopy, resulting in the discovery of flux-closure (azimuthal) domains. An example of their work can be seen in Figure 2.4. The study found that ferromagnetic NTs made of permalloy (Py) and CoFeB, with a length of fewer than 2 µm, a diameter between 200 and 300 nm, and a thickness of 30 nm, displayed remanent azimuthal configurations. They found that the ratio of the length to the diameter of the NTs was a key factor in maintaining the stability of the global azimuthal state. According to calculations, longer ferromagnetic NTs were expected to occupy a mixed-state configuration, where the central part of the NT would align along its long axis with only the ends forming vortices. However, for further study of spin-wave physics and for applications in areas such as magnonic and data storage, ferromagnetic NTs with larger length-to-diameter ratios are necessary.

In 2018, Stano and colleagues [9] explored the possibility of establishing remanent flux-closure

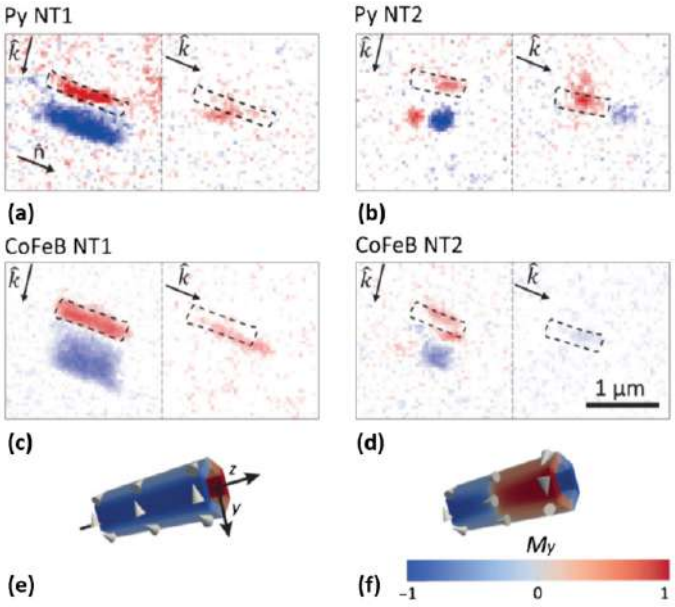

Figure 2.4: This figure shows XMCD-PEEM images of short ferromagnetic NTs with different lengths and materials. The images display the normalized magnetisation along the y-axis. There are four images in total, two of Py NTs and two of CoFeB NTs, each showing a global azimuthal state (a and c) and an opposing azimuthal state (b and d). The figure also includes two simulations of the equilibrium states of ferromagnetic NTs with a length of 610 nm and a diameter of 245 nm, one in a global azimuthal state (e) and one in an opposing azimuthal state (f). The arrowheads in each image indicate the direction of the local magnetisation. This figure is adapted from [38].

states in longer NTs by using magnetic anisotropy. To achieve this, the researchers synthesized CoNiB nanotubes through electroless plating in porous templates. The resulting tubes were up to 30 µm in length, with diameters between 300 and 400 nm, and a thickness of 30 nm. Using techniques like XMCD-PEEM (Figure 2.5) and STXM (Figure 2.6), the authors carried out magnetic imaging of individual specimens in remanence, revealing the presence of NTs in purely azimuthal configurations. Additionally, the authors also analyzed the magnetic imaging of the nanotubes by STXM under magnetic fields. The XMCD-PEEM image displays sharp-enclosed flux domains, but this is not the case in the STXM images, as the sample had aged over a year before the STXM was performed and showed a tilted state. These configurations were stabilized by an effective anisotropy coefficient of approximately $10\,\mathrm{kJ/m^3}$, which may have arisen from the magnetoelastic coupling or anisotropic interfacial magnetic anisotropy. This finding suggests that the strength of magnetic anisotropy and the type of remanent magnetic configuration can be adjusted through changes in material composition or annealing. Similar to Stano's investigations, Zimmermann et al. [47] conducted a study on the remanent configurations in $Ni_{80}Fe_{20}$ NTs. Using a combination of Anisotropic magnetoresistance (AMR) measurements and STXM, the researchers investigated NTs with lengths ranging from 10 to 30 µm, a diameter of 500 nm, and a thickness of 30 nm. The study found that the NTs displayed stable azimuthal configurations made up of azimuthal domains, regardless of the length of the nanotube. This result supports the idea that magnetic anisotropy plays a role in stabilizing the remanent configurations of these NTs.

In this thesis, we will investigate tubes that are similar to those studied by Stano [9], with various diameters and thicknesses. Our research will involve structural and chemical analysis, as well as

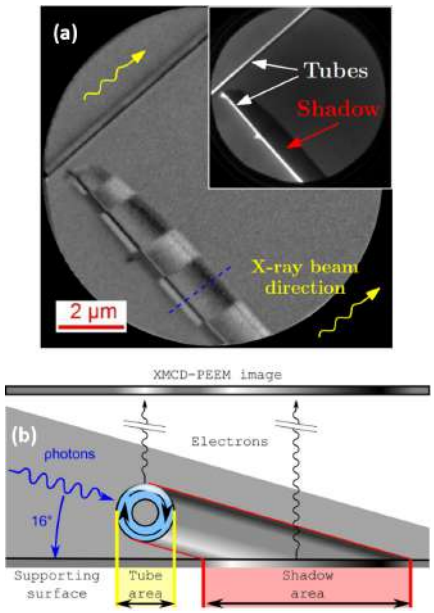

Figure 2.5: The figure illustrates magnetic domains with azimuthal orientation in nanotubes. (a) displays an XMCD-PEEM (Co-L_3 edge) image of two NTs positioned at orthogonal angles. The tube along the beam shows minimal contrast, while the tube perpendicular to the beam reveals pronounced contrast, indicating the presence of azimuthal magnetic domains. The grey line in the shadow near the rim is due to oxidation of the inner tube surface and is non-magnetic. The inset displays a non-magnetic PEEM image of the tubes. (b) shows a schematic of the azimuthal magnetisation and XMCD-PEEM contrast along a line profile of an azimuthal domain, which is indicated by a blue, dashed line in panel (a). This figure is adapted from [9].

magnetic imaging under the influence of magnetic fields using electron microscopy. For further information, please refer to Chapters 4 and 5. In the next section, we will examine the studied DWs in these NTs.

2.1.2.4 Domain walls in nanotubes

In magnetic NTs, the reversal of magnetisation can occur in a few ways, including through the nucleation and progression of DWs [35]. Most DWs in magnetic tubes are considered to be metastable [31], and uniform-axial, mixed or azimuthal domains are thought to have a lower energy state. Despite this, research has mainly focused on walls between axial domains, and there are only a few studies that examine walls between azimuthal domains, which are typically found in NTs with small aspect ratios (large diameters and short lengths). So far, research on DWs has been limited to theoretical and simulated models, with no practical experiments reported. While some experiments have observed azimuthal domains in NTs [9, 38, 46, 47], no domain wall has been successfully stabilized or imaged in NTs with azimuthal domains yet. However, we will report in Chapter 5 the first experimental evidence of a domain wall between two azimuthal domains in long nanotubes by electron holography.

The shape of magnetic NTs usually results in them being assumed to have an axial magnetisation. As a result, DWs in these NTs are predicted to resemble those found in cylindrical nanowires. Theoretical and simulation-based studies predict the existence of two types of DWs in these NTs:

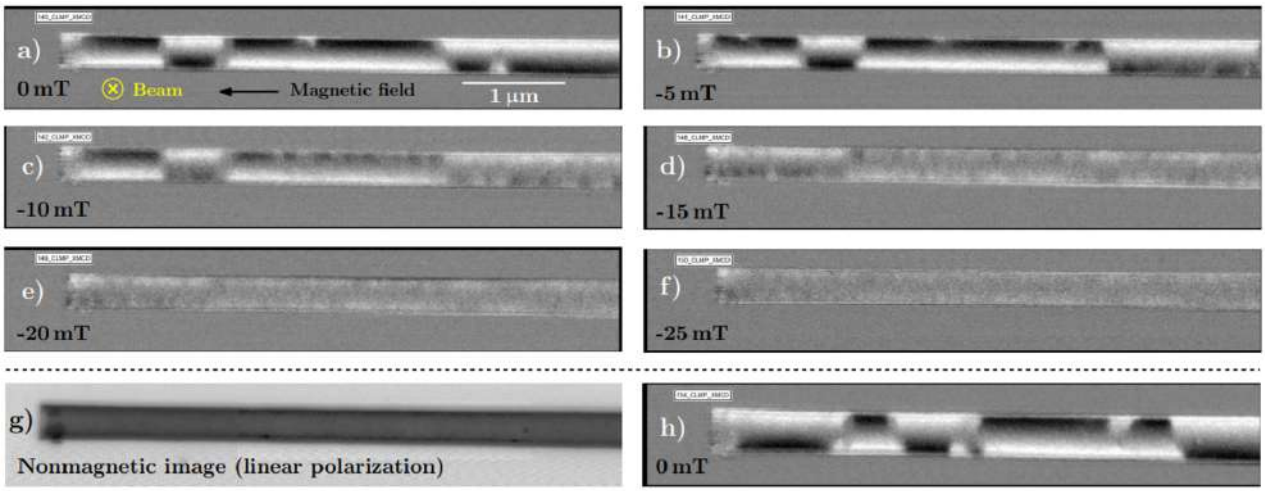

Figure 2.6: STXM Images under Magnetic Field. (a-f) The figure shows XMCD magnetic images (Co-L_3 edge) of tubes under axial magnetic fields, ranging from low to high magnitudes. As the field strength increases, the STXM contrast decreases, indicating that the magnetisation is rotating towards the axial direction. It takes about 25 mT for the tubes to reach saturation along the axial direction. The field of view in images (a-g) is $6.0 \times 1.0\,\mu m^2$, and $4.8 \times 0.8\,\mu m^2$ in (h). Image (g) represents a non-magnetic STXM image, which highlights the tubular structure using linear polarization of X-rays. Image (h) is the XMCD image after the removal of the magnetic field, following the sequence (a-f). The transition between neighbouring domains is not as sharp as in XMCD-PEEM images, which the authors attribute to sample ageing (The STXM was done one year after the XMCD-PEEM). This figure is adapted from [9].

the transverse wall and the vortex-like wall (Figure 2.7) [35, 48]. The latter is similar to the Bloch-point wall found in cylindrical nanowires but without the singularity of the Bloch point due to the hollow nature of the nanotube [25, 26, 49]. At present, no direct experimental evidence, such as imaging, has been reported to support these predictions.

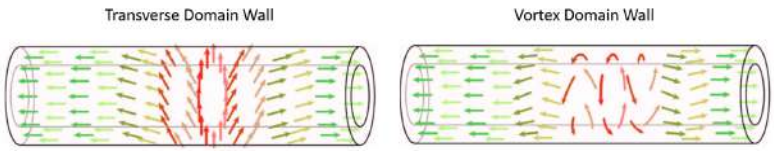

Figure 2.7: A schematic showing the expected types of DWs in nanotubes with axial magnetisation: transverse and vortex-like walls. The figure is adapted from [50].

The simulations expected to observe Vortex-Like walls in experimental imaging when they examined DWs in magnetic NTs because this type of wall is favoured in tubes with larger diameters and thin walls [35]. These geometries are the most common ones in experiments. However, transverse walls are expected to form in elemental ferromagnets such as nickel and permalloy in tubes with diameters below 50 nm, which are challenging to fabricate. Allende et al. [51] conducted a study that modelled the angular dependence of reversal modes and found that Transverse walls could occur in tubes with larger diameters when a magnetic field was applied close to a direction perpendicular to the tube axis [51]. This prediction was verified through magnetometry on arrays of tubes [50, 52].

Allende also later modelled the propagation of Transverse walls in diameter-modulated NTs with small diameters [53].

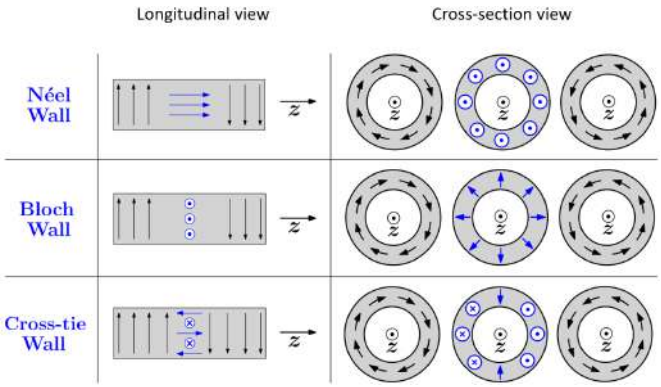

Figure 2.8: A schematic illustration of various types of domain walls (Néel, Bloch, and Cross-Tie) in nanotubes with azimuthal domains. The left panel shows a view along the tube axis (z-axis), while the right panel depicts cross-sections of a tube with two opposing azimuthal domains and the wall located in the centre. The figure is adapted from [8].

In the case of azimuthal magnetisation, attention to magnetic domains and domain walls has mostly been given to short tubes with large diameters, which are capable of sustaining azimuthal domains without the need for special magnetic anisotropy. Using micromagnetics, Lee et al. [54] modelled a short permalloy tube and discovered that it consisted of two azimuthal domains separated by a domain wall with a perceived axial magnetisation. This type of wall has been experimentally seen by Wyss et al. [38] and is referred to as the Néel wall due to its resemblance to a thin film that has been unrolled. However, the exact nature of this wall in short tubes remains controversial, as it could either be a Néel wall between azimuthal domains or an axially magnetized tube with curling ends that display a mixed state. Betancourt and colleagues [55] conducted simulations to examine the magnetisation in permalloy tubes of 500 nm in length and 500 nm in diameter, with a thickness of 50 nm. The simulations showed that the relaxed state of the tube consisted of two azimuthal domains separated by a cross-tie wall with a wall width of 30 nm. The team also explored the motion of this wall when a magnetic field was applied. Another study by Streubel and colleagues [56], which focused on rolled-up nanomembranes, also observed a similar wall. The simulation of a Ni tube with a diameter of 300 nm revealed the presence of azimuthal domains. Although the DWs were not the focus of this simulation, they were similar to the cross-tie walls seen in the other studies. Additionally, Sun and Pokrovsky [31] theoretically studied the existence of two distinct walls that could occur between azimuthal domains. The first type of wall has axial magnetisation and is referred to as a Néel wall. The second type of wall has radial magnetisation and is referred to as a Bloch wall. These walls are comparable to those observed in thin films.
Later, Stano [8] delved further into the topic of DWs, identifying three types of walls that exist between azimuthal domains, namely Néel, Bloch, and Cross-Tie. He provided both experimental evidence and simulations of tubes that exhibit these DWs. However, the type of domain wall detected by XMCD-PEEM was unclear due to the limited resolution of the method (20-30 nm). The contrasts from the XMCD-PEEM simulated images of Néel and Bloch walls were found to be very similar, with the main difference being that XMCD-PEEM could not detect an axial component of magnetisation of the Néel wall in the shadow. Based on this, Stano concluded that the detected domain wall was a Bloch wall. However, the physical tilting of the sample was not considered in

the simulation, which could affect the contrast and the shadow, causing an elongated shape and potentially leading to misidentification of the domain wall type. Although the physical tilting of the sample was not energetically favourable, there was no clear experimental evidence indicating its presence or absence. Stano also noted that the strength of the azimuthal anisotropy in the sample could diminish over time, for instance, due to ageing. As a result, certain sections of the tube may exhibit a mixture of both axial and azimuthal magnetisation, resulting in more complex magnetic arrangements that are no longer purely azimuthal [8].
In this thesis, we utilized electron holography to achieve high-resolution imaging of a domain wall. Our study was able to examine the varying states of domain walls when subjected to magnetic fields (See chapter 5). The subsequent section provides a brief overview of the theoretical and experimental findings on a single nanotube, along with an overview of the techniques utilized to study these structures.

2.1.3 Theoretical and experimental advances in nanotubes

In the previous discussion, we covered experiments that involved magnetic NTs and will continue to discuss more in upcoming sections. However, we will give a brief overview of experiments we are knowledgeable about, with a focus on tube arrays that contain nanostructures within a template or matrix, such as nanoporous alumina, as well as isolated NTs. Array experiments are typically easier to study as individual tubes are generally prepared in templates or matrices that provide mechanical stability and partial protection against oxidation. Though arrays provide a higher magnetic moment and signal, the measured quantity usually represents an average of many nanostructures with varying properties and geometry. The magnetic dipolar interactions among the tubes can impact their behaviour, and their strength can be estimated through first-order reversal curves or numerical modelling. While some techniques can access a single tube within the template, these measurements are limited to what occurs near the tube's end and can still be affected by neighbouring tubes.
Understanding the magnetostatic interactions between individual nanomagnets is crucial for comprehending the magnetic properties of an array, such as coercivity, remanence, and interactions. These interactions significantly affect the magnetic properties of the array. While traditional analysis methods rely on major magnetic hysteresis loops, which only provide information on overall behaviour, analyzing multiple minor hysteresis loops, or first-order reversal curves (FORCs), provides more localized magnetostatic information. However, the FORC method has been used by only a few studies to investigate interactions in NT arrays [14, 57–59]. Furthermore, Fernandez-Roldan et al. [60] attributed the behaviour to a weaker interaction strength due to the smaller magnetic volume of NTs when compared to NWs, and the influence of tubular geometry through the presence of an empty core and inner surface. Additionally, the thickness of the tube walls of NTs significantly affects their magnetic properties. Velazquez-Galvan et al. [61] investigated the dipolar interaction field in arrays of Ni NTs. They found that as wall thickness is reduced, the dipolar interaction field decreases while magnetic anisotropy increases. Antohe et al. [57] produced core-shell Ni/NiO NT arrays with tuned NiO layer thickness by controlling the duration of annealing processes, resulting in different NiO wall thicknesses.
On the other hand, The typical experimental method used for studying NT arrays is magnetometry, which commonly involves the use of a superconducting quantum interference device or a vibrating sample magnetometer. Bachmann et al. [50] used global magnetometry to investigate the geometry dependence of coercivity of magnetic tube arrays and observed agreement with theoretical

predictions for magnetisation reversal through nucleation and propagation of both transverse and vortex-like domain walls. Pathak et al. [62] used magneto-optical measurements with the Kerr effect to compare magnetisation reversal at tube and wire ends in arrays of Y-junction nanowires with tube segments. Tabasum [63] performed MFM to study magnetisation switching in a tube array and compared it with NW arrays. Using Mössbauer spectroscopy, several researchers [64–66] investigated different NT arrays and demonstrated that the magnetisation predominantly aligns along the tube axis. Wang et al. [40] utilized Brillouin light scattering spectroscopy on an array of Ni nanorings (nanotubes with a short aspect ratio). They found that the spin wave frequency is dependent on the axial magnetic field, with similar behaviour to thin films observed except for small fields where micromagnetic simulations predicted slightly different behaviour.

Furthermore, investigating individual NTs experimentally is more difficult compared to NT arrays. The use of porous templates in the synthesis of NTs requires dissolving the template, purifying the solution, and transferring the tubes to a suitable substrate to obtain clean and isolated NTs. In some cases, micro-manipulation is necessary to place the tubes on a suitable substrate. Patterning of the substrate and lithography may also be needed for electrical contacting. Additionally, isolated NTs produce a weaker magnetic signal than solid NWs and are more susceptible to oxidation, making it important to take measures to protect them. NTs with large diameters and thin shell thickness may require reinforcement to prevent deformation, which can be achieved through atomic layer deposition of a thin, non-magnetic layer.

Li et al. [46] studied single-crystalline Co NTs using magnetic force microscopy and observed weak uniform contrast, which they initially interpreted as a sign of flux-closure domain. However, given that the tubes were exposed to NaOH during the template dissolution, and as the NTs had thin walls, it is more likely that the tubes were oxidized and the weak contrast was of a non-magnetic origin. On the other hand, the group of D. Borkowski and P. Diehle [67] performed electron holography imaging on short magnetic tubes of hexagonal cross-section and found an axially magnetized tube with magnetisation curling at the ends (mixed state). M. Poggio, D. Grundler and M. Wyss have reported many studies on single NTs, where they performed various measurements on Ni, CoFeB, and permalloy NTs, including magnetoresistance [68, 69], cantilever torque and SQUID magnetometry [45, 70], and magnetic imaging by synchrotron X-ray magnetic microscopy [38]. They observed axially magnetised tubes with end curling states and azimuthal domains in short tubes with a sign of the Néel wall in some of them. To date, the experimental observation and study of the displacement or dynamics of DWs in axially magnetized tubes have not been reported.

In M. Stano's studies [8], he conducted similar synchrotron imaging with higher resolution to previous investigations, revealing multiple well-defined domains and DWs. He also performed magneto-optical measurements and magnetic force microscopy, which showed a clear magnetic signal. In addition, he used electron holography to investigate higher aspect ratio CoNiB and NiFeB tubes. In aged CoNiB electroless tubes, he observed a decrease in the azimuthal anisotropy strength and strange phase patterns, which may be attributed to DWs. However, the phase shift extracted from electron holography did not resemble simple Bloch walls or other common types, likely because the electrostatic and magnetic phase contributions were not separated in the measurements.

The CoNiB ferromagnetic nanotubes with azimuthal magnetisation were investigated in a study by our group with D. Tiwari [71], which fabricated the tubes through electroless plating in polycarbonate porous templates. The nanotubes varied in length, diameter, and wall thickness, with lengths of several tens of micrometres, diameters ranging from 100 to 500 nm, and wall thicknesses ranging from 10 to 80 nm. The nanotubes had a resistivity of around $1.5 \times 10^{-6}\,\Omega\cdot\mathrm{m}$ and showed an anisotropic magnetoresistance (AMR) of 0.2 to 0.3 %, one order of magnitude larger than the bulk

material due to resistance at grain boundaries. By analyzing M(H) AMR loops of single tubes contacted electrically, the authors determined the azimuthal anisotropy field, which had a magnitude of around 10 mT and increased with the tube wall thickness and Co content but not significantly with diameter or curvature. The study also reported on the tubes' structural and electric properties, in addition to the magnetic properties.
This thesis will explore electroless-plated CoNiB nanotubes identical to those studied by D. Tiwari et al. [71] and earlier by Stano. All nanotubes under consideration will share the same tube length of 30 µm, but vary in diameter and thickness. We intend to conduct a comprehensive analysis of their structure and chemical composition. Our investigation will include magnetic imaging conducted through Lorentz microscopy and electron holography under applied magnetic fields, utilizing the advanced TEM microscope due to its superior spatial resolution in comparison to X-ray-based techniques. The study anticipates providing clear experimental evidence of a domain wall between azimuthal domains, along with proof of curling at the tube ends in the case of an axially magnetized tube (the mixed state).

2.1.4 Nanotubes synthesis and materials

To synthesize nanotubes, bottom-up methods, which employ chemical-based methods like filling nanoholes or coating nanopillars, are commonly used. Templates such as porous membranes or arrays of pillars/wires offer better control over the geometry of the nanostructures, making them the preferred choice. Although chemical syntheses without the use of templates are also available, they are less prevalent. Lithography is a top-down approach that can be used to produce tubular structures; however, it is less efficient and has limited capabilities in terms of geometric parameters. A variety of fabrication techniques exist for creating cylindrical geometries like nanotubes and nanowires, such as Focused-electron-beam-induced deposition (FEBID) [72]. However, this thesis will focus only on the electroless plating deposition, which is the main method used in this thesis.
Template materials like porous alumina, mica, and track-etched polymeric templates like Polycarbonate and Poly-Ethylene Terephthalate are commonly employed. In this study, we used polycarbonate templates with electroless plating to fabricate CoNiB nanotubes. For more information about the preparation of these templates and nanotube fabrication using other techniques, please refer to the cited references [11, 13, 73].

2.1.4.1 Electroless plating deposition

Ferromagnetic nanotubes can be fabricated by a method called electroless plating deposition. In this process, a catalytic seed layer is first deposited onto a substrate, followed by the deposition of a magnetic material, such as cobalt or iron, by an electroless plating method. The seed layer acts as a template for the growth of the nanotube. The diameter, length, and wall thickness of the nanotube can be controlled by adjusting various parameters of the deposition process, such as the concentration of the plating solution, the temperature, and the deposition time.
One of the advantages of electroless plating deposition is that it can produce uniform and well-defined NTs with high aspect ratios. Moreover, the process can be easily scaled up for mass production. Ferromagnetic NTs of CoNiFeB and CoNiB can be fabricated using electroless plating deposition, a process that involves the reduction of metal ions onto a substrate without the use of an electrical current. This method provides a way to create uniform and well-controlled nanotube structures. One of the key advantages of this method is the ability to synthesize CoNiB NTs with

precise control over their diameter and wall thickness. In a typical process, a polycarbonate template is used to guide the deposition of the metal ions onto the substrate, which is then reduced to form the nanotube structure.
The key advantages of electroless-plated NTs include easy tuning of nanotube geometrical parameters such as tube length and diameter by manipulating the size of the pores and flexible targeting of tube-wall thickness by controlling the deposition time. In addition, the material-growth deposition is radial, poly-crystalline and has shown homogeneous wall-thickness and composition (Figure 2.9) [74, 75].

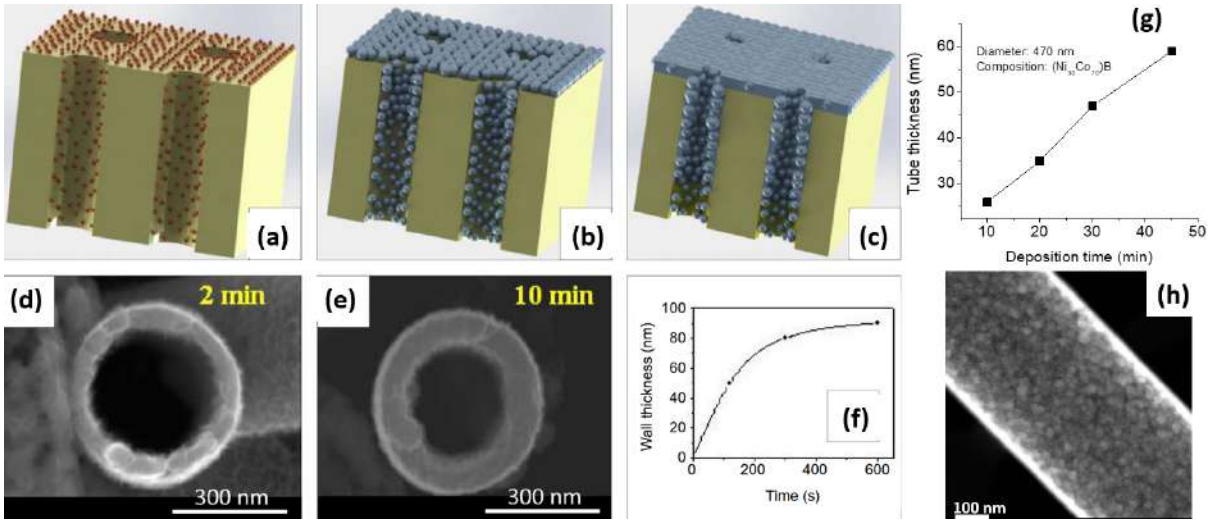

Figure 2.9: A figure presents a 3D artistic representation of the various phases of growth of CoNiFeB alloy nanotubes, denoted as (a-c). The first phase involves the nucleation of nanoparticles from the Pd catalyst, while the second phase depicts the growth of these nanoparticles. The third and final phase involves percolation and film formation. SEM images of nanotube walls deposited for two and 10 min are shown in panels (d) and (e), respectively. Panel (f) illustrates the correlation between the deposition time and the thickness of the nanotube walls. (g) The tube thickness variation with the deposition time. The thickness can be targeted by controlling the deposition time of the growth. (h) Scanning Transmission Electron Microscopy (STEM) image of the studied nanotube (diameter = 470 nm, thickness = 60 nm). (a-f) are adapted from [75].

Electroless plating in ion track-etched polycarbonate membranes was used to make various batches of CoNiB NTs, with different compositions and diameters (140, 470 nm). Firstly, the polycarbonate foils are irradiated by heavy ions, resulting in latent damage tracks that are more sensitive to chemical etching than the bulk polymer. Following treatment in a NaOH solution, cylindrical pores are formed, which are utilized as templates for the synthesis of nanotubes. Catalytically, active Pd nanoparticles are deposited on the membrane surface by immersing the membrane in Sn(II)- and Pd(II)-containing solutions, alternatively to initiate the electroless deposition reaction. Electroless plating is next used to deposit the membrane pores' walls with CoNiB. The Ni to Co ratio is adjusted in this case by adjusting the relative concentration of each metal precursor in the plating solution [74].
The electroless plating process was expertly conducted by DR. MARTIN CHRISTOPH SCHEUERLEIN and DR. WOLFGANG ENSINGER in Dramstadt, Germany. Following the successful plating, the polycarbonate membranes were dissolved in our laboratory. This was accomplished using

dichloromethane, effectively freeing the nanotubes from the membranes. The resultant nanotubes were then spread onto both TEM carbon grids and SiO substrates for the purpose of TEM imaging and focused ion beam (FIB) fabrication, respectively.

Chapter 3

Methods and instrumentation

3.1 Transmission Electron Microscopy

Transmission Electron Microscopy (TEM) is a microscopy technique that uses a beam of electrons to visualize structures and features at a nanometer scale. Unlike light microscopy, TEM leverages the wave-like properties of electrons that are accelerated to very high energies to attain resolutions of several orders of magnitude greater. TEM is widely used in nanoscience for the detailed analysis and characterization of nanostructures. The technique offers many methods, such as diffraction, imaging, spectroscopy, Lorentz microscopy, and electron holography, to provide a comprehensive understanding of the magnetic properties of nanostructures. This versatility and high spatial resolution have made TEM an invaluable tool in materials science and nanotechnology research [76–78].
The image formation process in a TEM involves several interconnected stages (Figure 3.1.a). Initially, an electron beam is generated from a source and accelerated. The beam (electron probe) is then directed towards the specimen. This electron probe then interacts with the specimen, leading to electron scattering and a diffraction pattern in the back focal plane of the objective lens. Subsequently, the specimen's image is formed in the image plane and finally is magnified and projected onto the detector plane.
The generation of an electron beam is achieved through either thermionic emission, where a tungsten or LaB_6 filament is heated to produce electrons, or field emission, which employs a small tungsten tip. Field emission can occur at room temperature, known as a Cold Field Emission Gun (CFEG), or under heated conditions, known as a Schottky Field Emission Gun (SFEG). Both CFEG and SFEG produce a highly coherent and bright electron beam, which is essential for advanced techniques such as electron holography that utilize the coherence of electrons. In contrast, while thermionic emission provides a high-intensity beam, it offers reduced coherence [76]. In a TEM, the generated electrons are accelerated to a voltage range of 60 to 300 kV, decreasing their wavelength. Following this, the electron beam passes through various lenses, deflecting coils, and stigmators, which control the probe size, convergence angle, and electron dose of the beam.
TEM operates by deploying a high-energy beam of electrons, which, upon interaction with a specimen, engenders a diverse array of signals (Figure 3.1.b). Each signal emanates different information regarding the specimen and can be detected and analyzed to procure a characterisation of the material in question. The signals include the direct (transmitted) beam, elastically and inelastically scattered electrons, Auger electrons, visible light, secondary electrons, X-rays, and backscattered electrons. Their collective interpretation provides detailed insights into the physical and chemical properties of the material, underpinning TEM's versatility and comprehensive applicability in

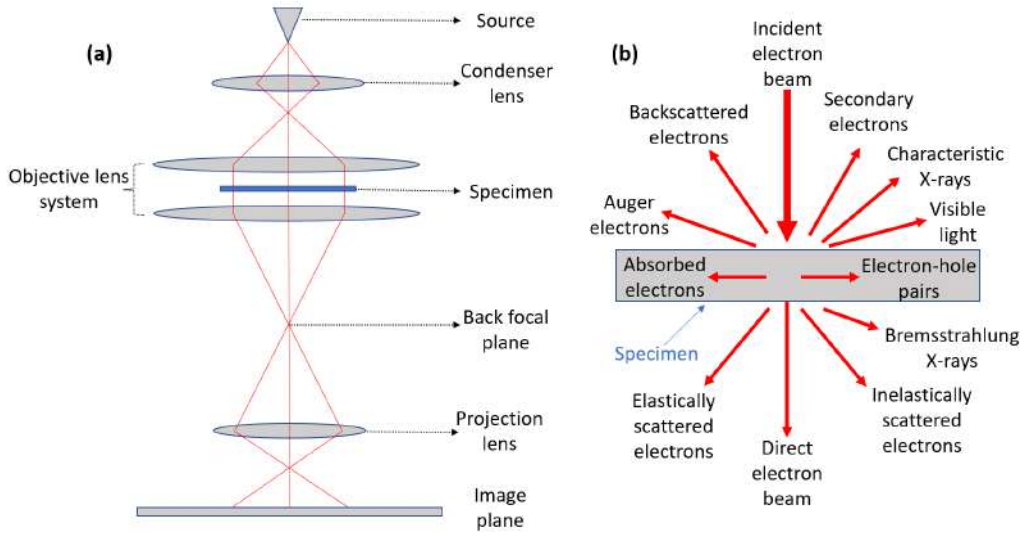

Figure 3.1: (a) A schematic illustrating the path of the electron beam in a TEM. (b) Depicts the complex interactions between the electron beam and the specimen, leading to the generation of diverse signals. (b) is adapted from [76].

material science and nanotechnology [76].

The portion of the electron beam that passes through the specimen without significant interaction with the material's atomic structure is referred to as the direct or transmitted beam. This beam has experienced minimal deflection or energy loss, thus maintaining its initial direction and energy. Notably, the transmitted beam can retain valuable information about the specimen's structure, density, and composition, contributing significantly to the comprehensive analysis offered by TEM. Thus, some electrons from the incident beam are deflected by the specimen, a process that can either leave their kinetic energy unchanged (elastic scattering) or result in a loss of kinetic energy (inelastic scattering). Elastically scattered electrons contribute to diffraction patterns and high-resolution images, while inelastically scattered electrons, via their energy loss characteristics, can reveal information about the specimen's elemental composition and electronic structure. When the incident beam ejects an inner-shell electron in an atom of the specimen, a characteristic X-ray is emitted as a higher-energy electron falls into the resultant vacancy. This process forms the basis for techniques like Energy-Dispersive X-ray Spectroscopy (EDS), which reveals elemental composition information. In a related process, the energy released from the electron falling into the vacancy can also be transferred to a second electron, leading to the ejection of the second electron, known as an Auger electron. The interaction of the electron beam with the specimen may also result in the emission of visible light, a phenomenon called cathodoluminescence, which is helpful in investigating the optical properties of materials. Furthermore, ionizing interactions of the incident beam can cause the ejection of low-energy electrons from the specimen, known as secondary electrons, typically used in Scanning Electron Microscopy (SEM) to generate high-resolution images. Additionally, the deceleration or 'braking' of incident electrons by atomic nuclei within the specimen leads to the emission of non-characteristic X-rays, known as Bremsstrahlung X-rays. An additional important signal comes from backscattered electrons. These are incident electrons that, following elastic interactions with the atomic nuclei in the specimen, are scattered back out. The intensity of backscattered electrons is proportional to the atomic number of elements in the specimen, providing compositional contrast. This is often called Z-Contrast, 'Z' being the scientific symbol for

atomic number.

3.1.1 Scanning Transmission Electron Microscopy (STEM)

Scanning Transmission Electron Microscopy (STEM) is a microscopy technique that enables the investigation of materials at the atomic level. It is widely used in various disciplines, such as materials science, physics, biology, and chemistry [76, 78].
STEM is based on similar principles as conventional TEM but differs in the image formation method. While TEM projects the transmitted electrons onto a detector in one step, STEM scans the sample with a focused beam in a raster pattern and collects the signal at each point to form the image sequentially. STEM allows the simultaneous acquisition of multiple signals, such as bright-field, dark-field, and high-angle annular dark field (HAADF) images. A key advantage of STEM over TEM is the generation of Z-contrast images using HAADF, which depends on the Rutherford scattering of electrons by heavier atoms. Thus, HAADF-STEM images show contrast based on the atomic number (Z) of elements, enabling quantitative analysis. Moreover, STEM can perform elemental mapping through Electron Energy Loss Spectroscopy (EELS) and Energy Dispersive X-ray Spectroscopy (EDX). These tools allow STEM to identify the elemental composition at each scanned point, providing detailed insights into the spatial distribution of elements at sub-nanometer resolution. More details about EELS and EDX are discussed below.

3.1.1.1 Energy Dispersive X-Ray Analysis (EDX)

Energy-Dispersive X-ray Spectroscopy (EDX or EDS) is an analytical technique for elemental analysis or chemical characterisation of materials at the micro and nanoscale. It is often combined with electron microscopy techniques such as SEM or STEM to provide insights into the elemental composition of a sample [76].
EDX is based on the interaction of a high-energy beam of charged particles or X-rays with the atoms in the material. This excites the atoms and causes electrons from the inner shells to leave vacancies. As the atom stabilises, electrons from outer shells fill these vacancies and emit characteristic X-rays, which serve as an elemental fingerprint. These X-rays are detected and converted into a spectrum that shows the number of X-rays at various energy levels. Since each element has a unique set of peak energies, this spectrum reveals the sample's elemental composition. Quantitative data can be extracted from EDX spectra by comparing the X-ray counts of each element's peaks. By using standard samples, a calibration curve can be developed to quantify each element's presence in an unknown sample.
We used EDX as the main technique for chemical analysis on the studied nanotubes in collaboration with DR. FLORIAN CASTIONI. For detailed results, see Chapter 4.

3.1.1.2 Electron energy-loss spectroscopy (EELS)

Electron Energy Loss Spectroscopy (EELS) is a powerful and sophisticated analytical technique for investigating the chemical, electronic, and optical properties of materials at the microscopic and even atomic scale. It is widely used in materials science and other fields, such as biology, nanotechnology, and thin film research. Figure 3.2(a) shows the setup of EELS equipment on a Transmission Electron Microscope (TEM) with a post-column arrangement. A magnetic prism,

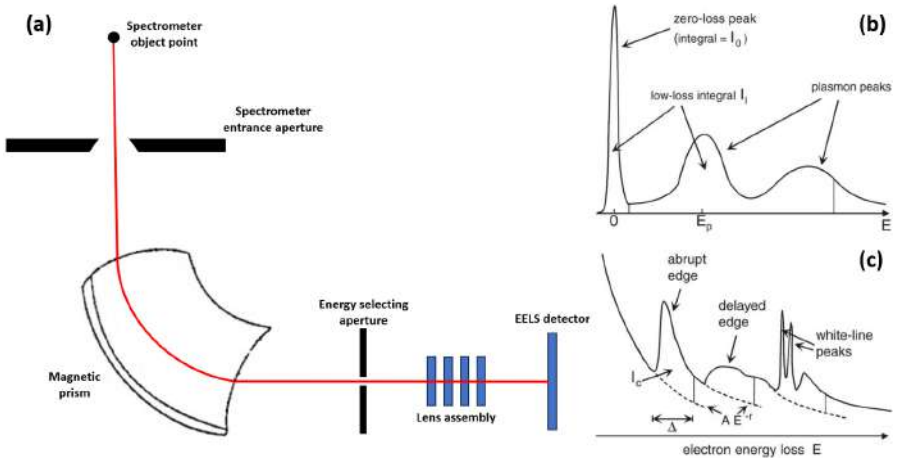

Figure 3.2: (a) An illustration showcasing the Electron Energy Loss Spectroscopy (EELS) equipment strategically positioned in a post-column setup on a Transmission Electron Microscope (TEM). A key feature of this setup is a magnetic prism, typically set at a 90-degree angle, employed for electron deflection. Panels (b) and (c) represent EELS spectra: in panel (b), the low-loss region is displayed, while panel (c) emphasizes the core-loss region. Importantly, within the core-loss region, the ionization edges and their associated backgrounds are highlighted, with the latter distinguished by dashed lines. (b) and (c) adapted from [79]

usually at a 90-degree angle, deflects the electrons. J.C. Slater and H.F. Kromminga introduced EELS in 1940 [76, 79].

EELS measures the energy loss of a beam of high-energy electrons after interacting with a sample. The technique directs a focused electron beam at the sample and collects and analyzes the scattered or absorbed electrons. The energy loss reveals the local electronic structure, bonding, density of states, and elemental composition and oxidation states of the sample.

EELS has two primary modes: low-loss and core-loss spectroscopy. Figure 3.2(b) illustrates low-loss EELS, which measures the energy distribution of electrons with small energy losses (less than 50 eV). It provides information about plasmons, band structure, and other low-energy excitations. Figure 3.2(c) depicts core-loss EELS, which probes energy losses from 100 eV to several thousand eV. It offers detailed elemental, chemical, and bonding information based on the ionization edges of specific atomic shells.

EELS has several advantages, such as providing chemical information with high spatial resolution and detecting light elements that are difficult to identify with other techniques, such as EDX. EELS can measure the specimen thickness and the surface layers of materials, distinguishing between different oxidation states of an element. This capability helps understand the chemical behaviour of materials.

EELS is often used with other imaging techniques, such as TEM or STEM, to obtain a comprehensive picture of the sample. These techniques can acquire both structural and chemical information about the sample. However, EELS also has some limitations. The samples need to be thin enough for the electrons to transmit, requiring careful specimen preparation. Interpreting EELS data can be complex due to overlapping and broadened ionization edges and artefacts from the electron scattering in the sample.

In collaboration with DR. HANAKO OKUNO, we used EELS to investigate the chemistry of the nanotubes and measure the sample thickness using EELS in EFTEM mode. We present the detailed

results in Chapter 4.

3.1.2 Magnetic imaging in TEM

Magnetic imaging in TEM enables the direct visualization of magnetic structures and domains at the nanoscale. The electron beam experiences a deflection due to the magnetic Lorentz force. This results in a magnetic contrast in the transmitted electrons, which can be detected and analysed to obtain information about the sample's magnetic properties. By measuring the changes in the phase of the transmitted electrons, the sample's magnetic properties can be deduced, providing information about the local magnetisation and its distribution. This technique has been used to investigate phenomena such as domain wall motion, magnetisation reversal, and magnetic coupling in nanostructures. In recent years, the development of electron holography and Lorentz microscopy has greatly improved the spatial resolution and sensitivity of magnetic imaging in TEM, making it a powerful tool for investigating the properties of magnetic materials at the nanoscale [76, 77, 80]. The phase is shifted when an electron interacts with an electromagnetic field. Conventionally, the initial phase shift is assumed to be zero, and the Aharanov-Bohm equation (ABE) describes how the interaction of electrons with a sample leads to a phase shift containing information about the magnetic vector potential and the electrostatic potential of the sample. The ABE incorporates two contributions to the phase shift, the magnetic phase shift ($\phi_{\mathrm{M}}(x,y)$) and the electrostatic phase shift ($\phi_{\mathrm{E}}(x,y)$), and it can be expressed as follows [76–78, 81, 82]:

$$\phi(x,y) = \phi_E(x,y) + \phi_M(x,y) = C_{\mathrm{E}} \int V(\mathbf{r})\, dz - \frac{e}{\hbar} \int A_z(\mathbf{r})\, dz \tag{3.1}$$

Where $A_z(\mathbf{r})$ is the z-component of the magnetic vector potential $\mathbf{A}$ ($\mathbf{z}$ represents the beam direction), and C_{E} is a constant that depends on the accelerating voltage of the microscope and takes on different values for different voltages. At acceleration voltages of 300 kV and 200 kV, C_E has values of $6.256\,\mathrm{V^{-1}\mu m^{-1}}$ and $7.288\,\mathrm{V^{-1}\mu m^{-1}}$, respectively [81–83].
Various magnetic imaging techniques in TEM, including electron holography and Lorentz microscopy, share a fundamental sensitivity to the transverse components of magnetic induction. This principle depends on the interactions between the sample's magnetic field and the electron beam. Specifically, the phase shift experienced by the electrons, which is integral to these techniques, is determined by the line integral of the magnetic vector potential ($\mathbf{A}$) along the path of the electron beam. Importantly, these TEM techniques are sensitive only to the $\mathbf{A}$ component parallel to the electron path. Consequently, their imaging capabilities primarily respond to the components of the magnetic field that are perpendicular to the electron beam path, which is often referred to as their focus on the 'transverse' or 'perpendicular' components of magnetic induction. In cases of a purely two-dimensional magnetic field (*i.e.*, $B_z = 0$) confined to the (xy)-plane, with A_z being the only component of the magnetic vector potential, the relationship between A_z and the perpendicular magnetic induction $\mathbf{B}_\perp$ (components B_x and B_y) is defined as $B_x = \frac{\partial A_z}{\partial y}$ and $B_y = -\frac{\partial A_z}{\partial x}$. Additionally, they leverage this transverse sensitivity to measure the phase shift of the electron beam, enabling a detailed mapping of a specimen's magnetic configuration, including the surrounding stray fields. Nevertheless, it is essential to note that the detected phase shift represents a projection and an integration of the potentials along the electron beam path [83]. Therefore, the relationship between $\mathbf{A}$ and $\mathbf{B}_\perp$ allows for the following expression:

$$\phi_M(x,y) = -\frac{e}{\hbar} \iint B_\perp(\mathbf{r})\, dxdz \tag{3.2}$$

An accurate knowledge of the sample thickness is essential for the correct interpretation of collected data in TEM magnetic imaging techniques, particularly when studying materials like CoNiB nanotubes. A comprehensive study on the determination of nanotube thickness using TEM can be found in Chapter 4, providing valuable insights and methodologies for thickness measurements in similar materials. The development of advanced TEMs with Cs-aberration correctors, advanced optical devices designed to compensate for spherical aberrations (Cs), has further expanded the scope of TEM by allowing for the study of electronic and magnetic properties with even higher resolution. This knowledge paves the way for further advancements in magnetic imaging by TEM, enhancing the reliability and precision of the analysis [76, 77].

3.1.3 Electron holography

In conventional TEM, only the intensity distribution of the electron wave is recorded, causing the phase information to be lost. This means that information about the electron beam's phase shift from the electromagnetic fields due to the Aharonov-Bohm effect cannot be obtained. Electron holography is an imaging technique that allows for the phase shift of the electron wave resulting from the sample interaction to be accessed, providing information about local variations in magnetic induction and electrostatic potential. The concept of electron holography was proposed by Denis Gabor in 1948 to improve the limitations of electron microscopy caused by aberrations in electromagnetic lenses. There are several types of electron holography with different microscopy setups. In this thesis, we use off-axis electron holography, detailed in this section.

3.1.3.1 Off-axis electron holography

Off-axis electron holography (EH) is a cutting-edge TEM technique offering a comprehensive, high-resolution electromagnetic field analysis within and around nanostructured materials. This technique has the unique and advanced ability to reveal spatial variations in electrostatic and magnetic potentials, contributing significantly to fields such as materials science, physics, and nanotechnology [76, 77, 84].

EH operates on the principle of interference. An electron beam, generally sourced from a field emission gun (FEG) due to its superior brightness and coherence, is divided into two coherent beams: an object beam, which traverses through a specimen, and a reference beam, which passes through the vacuum. Following this, the coherent beams are overlapped using an electrostatic biprism, also known as a Möllenstedt biprism, to enable the interference process [85, 86]. The term 'off-axis' thereby refers to the spatial separation of the object and reference beams across the plane perpendicular to the beam direction, a necessary condition for their interference. Electromagnetic lenses are applied post-beam-splitting to manage the paths of the object and reference waves, ensuring their successful overlap to form the interference pattern or hologram (Figure 3.3). Following the formation of the interference pattern, a detector, typically a Complementary Metal-Oxide-Semiconductor (CMOS) camera, is used to record the hologram. The captured hologram, embodying information about the electron wave's phase and amplitude, is subsequently reconstructed into an image. Optimal tuning of the biprism voltage ensures the best overlap and resulting interference pattern. In this manner, the object and reference beams are recombined, resulting in an interference pattern or hologram.

The application of a numerical reconstruction algorithm to this hologram enables the recovery of the electron wave and the calculation of the phase shift caused by the sample. Mathematically,

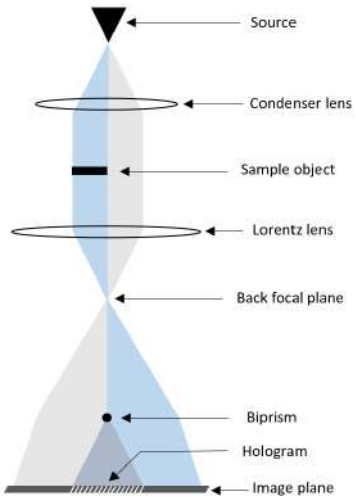

Figure 3.3: A schematic representation of the process of electron holography, which involves manipulating and recording an electron beam to generate a holographic image.

let's consider two coherent waves travelling in the z-direction. One wave is the reference wave represented by $\psi_{\text{ref}}(\mathbf{r}) = A_{\text{ref}}(\mathbf{r})e^{i2\phi\mathbf{k}\cdot\mathbf{r}}$, while the other is the object wave represented by $\psi_{\text{obj}}(\mathbf{r}) = A(\mathbf{r})e^{i(2\phi\mathbf{k}\cdot\mathbf{r}+\phi(\mathbf{r}))}$, where $\mathbf{r}$ signifies the position vector, and $\mathbf{k}$ denotes the wave vector. $A_{\text{ref}}(\mathbf{r})$ and $A(\mathbf{r})$ are the amplitudes of the reference and the object, respectively.
The intensity of the wave function produced by the interference of these waves along the x-axis at $z = 0$ can be expressed as:

$$I_{\text{holo}}(x,y) = |A_{\text{ref}}(x,y)|^2 + |A(x,y)|^2 + 2\cdot A_{\text{ref}}(x,y)\cdot A(x,y)\cdot\cos\left(2\pi\frac{\alpha_{\text{d}}}{\lambda}x + \phi(x,y)\right) \tag{3.3}$$

The intensity of the hologram image encapsulates both the conventional bright field image, represented by the amplitude terms, and a cosine term that carries information about the phase shift. This equation describes the interference fringe pattern of the hologram, where the fringes' periodicity ($\frac{\alpha_{\text{d}}}{\lambda}$) depends on the deflection angle (α_{d} and $-\alpha_{\text{d}}$) caused by the biprism for the reference and object waves. The transformation of a conventional bright field image into Fourier space results in a central spot, also known as the direct beam or central band. Conversely, the Fourier transform of a hologram image reveals a central band and two additional collinear spots, referred to as sidebands, which are equally displaced from the centre band. The sidebands are where the information about the transmitted wave's phase and image amplitude is stored. By selecting one of the sidebands and performing an inverse Fourier transform after centring on the spatial frequency of the fringes, one can obtain information about both the amplitude and phase shift of the object's electron wave.
EH has found extensive applications in various domains, from material science [87–95] to biological research [96–98] and many other studies [83, 99–107].

3.1.3.2 Phase reconstruction

The extraction of phase shift and amplitude information from a hologram through a series of steps is shown in Figure 3.4. First, the recorded hologram (Figure 3.4.a) undergoes a Fast Fourier Transform (FFT) to convert it from the spatial domain to the spatial-frequency domain (Figure 3.4.b).

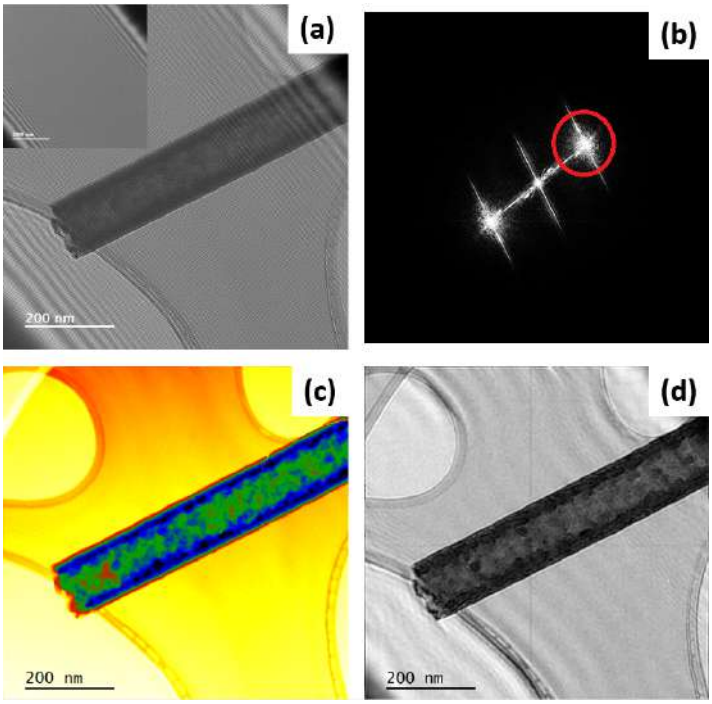

Figure 3.4: The phase reconstruction process. (a) A hologram image of a nanotube and a reference image (in the inset) of a nanotube electron holography data. (b) The FFT image of the hologram and the sideband is selected in red. (c) and (d) show the reconstructed phase (Unwrapped) and amplitude images, respectively.

The FFT produces a Fourier spectrum with a central beam and two sidebands. One of the sidebands, which contains the essential phase shift and amplitude information, is shifted to the zero frequency and isolated using a Fourier mask. Then, an inverse FFT is applied to the masked sideband, resulting in amplitude and phase images, as seen in Figure 3.4.(c) and (d). The phase image shows the variations in the interference fringes' periodicity relative to a reference area. Each fringe in the phase image initially corresponds to a phase shift of 2π radians. To avoid ambiguities from phase values exceeding a full wave of phase shift, phase unwrapping is performed to obtain a continuous phase map that reflects the electromagnetic field within the specimen. The phase image in Figure 3.4.(c) is already unwrapped.

The choice of mask size in the inverse FFT step affects both the resolution and the signal-to-noise ratio of the final complex image (amplitude and phase). An optimal trade-off between these two factors is required. Phase distortions from the microscope and detection system, such as Fresnel fringes from the biprism, projector lenses, and the camera's optical fibres, must also be considered. A reference hologram from an empty area serves as a control, containing only the phase shift from the TEM column artefacts. Subtracting this from the reconstructed phase image of the object removes the phase distortions from the microscope setup.

The reconstruction stage is crucial in electron holography because it reveals the phase data related to the specimen's electromagnetic field. We used custom scripts on Gatan© Digital Micrograph by DR. CHRISTOPHE GATEL for the reconstruction, but the approach can be adapted depending on the research goal and the computing resources.

3.1.3.3 Separation of phase contributions

The phase image from electron holography data shows the phase shift, which has two main parts: the electrostatic and magnetic phase shifts. They reveal the specimen's electromagnetic properties. We can separate these phase shifts using different methods [108, 109].
One method is to flip the sample (Figure 3.5). This works because vectors and pseudo-vectors (or axial vectors) behave differently when flipped. The magnetic phase shift depends on the sample's magnetisation, which is a pseudo-vector. Flipping the sample changes the sign of the magnetic phase shift in the image. The electrostatic phase shift, related to the electric potential (a scalar), does not change when the sample is flipped. This lets us separate the two phase shifts.
Another method is to apply an external magnetic field along the axis of a nanotube, for example (Figure 3.5). This works because the magnetic field affects the magnetic phase shift but not the electrostatic phase shift. Applying a magnetic field in positive and negative directions gives us two images with different magnetic phase shifts. The electrostatic phase shift, based on the sample's internal potential, stays the same. We can separate the two phase shifts by comparing the images under opposite magnetic fields.
To separate the phase shifts, we need to align the images well. This matters when we compare images under different conditions, like flipping or changing the magnetic field. We used an ROI line to align the images at the same location. Then we added and subtracted them to separate the phase shifts. By adding the images of the Up and Down images, or the Positive and Negative Magnetic Field states, we separated the magnetic phase shifts and kept the electrostatic phase shifts. There are other methods to separate the phase shifts[76, 77, 84]. We used the flipping and magnetic field methods in our research.

3.2 Scanning transmission X-ray microscopy (STXM)

Scanning Transmission X-ray Microscopy (STXM) is a technique that combines the penetration of X-rays and the resolution of microscopy to analyze various materials, such as biological cells, thin films, and nanostructures. Figure 3.6 illustrates the operation of STXM. STXM can produce detailed, three-dimensional images of these samples at the nanometer scale [77, 110].
The operation of STXM involves scanning a highly focused X-ray beam across a sample and monitoring the transmitted intensity as a function of position and energy. The small size of the beam, typically in the range of 10-30 nanometers, enables high-resolution imaging. This is achieved by using a specialized X-ray optic, such as a zone plate, a diffractive lens comprised of concentric rings, which can focus the monochromatic X-ray beam to a tiny focal point on the sample, as shown in Figure 3.6. The spatial resolution of the resultant image is defined by the spot size, which in turn is governed by the width of the outermost zones of the zone plate.
STXM measurements are performed at synchrotron radiation sources, favoured for their high-intensity, tunable X-rays. In a standard synchrotron STXM setup, X-ray photons emitted by a synchrotron storage ring first pass through a monochromator to select a narrow band of X-ray energies. The X-rays are then focused onto the sample using a Fresnel zone plate. The sample, mounted on a precision stage that can move in the x, y, and z directions with nanometer precision, is scanned through the focused X-ray beam. A detector downstream of the sample then collects the transmitted X-rays and records their intensity as a function of position and energy, providing the necessary data for image and spectral analysis.

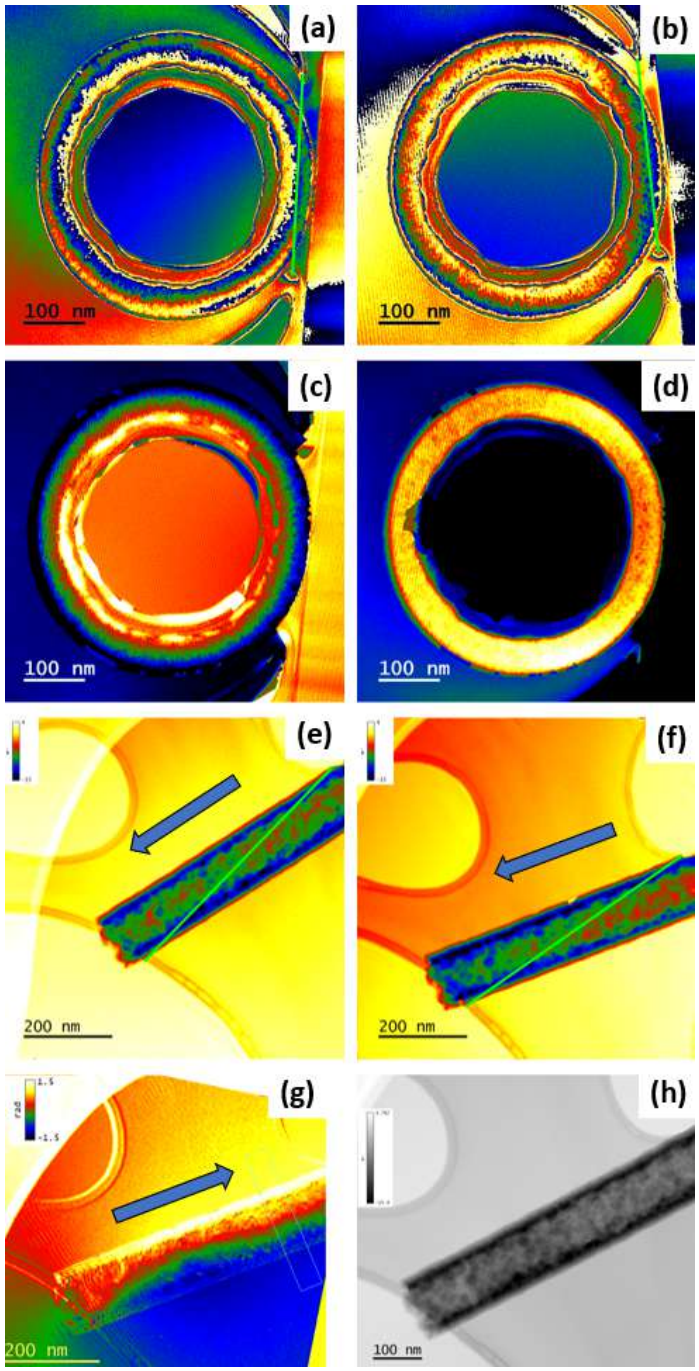

Figure 3.5: This figure shows two methods of separating the magnetic and electrostatic phase shifts in a nanotube sample. The first method involves flipping the sample within the microscope, resulting in inverted magnetic phase signs and constant electrostatic contributions. The second method involves applying an external magnetic field in opposite directions along the nanotube axis, resulting in distinct magnetic phase shifts and constant electrostatic contributions. The images are labelled as follows: (a) and (b) are phase images before and after flipping, respectively; (c) and (d) are the separated magnetic and electrostatic phase shifts, respectively; (e) and (f) are the phase maps under positive and negative magnetic fields (the blue vectors), respectively; (g) and (h) are the separated magnetic and electrostatic phase shifts, respectively. The green ROI lines in the images were used to align before the separation of the phase images.

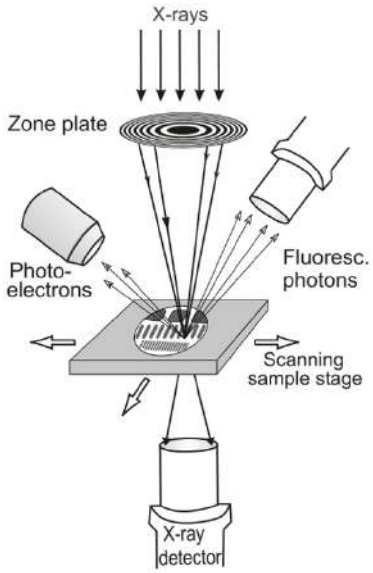

Figure 3.6: This figure illustrates the operation of Scanning Transmission X-ray Microscopy (STXM). In this technique, a monochromatic X-ray beam is narrowed to a tiny focal point using an appropriate X-ray optic, as exemplified by a zone plate in this diagram. The sample is then systematically moved across the focal point of the X-ray beam. The spatial resolution of the resultant image is defined by the spot size. The image contrast is achieved by measuring either the intensity of the transmitted X-rays, the sample's fluorescence, or electron yield, all as functions of the sample's position. This figure is adapted from [110].

Furthermore, STXM combine X-ray Absorption Spectroscopy (XAS) and X-ray Magnetic Circular Dichroism (XMCD) to study the chemical and magnetic properties of samples. XAS uses the energy-dependent absorption of X-rays by core-level electrons to probe the local atomic structure, electronic state, and oxidation state of a material. In STXM, XAS spectra are collected from different regions of the sample using circularly polarized light, creating a spatial map of the chemical state. This is useful for examining heterogeneous samples and phenomena such as chemical gradients or phase boundaries at the nanoscale.
XMCD measures the difference in absorption of left- and right-circularly polarized X-rays by a magnetic material, which reflects the alignment of the magnetic moments in the sample. In STXM, XMCD measurements are obtained by acquiring two images at the same energy but with different circular polarizations. The difference between these images gives the XMCD signal, which can be analyzed to infer the magnetic state of the material. With the spatial resolution of STXM, XMCD-STXM can reveal magnetic domains, domain walls, and other magnetic structures at the nanoscale, thus providing a comprehensive understanding of the sample's magnetic properties [77, 110].
During the measurement, the radiation is focused and monochromatized to produce a narrow energy bandwidth, and the energy of the X-ray beam is tuned to cover the Co and Ni L_2 and L_3 absorption edges. These edges correspond to the $2p_{1/2}$ and $2p_{3/2}$ core electron levels, with the Co L_3 edge at approximately 778 eV, the Co L_2 edge at around 793 eV, the Ni L_3 edge near 852 eV, and the Ni L_2 edge at about 870 eV. The nanotube sample absorbs X-ray photons, exciting core electrons to unoccupied states. The intensity of the transmitted beam is measured, and the resulting transmission data is analyzed to obtain the X-ray absorption spectrum, which displays the Co and Ni transition edges as characteristic absorption peaks. For alloys like Py or $Co_{20}Ni_{80}$, more robust

signals are possible by measuring at the Fe or Co L_3 edge, respectively, rather than the Ni L_3 edge, even with more Ni atoms available for electron excitation. The XAS image, which represents the absorption, is obtained by averaging the I^+ and I^- images. This captures the absorption signal from both circularly polarized light directions. The XMCD image, which indicates the element-specific magnetic properties, is obtained by normalizing the difference between the I^+ and I^- images by their summation. This highlights the XMCD contrast between the two circularly polarized light directions, revealing information about the material's magnetic moment, orientation, and domain structure. By extracting the XAS and XMCD images through these calculations, we can gain valuable insights into the electronic and magnetic properties of the nanotubes.

3.3 Sample preparation for TEM

3.3.1 Dissolving of the nanotube membranes

Sample preparation is vital in TEM studies. It requires several meticulously handled steps to secure a sample that is of high quality and free from artefacts. It becomes all the more essential when dealing with nanotubes, which can be challenging due to their small size and propensity to aggregate.

The procedure begins with the disintegration of the nanotubes' embedding medium. For instance, in the case of CoNiB nanotubes that are typically grown in a polycarbonate membrane, a solvent such as dichloromethane is employed. Dichloromethane is particularly effective at dissolving the polycarbonate membranes, resulting in the nanotubes being liberated into the solution. One common method involves depositing a tiny droplet of the solution that contains the nanotubes onto a carbon grid. Once the droplet dries, the nanotubes adhere to the carbon substrate, ready to be imaged using TEM. The solution is deposited on a carbon grid along with ethanol and acetone.

In this scenario, dichloromethane is employed for the dissolution of the membrane, while ethanol and acetone are used during the cleaning process. These solvents serve a dual purpose: they aid in evenly dispersing the nanotubes on the TEM grids and help mitigate the aggregation of nanotubes. This results in enhanced quality of the TEM images.

Ensuring the nanotubes are uniformly dispersed on the carbon substrate is vital, as any clumps or aggregates could skew the results. Utilizing high-quality solvents and carbon grids and maintaining cleanliness during sample preparation are measures that can help minimize the risk of artefacts.

3.3.2 Focused Ion Beam (FIB) fabrication

Focused Ion Beam (FIB) fabrication is a technique for creating nanoscale structures with high precision. The FIB fabrication of cross-sections of nanotubes was done by DR. AURÉLIEN MASSEBOEUF.

FIB fabrication of cross-section nanotubes is a complex, multi-step process that requires a precise and comprehensive approach. We worked with CoNiB nanotubes dispersed on a Silicon Dioxide (SiO_2) substrate. The first stage of the fabrication procedure is dispersing the selected CoNiB nanotubes onto a SiO_2 substrate. The second stage is depositing a protective layer of metal, such as platinum, on the sample using a gas injection system integrated within the FIB column. This layer protects the upper section of the nanotubes from the ion beam during the milling process, preventing damage and preserving the nanotube's original structure. The third stage is milling the sample

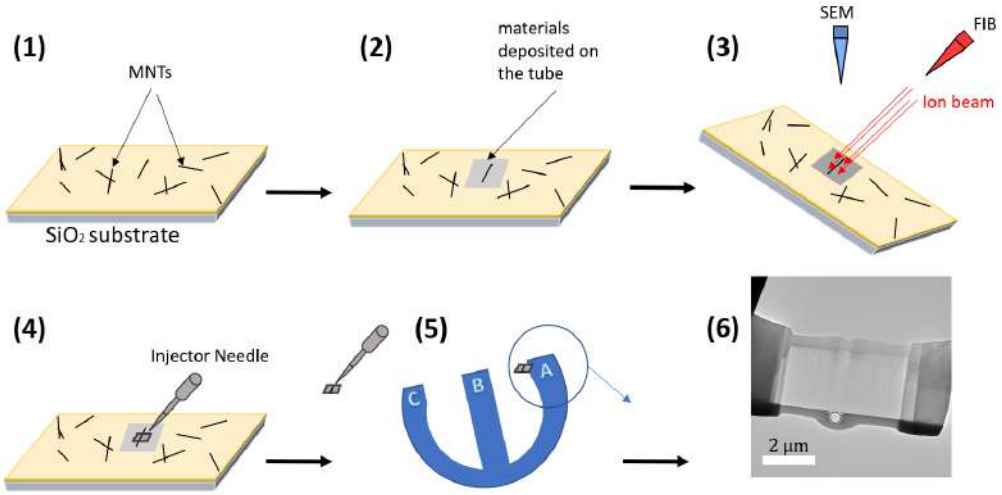

Figure 3.7: The figure illustrates the step-by-step fabrication process of cross-section nanotubes using Focused Ion Beam (FIB) technology. The process involves dispersing CoNiB nanotubes onto a SiO2 substrate, depositing a protective layer, and performing precise milling using a focused ion beam to create a cross-section of the nanotube. The final result is a highly accurate and uniform structure suitable for various nanotechnology applications.

with a finely focused ion beam composed of gallium ions to create a cross-section of the nanotube. The ion beam is locally focused, with a spot size of a few tens of nanometers. The milling process has two steps: rough milling and fine milling. In the rough milling step, a high-energy ion beam quickly removes the bulk of the material. In the fine milling step, the ion beam's energy is reduced to enhance the precision of the milling and minimize the damage, especially at the near-surface region of the sample. The nanotubes resulting from this process have uniform diameters, typically ranging from 100 to 500 nanometers. The thickness of the resulting TEM lamella is typically ranging from 80 to 100 nanometers. FIB fabrication of cross-sectional nanotubes is a powerful technique that enables us to extract the precise nanotube thickness and study the cross-section view of the nanotube. For more information about the results, see chapter 4.

Chapter 4

Structural and chemical analysis of nanotubes

This chapter emphasizes the necessity of comprehending the thickness and composition of CoNiB magnetic nanotubes for a thorough understanding of their magnetic properties. The nanotube thickness significantly impacts its magnetic behaviours, making accurate measurement critical. The chapter defines the thickness cross-section function and reviews existing TEM microscopy methods for measuring the thickness. It includes chemical characterisation through EDX and EELS to identify material density as it affects the thickness calculation. The advantages and disadvantages of each method are discussed, and the calculated thickness is used to estimate composition, including the amount of boron. The chapter also provides a theoretical estimation of the mean inner potential of polycrystalline material.

4.1 Introduction

Accurately quantifying the thickness is challenging but essential for extracting quantitative physical values, such as magnetic induction from an integrated phase shift in electron holography. Magnetic CoNiB NTs are a perfect example of nanostructures whose magnetic properties can be dramatically changed by changing their thickness and composition. Cylindrical NTs have important parameters such as internal and external diameters and a large aspect ratio. The wall thickness of these tubes significantly influences their ground state and magnetisation reversal mechanism [35, 36, 111]. Additionally, the thickness-dependent magnetic anisotropy of NTs may lead to azimuthal curling of magnetisation for certain material compositions, which is induced by curvature-related magnetoelastic effects [9, 71]. These NTs offer valuable opportunities for exploring new physics in 3D objects due to their curvature or specific topology [9, 12]. Their low stray field makes them highly suitable for various applications, including the proposed 3D domain-wall-based solid-state low-power-consumption memories.

Estimating the thickness of TEM specimens involves various methodologies, which depend on the type and composition of the specimen. These methods can be classified into two categories: destructive and non-destructive [112]. Destructive methods provide direct and accurate thickness measurements but render the sample unsuitable for further analysis. Moreover, such methods are time-consuming and impractical when dealing with multiple samples. Non-destructive methods, on the other hand, indirectly measure the thickness without causing significant damage to the

sample. They are typically self-contained and do not require further preparation steps. Using non-destructive methods requires less time and effort, making them the ideal choice for studying numerous samples and performing exhaustive analyses of individual nano-objects. Indirect measurements of specimen thickness require careful analysis to obtain a quantitative value.

This study aimed to evaluate the strengths and limitations of non-destructive methods for determining the thickness and composition of CoNiB NTs, using them as a prototypical sample. Two samples with different diameters and thicknesses were analyzed. The exact nanotube thickness was measured using TEM cross-sectioning with FIB fabrication as a reference measurement (a destructive method), while all other methods were non-destructive and could be applied alongside other analyses. The TEM image-contrast method, based on the Rutherford approximation, determined the thickness by measuring the amount of absorbed intensity through the specimen [113–118]. The log-ratio method, using EELS and is applied in energy-filtering TEM mode (EFTEM), estimated the thickness by calculating the inelastic mean-free path (IMFP) λ_i [119–121]. Finally, electron holography was used to determine the amplitude and mean-inner potential (MIP) images, providing thickness determination by energy-filtered amplitude coupled with λ_i estimation [91, 122] and electrostatic phase shift associated with MIP (V_0) estimation [90, 91]. Before starting thickness measurements, the chemical characterization using EDX and EELS was performed to understand the chemistry at play, as the thickness calculation largely depends on the density (and thus chemical composition).

Other methods for thickness determination exist, but they proved unsuitable for our specific study. Techniques such as Convergent-Beam Electron Diffraction (CBED) are frequently used to measure the thickness of crystalline alloys with a 2 % measurement accuracy [123, 124]. This method involves linear fitting of several fringes across the CBED disc, coupled with dynamical simulation to extract thickness. However, this method is not effective for polycrystalline specimens, such as the studied ferromagnetic nanotubes. EDX is another widely used technique to measure thin film thickness and provides information on composition. There are two established EDX-based methods for composition quantification: the Cliff-Lorimer [125], and ζ-factor [126] methods. However, our attempt to determine the tube's thickness using EDX proved challenging due to the low absorption of the CoNiB NTs, resulting in very low counts. This low absorption, which measures less than 10 %, may lead to inaccuracies in the quantification of results and lower the chances of achieving a significant thickness calculation. These results underscore the importance of careful consideration and appropriate selection of measurement techniques to accurately determine the thickness of specimens with extremely low absorption coefficients.

Although TEM is widely used for the structural characterisation of nano-objects, there is still room for improvement and comparison of different non-destructive methods for calculating their thickness and composition. This research gap motivates the current work, which seeks to explore and compare various non-destructive methods for determining the thickness and composition of CoNiB nanotubes.

4.2 TEM-Based Methods for Assessing Thickness

This study delves into the theoretical foundation of each method utilized. To prepare TEM samples, the FIB technique was used to create lamellae of cross-sectioning (CS) NTs dispersed on SiO substrates. The substrate surface was shielded with metallic e-beam-induced deposition (For more details on the process, review section 3.3.2). The TEM-FIB method was used as a reference

technique to measure the thickness and the chemistry distribution. Non-destructive methods were employed to determine the NT thickness, and their underlying assumptions and indirect calculations are detailed in the following sections. Finally, we established the mathematical expression for the cross-section thickness function of cylindrical nanotubes.

4.2.1 The image-contrast method by TEM

The TEM image-contrast method is based on the assertion that the transmission of an electron beam through a specimen is proportional to the product of the specimen's absorption cross-section σ, density ρ, and path length L through the specimen. This relationship, following Beer's law, can be expressed as:

$$I_{tr} = I_0 \cdot \exp(-\rho \cdot \sigma \cdot L) \tag{4.1}$$

The equation for the image contrast, denoted by $C = \ln(I_{tr}/I_0)$, is derived from the ratio of transmitted intensity through the specimen, I_{tr}, to the incident intensity of the electron beam passing through the vacuum, denoted by I_0. Two formulas can be used to express this relationship. The first formula describes the connection between C and the mass-thickness of the specimen, ρt, as well as the atomic scattering cross-sections. Lenz [113] first employed this relationship in 1954, which has since been utilized by other researchers [114–116]. The second formula, developed by Pozsgai [117, 118], is an empirical expression that relates C to the mass-thickness of the specimen, ρt, the effective atomic number, Z, and the atomic weight number, A, of a single-element specimen. In Rutherford's approximation, the electron scattering is represented by its absorption cross-section, σ, which is proportional to Z^2 at high accelerating voltages. The following equation gives Pozsgai's definition of image contrast:

$$C = \log_{10}(I_0/I_{tr}) = \left(\frac{k \cdot Z^x \cdot \log_{10}(e)}{A}\right) \cdot \rho \cdot t \tag{4.2}$$

The proportionality factor, denoted as K, is given by the equation $K = k \cdot \log_{10}(e) \cdot 10^{-4}$, where x is the exponent of the atomic number Z, and it equals 1.96 at an accelerating voltage of 200 kV [117]. The factor K is material-independent and can be calculated by measuring the thickness of some known elements, allowing for determining the mass thickness of any specimen material [117, 118]. However, the accuracy of the image contrast in the two relations [113, 117] may be limited in certain samples and conditions due to multiple scattering at larger angles, which depends on the specimen thickness and content and electron energy [127, 128]. More details about the limitations will be given in the discussion part.

4.2.2 The Log-ratio method by EELS

EELS in the EFTEM mode is a widely used technique for estimating the thickness of both amorphous and crystalline specimens. This technique involves analysing the ratio of elastic electrons (zero-loss peak - ZLP) to the whole electron spectra, which include both elastic and inelastic electrons. By analysing this ratio, it is possible to determine the thickness of the sample. The technique is particularly useful for samples that are difficult to analyze using other methods, such as those with complex structures or interfaces. It is also relatively simple and can be performed quickly, making it a popular choice for thickness measurements in many research applications.

The Kramers-Kronig sum-rule and log-ratio methods are the two methods employed to estimate the thickness in this technique, based on the mathematical relations between the real and imaginary parts of the complex dielectric function and the statistical properties of the energy loss spectra, respectively. However, both of these methods only apply within the tube's scattering area, meaning for collection angles below 20 mrad [128, 129]. While both techniques have advantages and drawbacks, the log ratio method is generally considered the easiest to use, requiring minimal assumptions during the data treatment. The log-ratio method is based on the Poissonian nature of inelastic scattering in the TEM, which refers to the statistical distribution of the energy loss electrons suffer as they pass through a material. Inelastic scattering occurs when an electron interacts with the atoms in a material and loses some of its energy. The basic formula for this method is represented in the equation below, which is relatively simple to use:

$$\frac{\mathrm{t}}{\lambda_{\mathrm{i}}} = \log_{10}\left(\frac{\mathrm{I_0}}{\mathrm{I_{tot}}}\right) \tag{4.3}$$

where I_0 represents the total intensity of an image, including elastic electrons, while I_{tot} represents the intensity of the same image for both elastic and inelastic electrons. λ_i is the inelastic mean free path (MFP). However, the drawback of this technique is that it only provides relative thickness measurements, not absolute ones. To obtain absolute thickness measurements, we must know the material's inelastic MFP λ_i. Two models for computing it are the Malis [120] and Iakoubovskii [121] models. The Malis model is a widely used empirical model that provides accurate inelastic MFP values for many materials. It is based on the work of Malis and coworkers [120], who developed a theoretical framework for calculating the inelastic MFP of materials based on their electronic structure and density ρ. On the other hand, the Iakoubovskii model is a recent development based on the scattering cross-section of electrons in materials. This model takes into account the energy loss distribution of electrons, as well as the angular distribution of the scattered electrons, such as the electron probe's convergence angle α and the collection semi-angle β to determine the value of λ_{i}.

Depending on the material and the needed accuracy, you can choose between the Iakoubovskii and the Malis models for calculating the inelastic MFP. Egerton [129] conducted a comparison of the Malis and Iakoubovskii models for calculating the inelastic MFP in EELS. Although the comparison results were inconclusive, they suggested that the Iakoubovskii model might be more accurate. Hence, we decided to employ the Iakoubovskii model in our study. The formula for calculating the inelastic MFP using the Iakoubovskii model is as follows [121]:

$$\begin{aligned} \frac{1}{\lambda_{\mathrm{i}}} &= \frac{11\rho^{0.3}}{200FE_0}\ln\left(\frac{\alpha^2+\beta^2+2\theta_{\mathrm{E}}^2+\left|\alpha^2-\beta^2\right|}{\alpha^2+\beta^2+2\theta_{\mathrm{C}}^2+\left|\alpha^2-\beta^2\right|}\times\frac{\theta_{\mathrm{C}}^2}{\theta_{\mathrm{E}}^2}\right), \\ F &= \frac{1+E_0/E_m}{\left(1+E_0/511\right)^2}, \theta_{\mathrm{E}} = \frac{5.5\rho^{0.3}}{FE_0}, \theta_{\mathrm{C}} = 20\,\mathrm{mrad} \end{aligned} \tag{4.4}$$

where F is a relativistic factor that depends on the energy of electrons. $\mathrm{E_0}$ is the energy of electrons in kV, and $\mathrm{E_m}$ is the average energy loss ($\mathrm{E_m} = 7.6\cdot Z^{0.36}\mathrm{eV}$). α and β are the convergence angle and the collection semi-angle in mrad respectively. θ_{E} is the characteristic angle of inelastic scattering corresponding to an energy loss. The saturation factor, denoted by θ_{C}, is a constant value of 20 mrad. The rationale behind this parameter has been explained in detail by Egerton [129] concerning the critical wavevector of plasmon scattering. The value of θ_{C} depends on the material's

Fermi surface structure, which can make it complex. However, this dependence is relatively weak in thickness measurements, and experimental errors tend to overshadow it. Therefore, θ_C can be considered constant for practical purposes [121, 129]. To determine the thickness of the alloy, we calculated the value of λ_i using the method described in [121].
In summary, while there are multiple techniques for measuring thickness using EELS, the log-ratio method is often considered the easiest to use. However, to obtain absolute thickness measurements, it is necessary to know the inelastic MFP of the material, which can be computed using either the Malis or Iakoubovskii model.

4.2.3 Electron Holography

Off-axis electron holography as a technique within Transmission Electron Microscopy (TEM) provides high resolution and electromagnetic sensitivity by analyzing the phase and amplitude of the electron wave after it interacts with the specimen, as described in [130]. It's important to note that this technique has been extensively used throughout my PhD research due to its versatility and ability to provide valuable insights into the specimen. Notably, it also offers the capability to measure the thickness of the studied materials, providing additional depth to our understanding of the specimen's structural properties.
In the TEM, the electron wave passes through a sample, resulting in the total intensity distribution denoted as I_{total}. This distribution is a sum of the intensities of both unscattered and scattered electrons, with the scattered electrons further divided into elastic $I_{elastic}$ and inelastic $I_{inelastic}$ electron intensities. Therefore, the total intensity can be expressed as follows:

$$I_{total} = I_{unscattered} + I_{elastic} + I_{inelastic} \tag{4.5}$$

In the sample transmission process, any electrons that have not undergone substantial energy loss are retained within the zero-loss peak (ZLP). The intensity of this ZLP is referred to as I_{zero}, and it can be defined as follows:

$$I_{zero} = I_{unscattered} + I_{elastic} = I_{total} - I_{inelastic} \tag{4.6}$$

Additionally, by utilising the relationship of EELS between the total incident intensity and the inelastic electrons intensity $I_{inelastic} = I_{total}[1 - e^{-t/\lambda_i}]$ and by adding the definition of I_{zero}, we will get the same relation written in equation 4.3.
A straightforward and practical approach called holography filtering is utilized to determine the ratio t/λ_i from the amplitude image generated from off-axis electron holograms. In this ratio, t represents the local thickness, while λ_i denotes the mean-free path for inelastic scattering of high-energy electrons. By applying this technique to samples with well-defined λ_i, the energy-filtered amplitude reconstructed from a hologram can be used to measure the thickness of the sample, t.
Although energy filtering by electron holography and the EFTEM formula for calculating thickness may appear similar, they are fundamentally different techniques. In energy filtering by electron holography, off-axis electron holography records a hologram of the electron wave exiting the sample. This hologram is then processed to extract the phase and amplitude information of the electron wave, which can be used to determine the sample's thickness. In contrast, the EFTEM formula for calculating thickness involves imaging the sample at two different electron energies. One image is captured at a lower energy level (prior to energy loss), while the other is taken at a higher energy level (post-energy loss due to inelastic scattering). The two images are then used

to calculate the inelastic scattering cross-section of the sample, which can be used to determine the sample's thickness. While both techniques involve energy filtering, their underlying principles and measurement methods are different. The choice of which technique to use may depend on the sample being analysed and the accuracy required for the measurement.

In addition, according to [90], the determination of the thickness of such samples can be carried out using electron holography in a TEM, given that the MIP of the material is known. In case the dynamical diffraction is negligible, a linear correlation exists between the phase shift generated by the sample and its thickness t relative to a reference wave travelling through a vacuum, represented by Δ_Φ. If the specimen is uniform along the axis and not influenced by external electric fields, the phase shift is directly proportional to the local thickness of the sample, as depicted in the following equation:

$$\Delta_\Phi = \mathrm{C_E} \cdot \mathrm{V_0} \cdot \mathrm{t} \tag{4.7}$$

The parameter $\mathrm{V_0}$, denoting the mean inner Coulomb potential, depends on the specimen's structural and electronic characteristics. The MIP of cobalt-rich CoNiB alloys was determined using electron holography with a known diameter of CoNiB nanowires, yielding the value of $\mathrm{V_0} = 21 \pm 1\,\mathrm{V}$, which was used in this study. Further modelling methods for determining this parameter are discussed in section 4.4.1. The interaction constant $\mathrm{C_E}$ can also be calculated based on the electron's kinetic energy and the microscope's accelerating voltage. For an accelerating voltage of 200 kV, the value of $\mathrm{C_E}$ was determined to be $7.288\,\mathrm{V^{-1}\mu m^{-1}}$.

4.2.4 Defining the integrated thickness

Determining the thickness of a cylindrical nanotube is a crucial step in studying its magnetic properties. To accurately calculate the thickness, a thickness function profile must be defined. In this section, we will introduce the thickness function cross-section profile of a cylindrical nanotube. This mathematical expression relates the phase shift of the electron wave passing through the sample to the thickness of the sample at each point across the tube. We will describe how to define the thickness function profile mathematically and discuss its importance in determining the data profiles based on the thickness function, such as the TEM profile, the MIP and amplitude profiles from electron holography, as well as the XAS, XMCD and the magnetic phase shift profiles that are used in chapter 5.

Assuming a cross-sectional view of a cylindrical nanotube centred on point O, with outer and inner radii of R and r, respectively, and a wall thickness of $t = \mathrm{R} - \mathrm{r}$, the geometry of the studied tube is illustrated in Figure 4.1. The electron beam passes through the tube along the y-axis, cutting through three distinct regions perpendicular to the tube's axis, represented by the z-axis. To simplify the model, we define the following points: $\mathrm{O}(0,0)$, $\mathrm{C}(x,0)$, $\mathrm{E}(x.y_1)$, $\mathrm{D}(x,y_2)$, $\mathrm{F}(x.-y_1)$ and $\mathrm{G}(x,-y_2)$. In this scenario, we define the function $t(x)$, representing the beam's path travelling through the nanotube. Figure 4.1 shows that the beam passes through three domains or interfaces for each x position along the nanotube's x-axis. The function $t(x)$ changes with variations in the x-axis, yielding a unique $t(x)$ value for each x position, while the y varies between $-y_2$ and y_2. Therefore the t(x) can be written as follows:

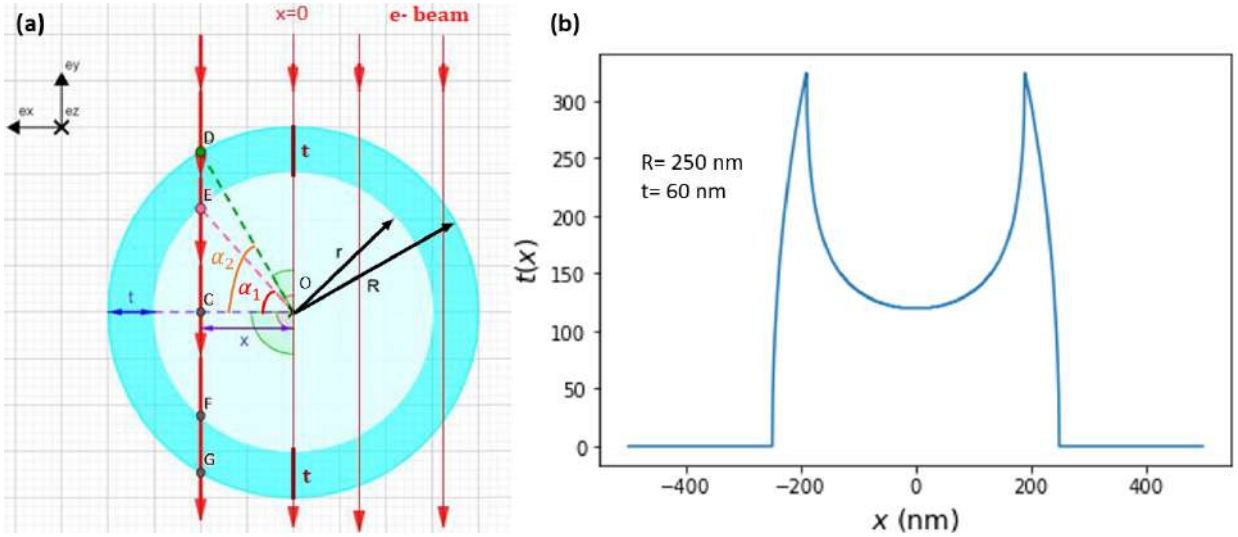

Figure 4.1: (a) A schematic illustration of the cylindrical nanotube, with the electron beam passing through three distinct regions at various positions along the y-axis. R and r are the outer and inner radii, respectively. $t = \mathrm{R} - \mathrm{r}$ is the tube thickness. (b) A plot of the thickness profile cross-section function $t(x)$ for a cylindrical nanotube with an outer radius $\mathrm{R} = 250\,\mathrm{nm}$ and thickness $t = 60\,\mathrm{nm}$. The function represents the variation in the thickness of the nanotube along its cross-sectional area. The plot indicates that the thickness of the nanotube is not uniform and decreases towards the edges, reaching a maximum thickness value at the tube's periphery and a value of 2t at the tube's centre ($x = 0$). The x-axis represents the distance along its cross-section, while the y-axis represents the thickness of the tube in nanometers.

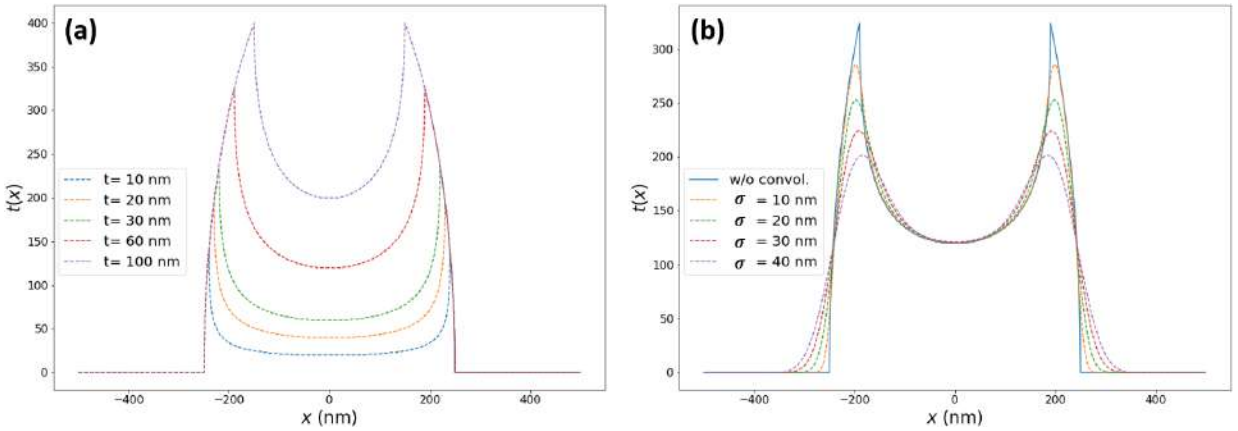

Figure 4.2: A plot of the thickness profile cross-section function $t(x)$ for a cylindrical nanotube with an outer radius of $\mathrm{R} = 250\,\mathrm{nm}$ and varying thicknesses. Subsequently, the same profile for a specific thickness of $t = 60\,\mathrm{nm}$ is depicted in (b), along with its convolution with a Gaussian distribution of different standard deviation values σ_{G}.

$$t(x) = \begin{cases} \mathrm{DE} + \mathrm{FG} = 2\mathrm{DE}, & \text{if } \mathrm{R} - t \leq |x| < \mathrm{R} \\ \mathrm{EC} + \mathrm{CF} = 2\mathrm{EC}, & \text{if } |x| < \mathrm{R} - t \\ 0, & \text{if } |x| \geq \mathrm{R} \end{cases} \tag{4.8}$$

By applying trigonometric relations, we obtain $\mathrm{DE} = \mathrm{R}\sin\alpha_2 - \mathrm{r}\sin\alpha_1$ and $\mathrm{EC} = \mathrm{r}\sin\alpha_1$, where $\alpha_1 = \arccos\left(\frac{x}{\mathrm{r}}\right)$ and $\alpha_2 = \arccos\left(\frac{x}{\mathrm{R}}\right)$. Consequently, we can rewrite $t(x)$ as follows:

$$t(x) = \begin{cases} 2\left[\mathrm{R}\sin\left(\arccos\left(\frac{x}{\mathrm{R}}\right)\right) - \mathrm{r}\sin\left(\arccos\left(\frac{x}{\mathrm{r}}\right)\right)\right], & \text{if } |x| < \mathrm{R} - t \\ 2\mathrm{r}\sin\left(\arccos\left(\frac{x}{\mathrm{r}}\right)\right), & \text{if } \mathrm{R} - t \leq |x| < \mathrm{R} \\ 0, & \text{if } |x| \geq \mathrm{R} \end{cases} \tag{4.9}$$

Figure 4.1.b shows the thickness profile cross-section function $t(x)$ for a cylindrical nanotube with specific dimensions ($\mathrm{R} = 250\,\mathrm{nm}$ and $t = 60\,\mathrm{nm}$). This function describes how the nanotube's thickness changes across its cross-section, from the centre ($x = 0$) to the edge ($x = \mathrm{R}$). As the plot reveals, the nanotube has a non-uniform thickness, with a minimum value of $2t$ at the centre and a maximum value at the edge. The x-axis and y-axis measure the distance and the thickness in nanometers, respectively. This information is essential for accurately characterising the nanotube's thickness, which is critical for understanding its magnetic properties. This thesis frequently uses this function to define the cross-sectional thickness profile in cylindrical nanotubes. Additionally, to give the function a physical meaning for describing the beam, we apply a mathematical convolution with the Gaussian distribution probability density function, which is given by:

$$f(x|\mu, \sigma_{\mathrm{G}}^2) = \frac{1}{\sigma_{\mathrm{G}}\sqrt{2\pi}} \exp\left(-\frac{(x-\mu_{\mathrm{G}})^2}{2\sigma_{\mathrm{G}}^2}\right) \tag{4.10}$$

The Gaussian distribution, defined by the mean μ_{G} and variance σ_{G}^2, depicts a bell curve centred at the mean, with the curve's breadth governed by the variance. The distribution is symmetric around the mean, with 68% of the total area within one standard deviation. Widely applied in statistics, physics, and engineering, the Gaussian distribution models probability distributions and describes beam spot sizes in optics by characterizing intensity profiles. Smoothing out experimental noise and uncertainty, the distribution can enhance data analysis, aiding in more precise information extraction. In our context, the Gaussian distribution lends a physical interpretation to the theoretical function determining the beam path through the nanotube.

4.3 Results and discussion

4.3.1 Ferromagnetic Nanotubes

In this study, CoNiB ferromagnetic NTs were considered with azimuthal curling of magnetisation caused by curvature-induced magneto-elastic anisotropy [9]. The samples were fabricated by electroless plating in ion track-etched polycarbonate membranes according to a previously published procedure [9, 131]. The template membrane was dissolved afterwards using dichloromethane to obtain isolated NTs for further characterization. In total, two NTs have been studied, NT_1 and NT_2 that have diameters of $\mathrm{d}_1 = 145\,\mathrm{nm}$ and $\mathrm{d}_2 = 470\,\mathrm{nm}$ and thicknesses t_1 and t_2, respectively. Both have a length $\mathrm{l} = 30\,\mu\mathrm{m}$, which is determined by the dimensions of the polycarbonate membrane

used as a template. The thicknesses obtained by 45 min of electroless plating have been directly measured from the CS samples prepared by the FIB-TEM method (a direct measurement). We have obtained from the FIB-TEM method: $t_1 = 21.8 \pm 0.5$ nm and $t_2 = 59.1 \pm 1.2$ nm.

Figure 4.3, adapted from [71], presents the TEM characterization of the CoNiB nanotube (NT_2). Images acquired via conventional (S)TEM imaging are shown in Figure 4.3 (a-c), demonstrating the visible nano-granular structure of the grown layer. Since transmission images of tubular structures can overlap information from the top and bottom layers in the projected image, our focus was on a broken tube, as depicted in the inset of Figure 4.3.b. This allowed high-resolution imaging of a single layer, resulting in sharp images that suggested a typical grain size of 8 ± 5 nm and a typical grain boundary size as large as 1 nm. The grain boundaries, which appear black in the HAADF contrast image (Figure 4.3.c), suggest the presence of light elements such as Boron. However, at this high magnification, we were unable to detect Boron by EDX due to its light-element nature. A higher magnification image, shown in the inset of Figure 4.3.c, revealed that the grains exhibit a finer structure, which we associated with the Pd seeds used for electroless growth. More details about the detected Pd seeds are presented in section 4.3.2. As previously discussed, we used FIB to slice the NTs and conduct a cross-sectional and thickness analysis in a TEM. Prior to final thinning, the TEM lamella had a thickness of around 80 ± 10 nm, based on our knowledge and experience with such preparations. The prepared lamella before the final thinning step is shown in Figure 4.3.d.

Some variations in the tube diameter, especially tapering towards the ends, were systematically observed after releasing the tubes from the template. As the tube shape is a direct replica of the pores in the polycarbonate membrane, it can be assumed that the diameter variations result from the ion track-etching process. In fact, tapered pore ends are commonly observed in track-etched polycarbonate, while the origins of this phenomenon are still not fully understood [132]. Possible reasons include higher-density surface layers introduced during polymer foil manufacturing or etchant-induced inhomogeneities [132, 133]. Furthermore, it can be observed that the thickness is generally larger at the openings than in the middle of the tubes. We attribute this variation to the electroless plating process: near the openings of the membrane, reactants are quickly replenished by both diffusion and convection. However, diffusion of reactants towards the middle of the pores is severely limited by the spatial confinement and high aspect ratio, resulting in slower plating speeds. The observation corroborates that the centre thickness is higher for tubes with larger diameters, as larger pores enable more solution flow and faster diffusion. The variation of the tube thickness along its length has been determined using the image-contrast method with a line profile selection at the centre of the tube, where the beam passes through two thicknesses (*i.e.*, two walls of the tube). Low-pass filtering has been used to lower the noise from the data. In addition, cross-section selections along the tube have been made (500 nm between each selection) to determine the variation of the diameter along the tube length l. At the tube extremities (5 µm on both ends), as compared to the centre, the thickness is larger, the diameter is smaller, and the variation is nearly symmetrical in both cases. However, a homogeneous shape of the tube is observed at the centre (Figure 4.4). To avoid any differences caused by the system inhomogeneity, the thickness measurements provided in this study were systematically taken at the centre of the tube.

The variation significantly influences the magnetic properties of the nanotube and the thickness calculation in the local chemical composition. Therefore, a combination of STEM-EDX and STEM-EELS has been used to characterize the tube's chemical composition, as shown in the following section.

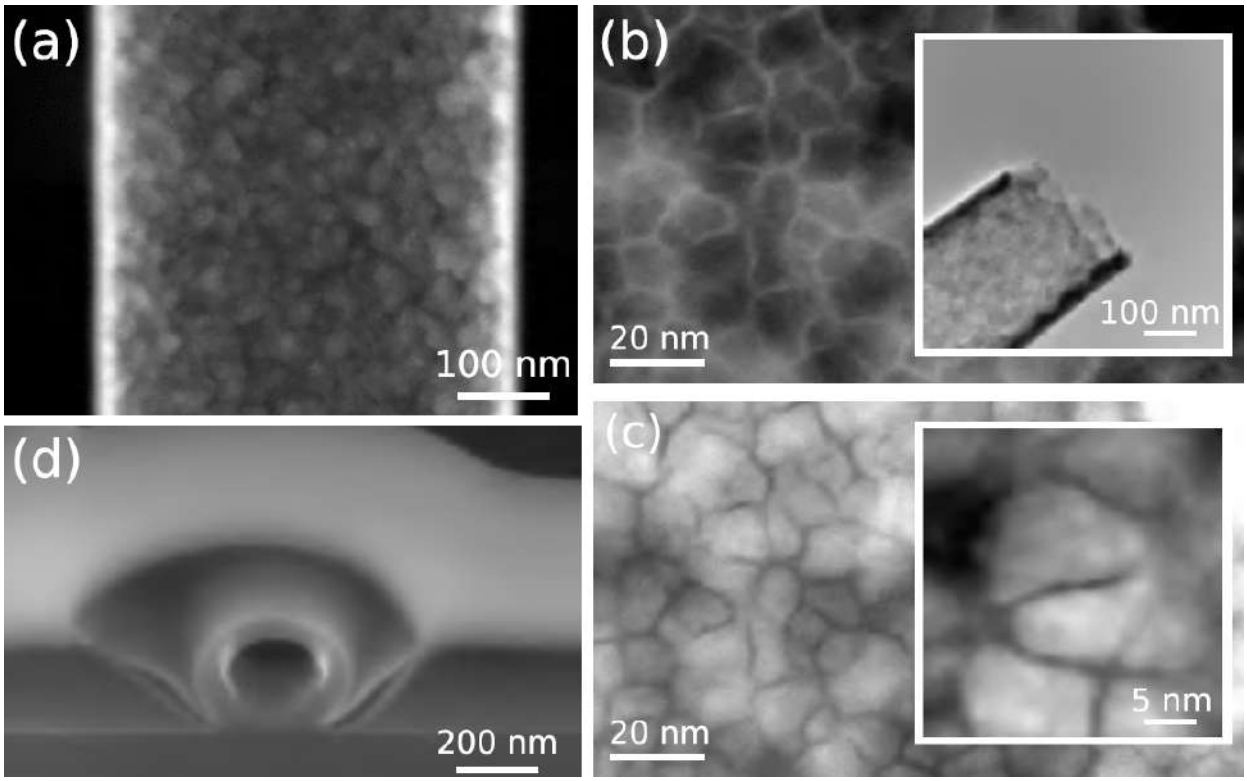

Figure 4.3: The figure presents various characterization techniques used for the nanotube (NT_2). The STEM-HAADF view in (a) reveals a granular structure of the material. Zoomed views of a one-wall-only end part in TEM bright field (b) and STEM-HAADF (c) exhibit the granular and intergranular structure. The insets show the general view of the broken tube used for this single-layer analysis and a higher magnification image in HAADF mode displaying the fine structure of the grains. The step of the FIB preparation of the (NT_2) single slice is shown in (d). This figure is adapted from [71].

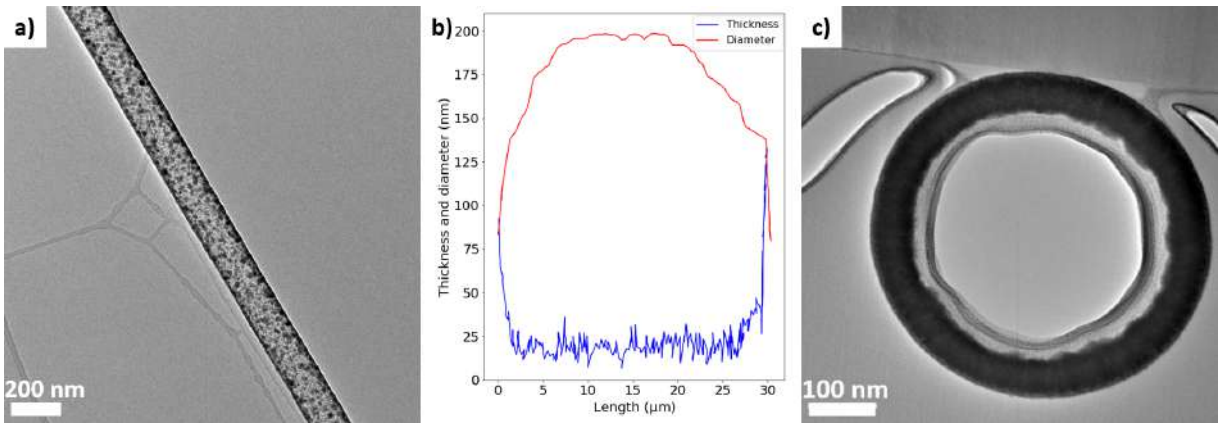

Figure 4.4: (a) Conventional TEM image of the nanotube NT_1 ($t_1 = 22\,nm$, $d_1 = 145\,nm$), the thickness has been determined at the centre of the tube axis by using the image contrast method. (b) the variation of the tube-wall thickness and the diameter of NT_1 along the tube length. (c) TEM image of the CS nanotube NT_2 ($t_2 = 60\,nm$, $d_2 = 470\,nm$) prepared by FIB.

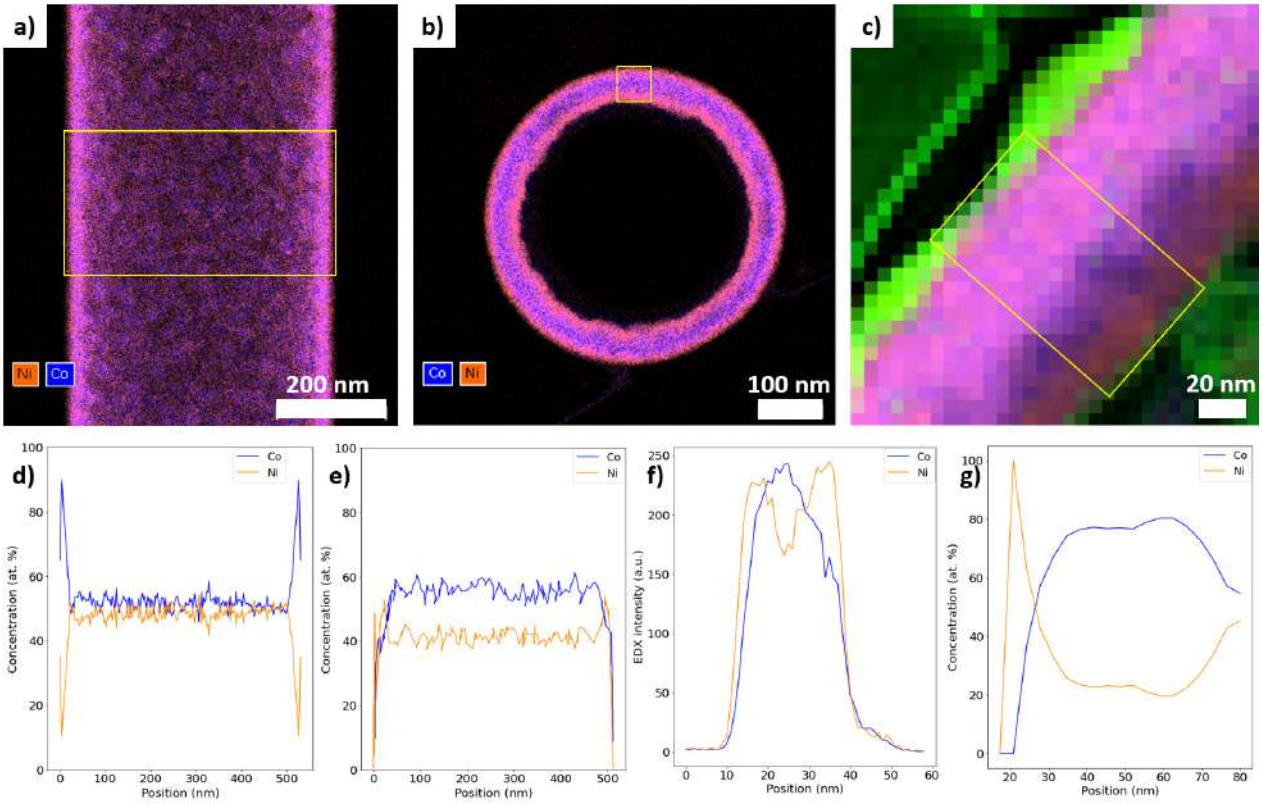

Figure 4.5: STEM-EDX colour maps of Co (blue) and Ni (orange) of the nanotube NT_2, (a) along the tube axis and (b) across the tube axis (cross-section). (c) RGB composite image (STEM-EELS) of a selected area of the CS tube NT_2. O-K edge shown in green, Co $L_{2,3}$-edges shown in blue and Ni $L_{2,3}$-edges shown in orange. (d) The composition variation in % of Co and Ni of the profile selected in (a). (e) The composition variation in % of Co and Ni averaged to the electron path profile of the CS tube in (b). (f) The EDX intensity counts of Co and Ni at the selected profile in (b). (g) The composition variation in % at the selected profile in (c). Ni prefers to segregate on both sides of the CoNi alloy.

4.3.2 Chemical analysis by STEM-EDX and STEM-EELS

Recognizing the role that composition plays in influencing the evaluation of the thickness and magnetic properties of our subject, we turned to EDX. This powerful analytical tool is essential for examining the elemental composition of materials. In the context of our study, we applied EDX in two orientations to analyze the CoNiB nanotubes: longitudinally along the tube and on the cross-section.

The results of the longitudinal analysis showed a flat composition variation along the diameter of the tube, which would suggest that the composition is uniform in the tube (Figure 4.5.a and d). It indicates $Ni_{40}Co_{60}$ of composition instead of $Ni_{30}Co_{70}$ that was expected from the electroless plating deposition parameters. However, the cross-sectional analysis showed a substantial variation of the relative EDX intensities across the tube wall, indicating that the composition is not homogeneous. The measurement shows that nickel (Ni) tends to segregate toward the tube's inner and outer surfaces (Figure 4.5.b and f). To reconcile these seemingly contradictory results, an artificial spectra projection was performed along the direction of the electron beam to recreate the condi-

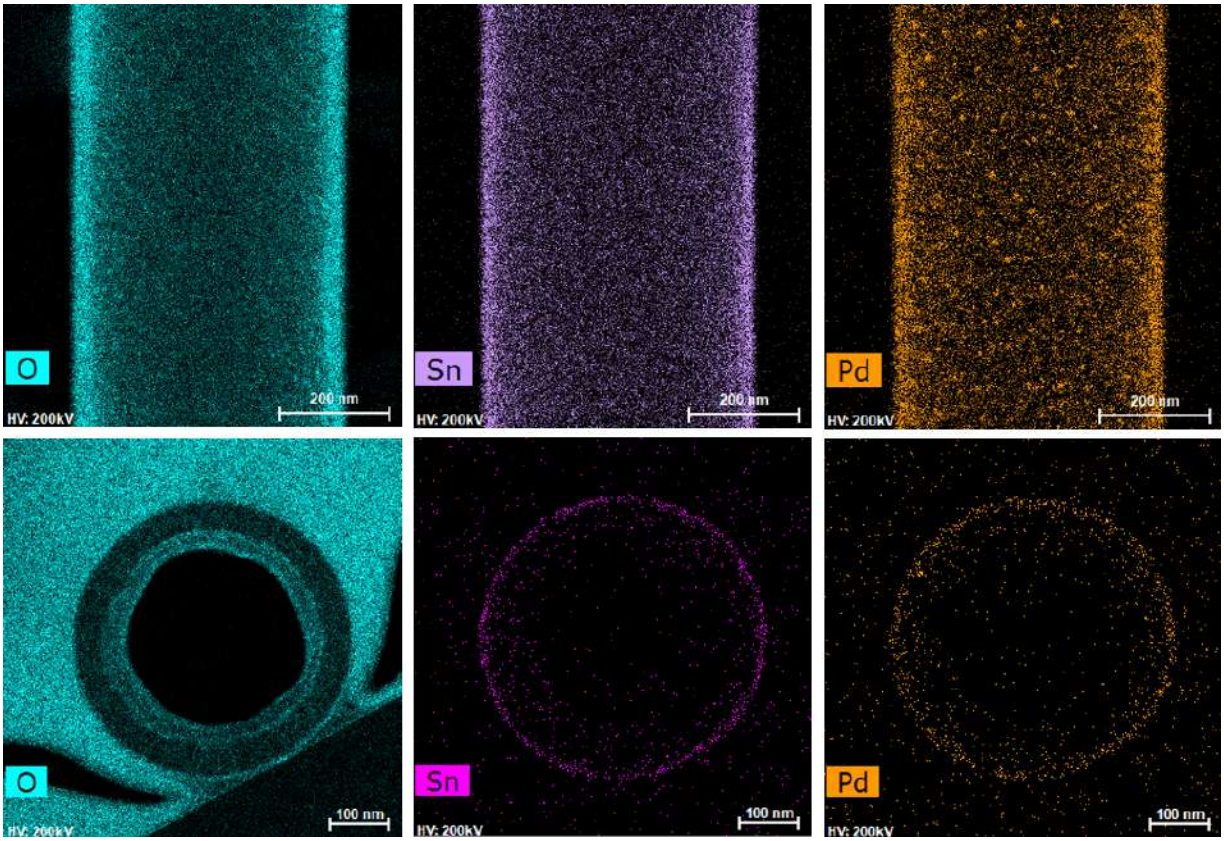

Figure 4.6: STEM-EDX colour maps of O (cyan), Sn (pink) and Pd (orange) of the nanotube NT_2, both along the tube axis and across the tube axis (cross-section).

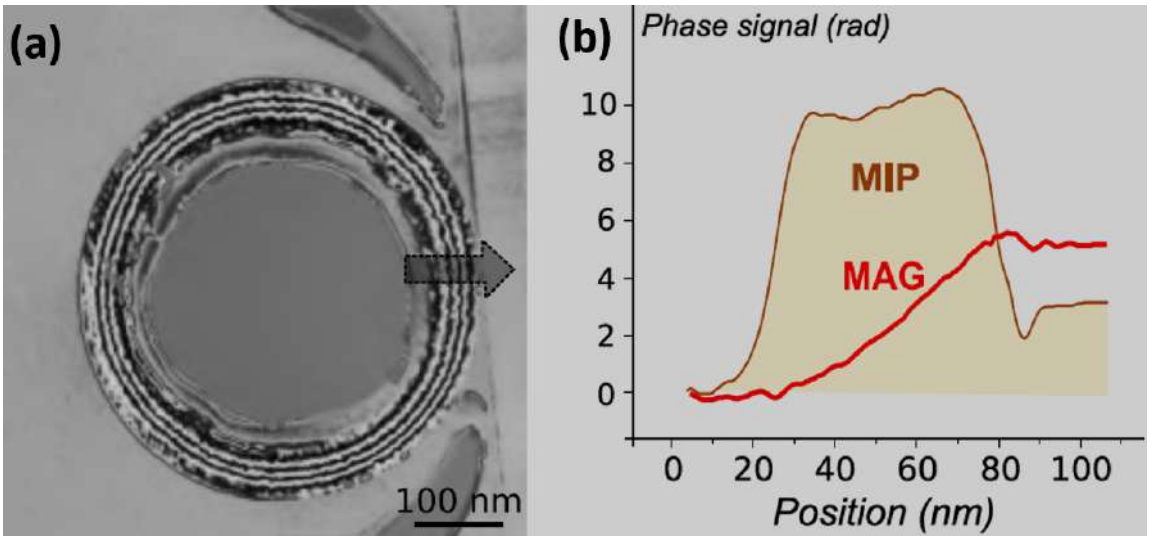

Figure 4.7: The electron holography output in (a) displays MIP $\times \cos 5 \cdot$MAG, an analysis based on observations made in Figure 3.4 from the previous chapter. The phase shift profiles for the MIP (brown) and MAG (red) components are shown in (b). This figure is adapted from [71].

tions met with the longitudinal analysis. This projection showed a flat composition (Figure 4.5.e), which confirms that the alloy appears homogeneous when viewed longitudinally, but in fact, it has a non-uniform distribution of Ni and Co.

One expectation about the reason behind the Ni segregation is that in the electroless plating process used to synthesize CoNiB nanotubes, Ni ions are reduced onto a template substrate to form the desired composition of the nanotubes. During this process, Ni can segregate and concentrate in specific regions of the nanotubes. Ni is a highly reactive element that tends to form strong bonds with other elements, such as boron (B) and cobalt (Co), which are also present in the plating solution. These bonds can result in the formation of Ni-rich regions in the nanotubes, which can have different properties than regions with lower Ni content. The degree of segregation can be influenced by various factors, such as the plating conditions, the composition of the plating solution, and the template used to synthesise the nanotubes.

This segregation can significantly affect their magnetic properties, as regions with high Ni content can have different magnetic behaviour than those with low Ni content. For example, the magnetic moment of the nanotubes can be influenced by the degree of Ni segregation, as the magnetic properties of Co and Ni are different. We used electron holography to investigate whether there is a magnetic dependence. This allowed us to separate the reconstructed phase's electrostatic (Mean inner potential - MIP) and magnetostatic (MAG) components. Figure 4.7.d exhibits the MIP and MAG phase profiles. The MAG cosine phase isolines, representing the magnetic induction flux lines, are illustrated in Figure 4.7.c. By estimating the slope of the MAG phase profile to be $0.11\,\mathrm{rad}\cdot\mathrm{nm}^{-1}$, we were able to approximate the local magnetisation to be $\mu_0 M_S = 0.9\,\mathrm{T}$, by considering a slice thickness of 80 nm. One noteworthy observation is that the MAG profile indicates a drop in magnetisation near the inner surface. However, this may be due to a local reduction in slice thickness rather than a change in composition. This phenomenon was not uniformly observed across profiles extracted from various slice regions. Furthermore, it is crucial to recognize that the flux-closure state observed in the slice may not accurately represent the ground state of a complete tube. The short aspect ratio of the resulting tube promotes azimuthal magnetisation, resulting in a

ring-like shape in this case.
It is essential to note that the material's outer surface exhibits more visible oxidation than the inner surface. However, such analysis becomes insignificant since the FIB slicing capping layer consists of SiO_x. Small quantities of Sn and Pd seeds are observed on the tube's exterior, resulting from deposition (Figure 4.6). Acquiring accurate and reliable results with EDX is often tricky for boron, a light element, due to the extremely low detection counts. Nevertheless, 20% boron content was determined from X-ray photoelectron spectroscopy (XPS) results on the provided tubes [71]. Concurrently, electron energy loss spectroscopy (EELS) was conducted to examine such a slice of the cross-section tube (Figure 4.5.c and g), revealing a compositional shift from $Ni_{20}Co_{80}$ on the exterior surface to $Ni_{50}Co_{50}$ on the interior surface, with a plateau in the middle showing a $Ni_{40}Co_{60}$ composition. The absence of oxidation inside the nanotube is also verified in this experiment. Although no significant impact on magnetic properties is observed, further investigation into these compositional differences could be conducted. Based on the chemical findings and by estimating 20% boron content, the sample compositions were determined to be: 48%, 32%, and 20% of Co, Ni, and B, respectively. These atomic fractions for this alloy were subsequently used to calculate the alloy density and tube thickness.
In this study, we estimate an average density of polycrystalline CoNiB nanotubes, homogeneous along the tube axis despite inhomogeneities across the tube wall. This approximation is based on the atomic fractions of B, Ni, and Co, which are first converted into mass fractions using their respective atomic weights. Subsequently, an estimation of the volume fractions is achieved under the assumption of an ideal mixture, whereby the mass of each element is divided by its density and normalized to sum to 1.
Applying these volume and mass fractions to the formula $\rho = \frac{\sum_i (m_i \cdot V_i)}{V}$, where m_i and V_i denote the mass and volume fractions of the i-th constituent element in the alloy, we estimated the average density of our polycrystalline CoNiB nanotubes to be $7.90 \pm 0.5\,\mathrm{g/cm^3}$ approximately. A detailed outline of this calculation procedure is provided in Appendix A of this thesis.
While this method offers a practical approximation, a more accurate assessment might require the use of advanced techniques such as computational modelling or high-resolution imaging, which can account for potential variations within the nanotube wall and non-ideal interactions between constituent elements. Estimating the density of polycrystalline alloys like CoNiB is inherently complex due to factors such as atomic interactions and structural characteristics. The conventional approach assumes ideal mixing and leverages the average atomic volumes of constituent elements, but in practice, alloy densities can deviate from these idealized calculations. While these estimations are informative for preliminary investigations, a more nuanced analysis ideally requires the density of such alloys to be determined experimentally or through advanced computational methods. However, in our study, we did not employ these advanced computational methods. Therefore, while our estimations provide valuable insights, they are not exhaustive and suggest the need for further investigation.

4.3.3 Thickness measurement and discussions

Various methods are presented and analyzed to determine the thicknesses t_1 and t_2 of the CoNiB nanotubes NT_1 and NT_2 by TEM. All the results of the thickness calculation are represented in table 4.1. The errors have been calculated using the error propagation formula based on five measurements of each method performed and their associated errors.

The FIB-TEM method enables direct, accurate, and precise determination of nanotube thickness by preparing cross-sectioned (CS) tubes with FIB and imaging them with a bright-field TEM at 200 kV (Figure 4.4.c). The outer black layer represents the ferromagnetic material, while the inner layer shows signs of fabrication-related carbon contamination. Despite this, the overall nanotube structure remains intact, demonstrating the effectiveness of using FIB for preparing TEM samples of CS nanotubes. Direct measurements reveal that the thicknesses of nanotubes NT_1 and NT_2 are $t_1 = 21.8 \pm 0.5$ nm and $t_2 = 59.1 \pm 1.2$ nm, respectively.

Despite being time-consuming, this precision is especially beneficial when high resolution and detailed analysis are critical. However, the sample preparation process is destructive and complex. Given these considerations, FIB-TEM, while invaluable for material characterisation, should be viewed as a method of last resort for sample analysis. Ideally, it should be used in conjunction with non-destructive characterisation techniques.

A bright-field TEM image of nanotube NT_2 was captured at 200 kV (Figure 4.8.a). This image was used to determine the thickness via the TEM-image contrast method, based on the principles laid out in Pozsgai's work [117, 118]. We applied Equation 4.2 for mass-thickness contrast, as our sample resembled nanotubes in its cylindrical geometry. Our initial step was to establish the value of the proportionality factor K, for which we studied various CoNiB nanotubes with known thicknesses. We determined that $K \approx 1.75 \times 10^{-4}$.

The approximate density of the polycrystalline CoNiB nanotube, determined in a previous section, was used, which stood at $\rho = 7.90 \pm 0.5\,\mathrm{g/cm^3}$. We also computed the value of $\sum_i \frac{C_i \cdot Z_i^2}{A_i}$, where i represents a single element of the alloy (Co, Ni, or B). Here, C_i represents the concentration quantity of element i, and Z_i and A_i are its atomic and mass numbers, respectively. A cross-section profile of the nanotube under study (Figure 4.8.b) was selected to derive the transmitted I_{tr} and incident I_0 intensities of the electron beam. From Equation 4.2, the mass-thickness contrast at the tube's centre (which comprises two thicknesses) is given by:

$$\rho \cdot t = \left(\frac{\log_{10}(I_0/I_{tr})}{2 \cdot K \cdot \sum_i \frac{C_i \cdot Z_i^2}{A_i}} \right) \tag{4.11}$$

By employing this method, we derived the thickness $t_2 = 57.3 \pm 3.3$ nm for nanotube NT_2 and $t_1 = 20.5 \pm 1.9$ nm for nanotube NT_1. The associated errors were determined by repeating the process five times. This method is effective as long as the proportionality factor K for the specimen is accurately estimated. Nevertheless, it might prove challenging to apply due to the necessity of multiple samples for K estimation and a high dependence on accurate density determination. For example, a change in consideration of Boron quantity by just 5% in the calculation can shift the calculated nanotube thickness by approximately 5 nm. A key assumption is that the contrast in a TEM image is solely due to mass thickness, an ideal situation which may not always be realised. Other factors, such as diffraction contrast and strain contrast, can also contribute to the image contrast, thereby impacting the precision of thickness estimates. Moreover, the quality of the TEM images is crucial to the effectiveness of this method. Factors like focus, astigmatism, image drift, or other aberrations can notably affect the image contrast, consequently leading to inaccuracies in thickness determination. In addition, electron-beam-induced carbon contamination can affect the reliability and accuracy of the thickness estimation, as it can increase the specimen thickness, degrade the resolution, reduce the contrast, and hamper the spectroscopic analysis, even with the other thickness determination methods. This method also assumes the TEM operates under

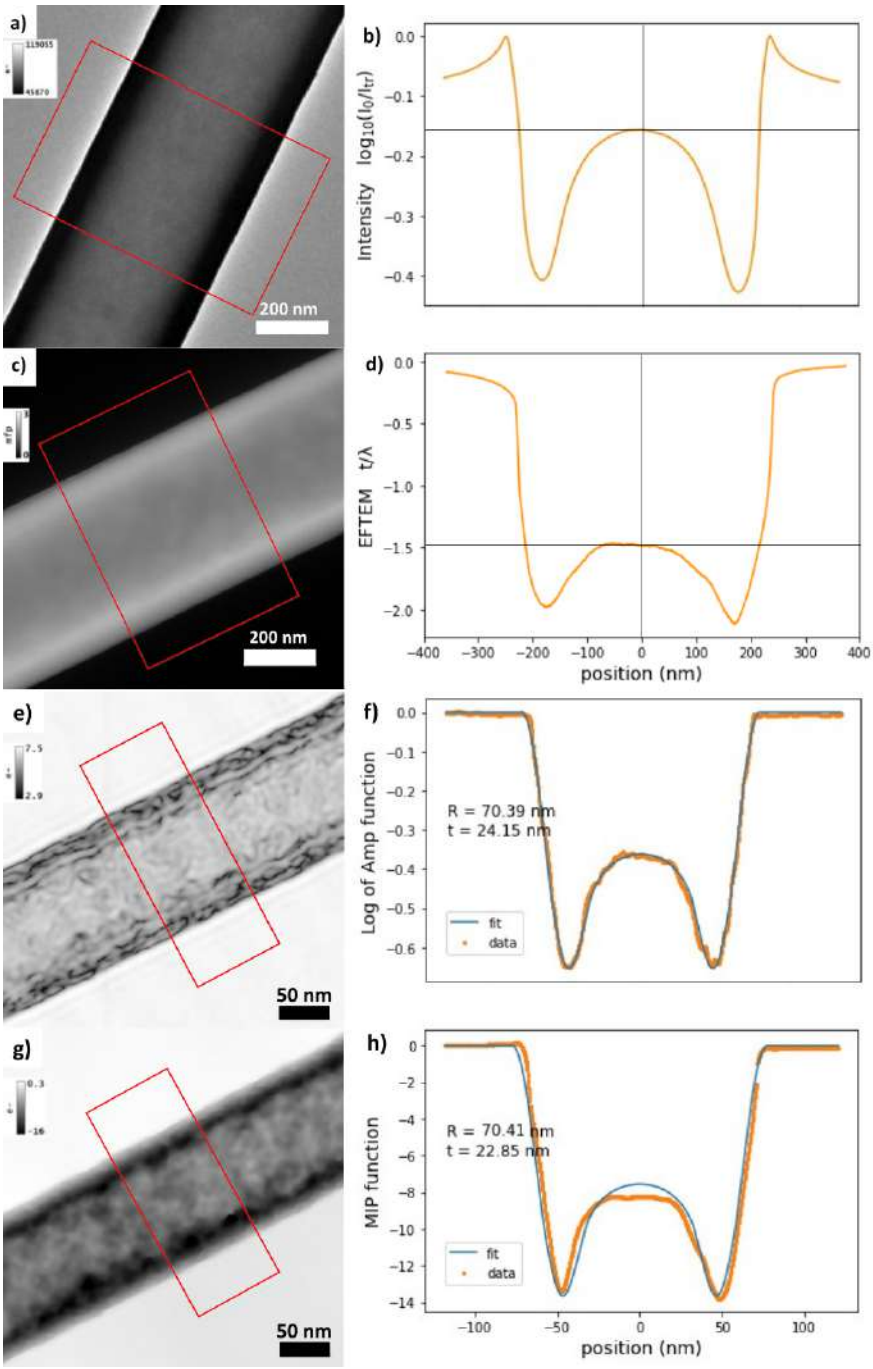

Figure 4.8: (a) TEM image of the nanotube NT_2, with a square profile ($500\,nm \times 750\,nm$) across the tube. (b) the corresponding profile of the selection that represents the transmitted intensity across the tube position. The intensity at the centre of the tube is associated with two values of the thickness ($2t_2$). (c) the EELS thickness map image (EFTEM) of the nanotube NT_2, with a square profile ($500\,nm \times 750\,nm$) across the tube. (d) the associated profile shows t_2/λ versus the position across the tube. The value of $\log_{10}(I_0/I_{tot})$ corresponds to $2t_2/\lambda$ at the tube's centre, where there are two thicknesses. (e-g) the logarithmic of the amplitude and the MIP images, respectively, obtained by electron holography of the nanotube NT_1 with square cross-section ($100\,nm \times 250\,nm$) profiles across the tube. (f-h) the corresponding amplitude and MIP profiles across the tube with the theoretical fittings. R is the tube's outer radius, and t is the thickness output from the fittings.

the "weak phase object" regime, an assumption which is not held for thicker or more complex samples. Further, it presumes that the nanotube maintains a perfectly cylindrical shape, which, in real-world scenarios, may not always be the case. Deviations from the ideal cylindrical form can introduce errors in thickness determination. In the context of an alloy such as CoNiB, the elemental composition plays a significant role in the accuracy of the calculation. Any variation in the composition across the nanotube can influence the image contrast and, therefore, affect the thickness measurement. Despite these limitations and challenges, this method provides a valuable non-destructive approach to estimating nanotube thickness.

EFTEM has been performed on studied samples at 200 kV. Two images represent the elastic and inelastic intensities, produced using a Gatan Imaging Filter (GIF) that allows the electrons to be selected according to their energy. The acquisition should be made with a minimal slit varying from 5 to 15 eV, depending on the stability and the precision of the GIF. By considering $\beta = 27.5$ mrad, which is calculated from the diffraction pattern of a known element such as Si, λ is therefore estimated to be 120 nm for CoNiB alloy based on [121] calculation. Figure 4.8.c represents the EELS thickness-map image of the studied nanotube NT_2. A square profile selection has been used to calculate the value of $\log_{10}(I_0/I_{tot})$ that corresponds to the ratio of $2t/\lambda$ at the centre of the tube (figure 4.8.d). The thickness has been calculated by using equation 4.3, and we have obtained $t_1 = 23.3 \pm 2.9$ nm and $t_2 = 64.5 \pm 4.5$ nm for nanotube NT_1 and NT_2 respectively.

Notably, neither the estimation of the alloy's density nor the assessment of the quantity of boron in the alloy plays a significant role in this method. However, a small change in the semi-collection angle β will change the estimation of the Inelastic Mean Free Path (IMFP), λ_i, as well as the determination of the thickness. There is a strong dependency when the value of β is below 20 mrad, and a weak one when the value is higher. To illustrate, if β changes by 10 mrad (when $\beta \leq 20$ mrad), this adjustment alters the calculated tube thickness by more than 10 nm. However, if β changes by 20 mrad (when $\beta \geq 30$ mrad), the calculated thickness is affected by around 4 nm. These results are compatible with the studies of [120, 121, 134]. For alloys like CoNiB, the chemical composition can greatly influence the estimation of λ_i. In our experiment, we worked with a constraint where the value of β is 27.5 mrad. In this context, the dependency falls into the weaker range, making the effect of changes in β less significant on the calculated tube thickness. The CoNiB nanotubes might not have a uniform composition throughout, which can affect the accuracy of the thickness determination. The EFTEM method works well as long as the IMFP λ_i is estimated, especially with thinner samples (20-150 nm thick). However, in thick specimens, there is an issue with the multiple scattering, resulting in low energy counts detected in the camera. A major difficulty could arise when analyzing samples of unknown composition. The EELS method is quicker and more comfortable, with accuracy depending on the determination of λ and the density ρ of the alloy [119–121, 135].

Off-axis electron holography was performed on the studied nanotubes. The holograms of the investigated nanotubes were captured on a 4096×4096 pixels camera using an FEI Titan Ultimate (FEI Company) at 200 kV accelerating voltage. The biprism voltage was set to 150 V. In order to separate the electrostatic and the magnetic phase contrasts, two holograms were recorded with opposite applied magnetic fields parallel to the tube axis to axially magnetize the tube. The addition of the reconstructed holograms from both magnetic states yields the electrostatic phase image. The amplitude image, meanwhile, can be determined from the hologram after reconstruction. The logarithmic amplitude and the MIP images are shown in figure 4.8.e and g. Theoretical definitions of the amplitude and the MIP cross-section profiles have been employed to fit the experimental data based on the thickness function $t(x)$. This optimized fitting technique can be utilized to extract the

value of the thickness for known experimental parameters. The fittings of the profiles are shown in figure 4.8.f and h.

One key aspect of this method is post-processing. Procedures like noise reduction and phase unwrapping play a substantial role in determining the quality of the reconstructed images and, subsequently, the accuracy of the thickness measurements. Further, appropriate imaging conditions are essential for reliable results. The specimen should be thin enough to be electron transparent and well isolated from the supporting film to minimize interference. When compared with other techniques, electron holography holds distinct advantages and challenges. This method works optimally for samples with a thickness less than 50 nm. For thicker samples, absorption becomes very high, making the application of electron holography methods difficult. Additionally, electron holography methods can only be used when experimental parameters, such as the IMFP λ_i for thickness calculation from the amplitude image and the internal potential V_0 of the alloys for calculation using the MIP method, are known.

The overall coherence between the results derived from each method demonstrates their robustness and reliability. Specifically, the range for the thickness of NT_1 (56 - 64 nm) and NT_2 (20 - 24 nm) differs by less than 5% for both tubes. The FIB-TEM cross-sectioning technique is the most precise method for directly determining the thickness. However, it is highly sample-specific and not suitable for bulk investigations. In contrast, the TEM image contrast method is versatile and straightforward, providing reliable measurements as long as the sample's proportionality factor and density are known. Likewise, the EFTEM technique performs admirably when providing the sample's mean free path λ. However, it's essential to note that the TEM image contrast, EFTEM and electron holography methods are influenced by phase contrast resulting from microscope aberrations, which could affect data fitting. Although these effects could be rectified by incorporating the contrast transfer function in the fittings, this additional step might complicate the process for some users. The electron holography methods are advantageous in instances where phase contrast is minimal, and they provide accurate measurements for those familiar with the electron holography technique. However, the holography methods require considerable effort during the experimental stage and the image processing after the experiment. Moreover, they're only applicable to known experimental parameters such as the IMFP λ_i for the thickness calculation from the amplitude image and the internal potential V_0 of the alloys for the calculation by using the MIP method. Furthermore, these techniques are the only ones limited to the sample size, as they struggle with samples thicker than 100 nm.

Our study reviews the methods that can be applied to measure the thickness in TEM, as this is a crucial factor for understanding the magnetic properties of nanotubes. Discrepancies in thickness can significantly affect our understanding of magnetic induction and magnetisation reversal mechanisms, which are crucial for designing magnetic-based devices. The precise determination of nanotube thickness is particularly vital in the context of magnetic anisotropy and the associated azimuthal curling of magnetisation. The results of our study are a significant step towards facilitating such explorations. A key challenge in this study was the low absorption of the CoNiB NTs in TEM. We found that the chosen methods in this study can handle the problem, but there is room for improvement. Future studies could enhance the performance of these techniques for samples with extremely low absorption coefficients. Thus, our findings offer valuable insights for future research focusing on CoNiB nanotubes or similar structures.

Table 4.1: A table summarizing all the methods used to calculate the thicknesses t_1 and t_2 of the two studied nanotubes NT_1 and NT_2 respectively, and with the corresponding errors in nm.

Method	t_1 (nm)	t_2 (nm)
FIB-TEM cross-sectioning	59.1 ± 1.2	21.8 ± 0.5
TEM image contrast	57.3 ± 3.3	20.5 ± 1.9
EFTEM log-ratio	64.5 ± 4.5	23.3 ± 2.9
Amplitude Electron holography	59 ± 3.9	24.2 ± 2.8
MIP Electron holography	56 ± 5.3	22.8 ± 2.2

4.4 Determination of important parameters for a known material thickness

In the previous sections, we have shown how to determine the thickness of nanotubes in TEM using different methods. These methods require some prior knowledge of other material parameters, such as the density, the mean inner potential, and the mean free path. However, once the thickness is determined by one of the methods, such as the FIB-TEM method, these parameters can also be estimated by comparing the experimental results with the theoretical models of the other methods. In this section, we will demonstrate how to use the thickness information to extract the MIP and the density of the nanotubes. We will also discuss how these parameters can help us infer the composition of the nanotubes, such as the boron content. This shows the interdependence of the material parameters and how knowing one of them with accuracy can lead to a better understanding of the others.

4.4.1 MIP of polycrystalline samples

The MIP is an essential property of crystalline or polycrystalline materials that can be mathematically calculated using various techniques. This text will discuss the general approach to calculating MIP for materials such as CoNiB.

MIP is defined as the average electrostatic potential of the innermost electrons of a material, which is independent of the chemical composition of the material. It is a fundamental property that can provide insights into the electronic structure of a material, as well as its bonding and reactivity. MIP is typically measured using experimental techniques such as electron holography for a known thickness of the specimen. However, it can also be calculated theoretically using various models and methods.

One such theoretical approach to calculating the MIP is using Dirac-Fock calculations [136, 137]. This method, which is an extension of the Hartree-Fock technique, considers both electron correlation and relativistic effects, making it particularly useful when dealing with high-speed electrons or in scenarios involving strong electric fields. The Dirac-Fock calculations provide a method for computing x-ray scattering factors, which are key to understanding how x-ray photons interact with a material's electrons.

For materials such as CoNiB, which are polycrystalline, MIP can be calculated using various averaging techniques that consider crystal orientations' distribution or the atomic arrangement's randomness. One method for calculating the MIP of polycrystalline materials is the Monte Carlo simulation, which involves generating a large number of random crystal structures and calculating

the MIP for each structure. The average MIP is then calculated by averaging over all the simulated structures. The equation for calculating the MIP using the Monte Carlo simulation is:

$$\text{MIP} = \frac{1}{V} \iiint V(r) \cdot \rho(r)\, dr \tag{4.12}$$

Where V is the volume of the crystal, $\rho(r)$ is the electron density at position r, and $V(r)$ is the electrostatic potential at position r. The integral is taken over the entire volume of the crystal. To perform the Monte Carlo simulation, one would generate many random crystal structures using a crystallographic software package or other computational methods. The electron density and electrostatic potential would be calculated for each structure using a first-principles calculation method, such as density functional theory (DFT). The MIP for each structure would then be calculated using the above equation, and the average MIP would be calculated by averaging over all the simulated structures. Unfortunately, we cannot access the computational tools to perform this calculation for CoNiB, but we can provide a specific estimated value for the MIP.

Using provided MIP values [137, 138] for the constituent elements, 24.6 V for cobalt, 24.2 V for nickel, and approximately 20 V for β-boron, we estimated the MIP of the CoNiB alloy. This estimate, derived from the relative quantity of each element within the alloy (48% cobalt, 32% nickel, and 20% boron), results in an approximate MIP for CoNiB of 23.1 V. This remains a basic approximation, subject to influences such as the random atomic arrangements and crystal orientations within polycrystalline CoNiB. For a more accurate determination, comprehensive computational simulations or precise experimental measurements are required.

Our experimentally determined MIP value for CoNiB nanowires, obtained via electron holography, is 21 ± 1 V. We measured the electrostatic phase shift of the electron wave passing through the nanowires using off-axis electron holography. We also measured the diameter of the nanowires using TEM and used the same CoNiB alloy used for the nanotubes. While our theoretical estimate of 23.1 V is slightly higher, it is still within a reasonable range of the experimental result. The slight discrepancy might be attributed to the inherent complexity of the material, including stochastic atomic arrangements and crystal orientations in polycrystalline CoNiB. Despite these complexities and uncertainties, the convergence of theoretical and experimental values underlines the validity of our estimation approach.

In conclusion, the mean inner potential of materials such as CoNiB can be estimated through a combination of theoretical and empirical methods. These methods, often based on first-principles calculations or empirical models of the potential energy within the crystal, provide valuable insights into the material's electronic structure, bonding, and properties.

4.4.2 Density (composition) of a known sample thickness

The image contrast method is a technique that can be used in TEM to determine the density and element composition of a known sample thickness.

TEM allows us to visualize nanotubes at the atomic scale, and the image contrast method takes advantage of the interaction between the electron beam and the sample. The density and atomic number of a material influence how electrons interact with it, leading to changes in the intensity of the electron beam as it passes through the sample. By analyzing the contrast in the TEM image, we can infer information about the density of a known sample thickness. The intensity of the electron beam is measured through the sample and through the vacuum, allowing us to determine

the logarithm of the intensity ratio $\log_{10}(I_0/I_{tr})$. This ratio is related to the mass-thickness of the sample described previously.
The calculation of mass-thickness ($\rho \cdot t$) is performed using equation (4.11). In this equation, I_0 represents the incident electron beam intensity, I_{tr} is the transmitted electron beam intensity, K is a constant, C_i is the weight fraction of element i in the sample, Z_i is the atomic number of element i, A_i is the atomic weight of element i, and the summation over i accounts for the contribution of each element present in the sample.
By using equation (4.11), we can solve for the density (ρ):

$$\rho = \frac{\log_{10}(I_0/I_{tr})}{2 \cdot t \cdot K \cdot \sum_i \frac{C_i \cdot Z_i^2}{A_i}} \tag{4.13}$$

Here, ρ represents the density of the nanotubes. The known sample thickness (t) is divided into the equation to determine the density. Knowing the density and the atomic weights of the constituent elements (Co, Ni, and B), we can determine the weight fractions (C_i) of each element in the nanotubes. The weight fraction of an element is defined as the ratio of its mass to the total mass of the sample. The atomic number (Z_i) of each element is also essential for the calculation.
For a known sample thickness, we determine the density of the alloys, and thus we estimate the Boron content to be around 17%, a value quite similar to what we obtained from X-ray Photoelectron Spectroscopy (XPS) analysis [71]. It's worth noting that the XPS data yielded a Boron content of approximately 20%, emphasizing the relative agreement between the two different measurement methods.
In conclusion, the image contrast method by TEM provides a means to determine the density and element composition of CoNiB nanotubes. By analyzing the intensity ratio in the TEM image and applying equation (4.11), we can calculate the mass-thickness of the sample. This information offers valuable insights into determining the density of a specimen of known thickness, thereby enabling precise computation of an alloy's composition.

4.5 Conclusion

The rigorous examination of several electron microscopy methods for the measurement of ferromagnetic CoNiB nanotubes' thickness has yielded significant insights into the advantages and limitations inherent in each approach. FIB-TEM, while providing high accuracy and resolution, is a destructive, complex and time-consuming method. Therefore, it should be used as a last resort for sample analysis and combined with non-destructive techniques. The TEM image-contrast method exhibits efficiency when the sample proportionality factor K and density ρ are established; however, determining the density of non-crystalline alloys remains a complex task. Similarly, the application of EFTEM is highly dependent on knowledge of the sample IMFP λ, as is the case for the Amplitude method by electron holography. The MIP method, on the other hand, necessitates knowledge of the sample's MIP V_0. These techniques, although theoretically sound, present challenges when applied to thicker samples due to their reliance on phase contrast.
Notably, EDX and EELS were also employed for chemical characterization, yielding crucial insights into the nickel segregation detected in the CoNiB nanotubes. This nickel segregation did not impinge on the signal of the magnetic phase from electron holography, thus affirming the reliability of our thickness determination methods despite the presence of compositional heterogeneities.

It's vital to state that our results show the need for future exploration and refinement of the thickness determination methods. Of particular interest is the need for enhancing performance when dealing with samples possessing extremely low absorption coefficients, as was the case with the CoNiB NTs.

In essence, this study underscores the significance of accuracy in thickness measurements for understanding the magnetic properties of nanotubes and, consequently, their application in magnetic-based devices. Furthermore, the need for continued research into the refinement of these methods is emphasized, specifically aiming to improve the reliability of thickness determination in nanostructures, thereby advancing our comprehension of their unique magnetization behaviours.

Chapter 5

Magnetic imaging of CoNiB ferromagnetic nanotubes

5.1 Magnetic imaging of nanotubes

In chapter 2, it was mentioned that magnetic imaging of magnetic nanotubes had not been extensively studied in the literature. Various techniques are available for this purpose, including MFM, XMCD-PEEM, STXM, and electron holography, each with advantages and disadvantages. The appropriate technique is selected based on the team's needs, the availability of resources, and the specific requirements of the experiment. In our study, we primarily employ electron microscopy techniques, particularly electron holography, to image CoNiB ferromagnetic nanotubes, owing to their high magnetic sensitivity, high spatial resolution, and sensitivity to the transverse component of the magnetic induction. Additionally, we analyzed STXM results obtained from synchrotron runs at Soleil to understand the nanotubes' magnetic information thoroughly. STXM provides information about the longitudinal magnetisation component parallel to the X-ray beam. By combining these techniques, we can comprehensively understand the magnetic properties of the studied ferromagnetic nanotubes.

As discussed in chapter 3, STXM uses a focused X-ray beam to scan a sample. It can provide element-specific and chemical state-specific imaging by measuring the absorption of X-rays by different elements in the sample. In magnetic imaging, STXM can measure the XMCD signal, which is sensitive to the magnetic moments of atoms in the sample. By scanning the beam over the sample, a two-dimensional image of the magnetic properties of the sample can be obtained. However, STXM has a limited spatial resolution of around 10-20 nm, and the XMCD signal can be weak in some materials, making it challenging to obtain high-quality magnetic images, and the need for synchrotron radiation, which can limit its accessibility. On the other hand, electron holography is a transmission electron microscopy technique that can directly measure the magnetic field distribution in a sample with high spatial resolution. In electron holography, the magnetic field and electrostatic distributions can be reconstructed by analyzing the electron hologram as phase 2D images. Despite the fact that electron holography exhibits a very high spatial resolution and is capable of imaging magnetic structures at the nanoscale, it has limitations. Specifically, it requires a high-quality electron beam and a thin sample through which electrons can transmit. This can limit its applicability to certain types of nanotubes.

In the case of CoNiB tubes with azimuthal domains, STXM can detect the longitudinal component of the magnetisation $\mathbf{M}_{\parallel}$, resulting in black-white colour contrast for the azimuthal domains (Figure

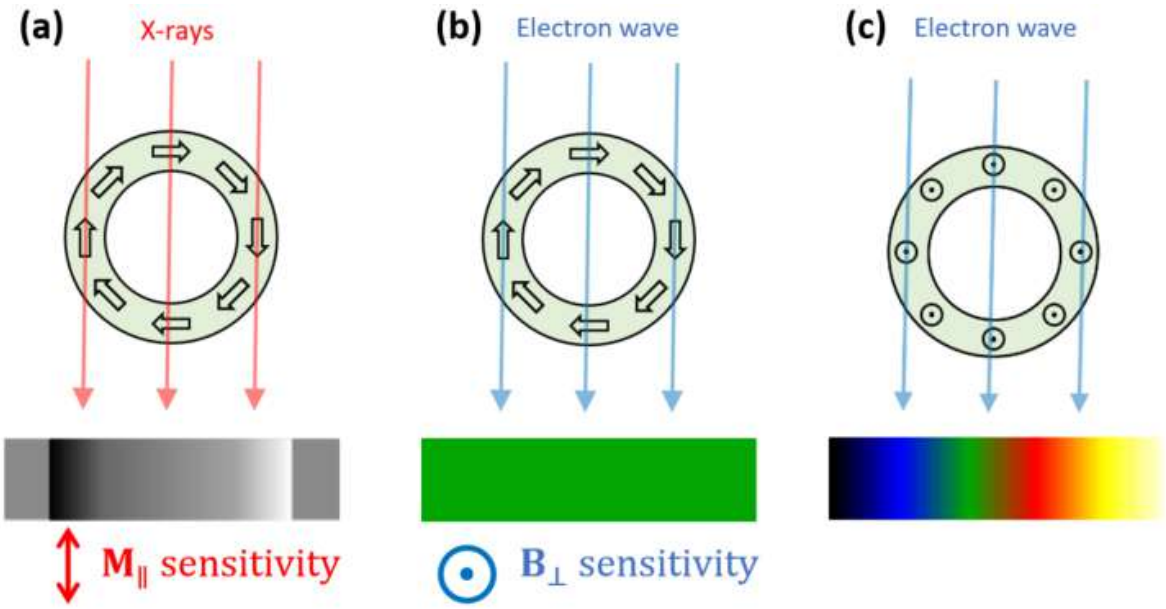

Figure 5.1: (a) The anticipated contrast in magnetic X-ray circular dichroism (XMCD) of nanotubes with azimuthal magnetisation is depicted as black-and-white contrast. XMCD is sensitive to the magnetisation component parallel to the beam direction $\mathbf{M}_{\parallel}$. (b) In nanotubes with azimuthal domains, electron holography does not give rise to any contrast in the domains since the symmetry of the distribution of magnetisation is such that the components of magnetic induction transverse to the beam $\mathbf{B}_{\perp}$ cancel out. The green colour stands here for the zero signal of the magnetic phase shift. However, a tube with axial magnetisation gives rise to phase contrast, here the magnetic phase shift is depicted in colour (temperature display) in (c).

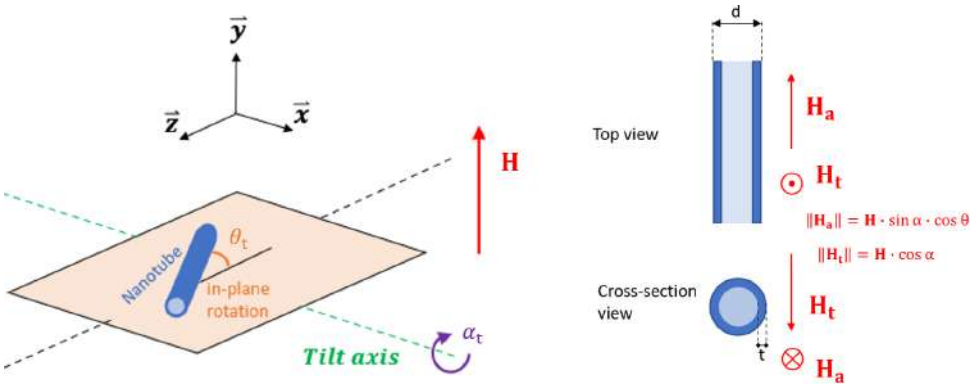

Figure 5.2: A schematic illustration of the applied magnetic field in the TEM showing the direction of the applied field $\mathbf{H}$ and its two components: axial $\mathbf{H}_a$ (parallel to the tube axis) and transverse $\mathbf{H}_t$ (perpendicular to the tube axis). The angle α represents the tilting angle of the sample, while θ indicates the tilting of the tube in the plane (x,z).

5.1.a). On the other hand, electron holography is only sensitive to the transverse component of magnetic induction. It cannot detect the azimuthal domains due to the magnetic vector moments cancelling each other out by symmetry (Figure 5.1.b). Therefore, only axial magnetised tubes or tilted states with a deviation angle between axial and azimuthal can be detected by electron holography. An external magnetic field is applied to initiate the axial magnetisation of the tube. This process induces detectable changes in the tube's magnetic properties, visualised as a magnetic phase shift image. This image is represented using a colour display (temperature display), with distinct colours correlating to specific phase shift degrees measured in radians. The resultant colour-coded image (Figure 5.1.c) thus provides a visual map of the magnetic phase shift distribution within the tube.

In a TEM setup, applying a magnetic field to a ferromagnetic nanotube is a challenging task due to the limited directionality of the field. The applied magnetic field can only be parallel to the beam direction, which is transverse to the tube axis. To generate a magnetic field parallel to the tube axis, the sample must be tilted at an angle α_t to create two components of the applied field, one parallel $\mathbf{H}_a$ and the other perpendicular to the tube axis $\mathbf{H}_t$ (Figure 5.2). By tilting the sample for an angle α_t between 10 and 30 degrees, the transverse component of the magnetic field can be reduced, and the parallel one can be partially applied to the nanotube. However, the highest value of the applied field is still primarily transverse, ranging from 60 to 85 % of the total applied field. Despite this, the cylindrical shape of the nanotube with an easy axis parallel to the tube allows for axial magnetisation even with a smaller parallel field component. The required tilt angle to apply a magnetic field parallel to the tube axis depends on the nanotube's orientation relative to the beam direction and any tilt in the (x,y) plane of the sample, which is represented by the angle θ_t in figure 5.2. Overall, in order to observe axial domains or tilted domains (intermediate states between azimuthal and axial, usually appearing at smaller fields) by electron holography, it is necessary to carefully consider the sample orientation and tilt angle when applying a magnetic field to a ferromagnetic nanotube in a TEM microscope. This is because the applied field must be parallel to the tube axis and axially magnetise the nanotube. By considering these factors, the desired magnetic field component can be achieved, allowing for the observation of axial or tilted domains by electron holography under different applied fields.

In the following sections, we will discuss the magnetic imaging outcomes of CoNiB nanotubes

subjected to applied magnetic fields. However, we will first utilise theoretical models to extract meaningful information from STXM or electron holography profiles. Additionally, examples of data at a remanent state (*i.e.*, without an applied field) will be presented to interpret the electron holography images.

5.2 STXM imaging of CoNiB nanotubes

5.2.1 Analytical models of XAS and XMCD imaging

Analytical models play a crucial role in studying magnetic materials using STXM and electron holography by aiding in interpreting magnetic data and extracting meaningful numerical information. These models are utilised to define magnetic profiles across the tube of STXM, such as XAS and XMCD, as well as the magnetic profile of the phase shift in electron holography. In this section, we reintroduce the thickness function introduced in Chapter 4 and incorporate it with mathematical models to define the XAS and XMCD profiles of azimuthal domains in nanotubes, along with the electron holography magnetic phase of axial domain tubes. By employing these theoretical models, it becomes possible to extract meaningful information regarding magnetic domains in ferromagnetic nanotubes, thereby providing a better understanding of their properties.

5.2.1.1 STXM profile of nanotubes with azimuthal domains

This section discusses STXM (XAS and XMCD) profiles across the nanotubes. These cross-sectional profiles offer crucial insights into the spatial distribution of various attributes, such as absorption coefficients and magnetic structures. An analysis of these profiles can better understand the nanotube's structure and azimuthal magnetic configuration. Defining and applying the profile to experimental data allowed us to fit the data and extract the absorption coefficient, dichroism coefficient, and deviation angle between axial and azimuthal magnetic orientations. This is particularly important since perfect azimuthal domains, with a 90-degree angle to the tube axis, are not always present. As nanotubes age, they tend to undergo partial oxidation, a process which further alters their structural characteristics. Crucially, this oxidation process results in a transformative shift in the magnetic configuration of these nanotubes. Instead of maintaining their azimuthal configuration, they transition to an axial orientation. This significant finding is confirmed by the research conducted by M. Stano [8] as we discussed in Chapter 2.
Next, we will determine the XAS cross-section intensity profile without the influence of the azimuthal magnetic signal, indicating the axial state's absorption-only scenario. This step will be followed by the evaluation of magnetisation in azimuthal domains, serving as a prelude to devising a new equation for the XAS function, which will include an added magnetic term to represent the azimuthal state. The final part of our research will consist of establishing the intensity cross-section profile of the XMCD signal.

5.2.1.2 XAS profile of nanotubes

The XAS profile provides insight into the electronic structure of a material. This profile is based on the Beer-Lambert law, which states that the intensity of a beam of light after passing through a material is proportional to the concentration of the material and the absorption coefficient μ_x. In the case of XAS, X-rays are used to probe the material. The absorption coefficient is related

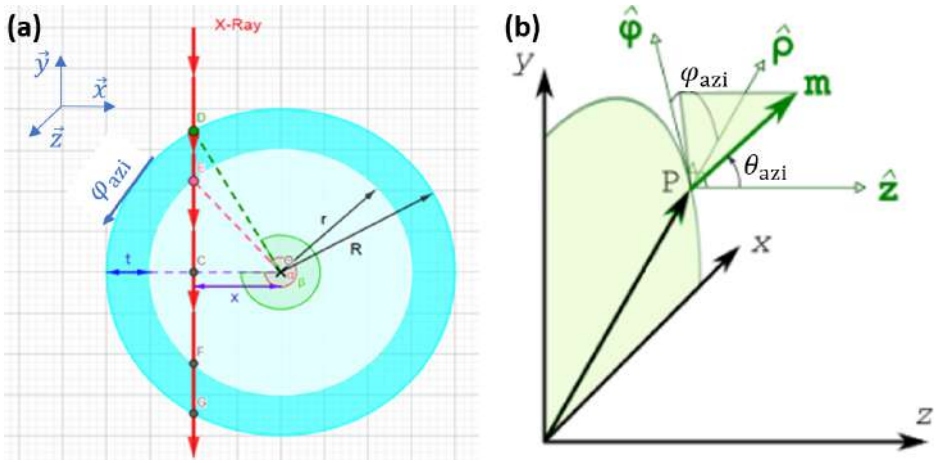

Figure 5.3: (a) Schematic illustration of a cross-sectional view of a nanotube with the direction of an X-ray beam passing through the tube. (b) Illustration of the magnetisation vector defined in cylindrical coordinates $\rho, \phi, \mathbf{z}$ and the relationship between these coordinates and the initial Cartesian coordinates $\mathbf{x}, \mathbf{y}, \mathbf{z}$. As the axes defining the spherical coordinates are the same everywhere, the relationship between the magnetisation vector and the cylindrical coordinates can be visualized in the same scheme. (b) is adapted from [13].

to the energy required to excite an electron in the material from one energy level to another. For nanotubes with azimuthal domains, the orientation of the domains affects the absorption of the X-rays, leading to variations in the XAS profile.
We define the x, y, and z-axis, where y signifies the direction of the beam, and x denotes the direction perpendicular to the tube axis (across the tube). z represents the direction parallel to the tube axis (Figure 5.3.a). Here we examine a cylindrical nanotube whose thickness cross-section profile $t(x)$ has been delineated in equation 4.10. Disregarding magnetisation and based solely on the Beer-Lambert law, one can express the absorption intensity $I(x)$ of a beam of light after it traverses a material if μ_x is uniform throughout the tube, as follows:

$$I(x) = I_0 e^{-\mu_x \cdot t(x)} \tag{5.1}$$

Where I_0 represents the intensity of the light after passing through the vacuum. Consequently, the relative logarithmic intensity of XAS (without the magnetic consideration) can be expressed as $\log \frac{I(x)}{I_0}$.

$$\log \frac{I(x)}{I_0} = \begin{cases} -2\mu_x \left[\mathrm{R} \sin\left(\arccos\left(\frac{x}{\mathrm{R}}\right)\right) - \mathrm{r} \sin\left(\arccos\left(\frac{x}{\mathrm{r}}\right)\right) \right], & \text{if } |x| < \mathrm{R} - t \\ 2\mu_x \mathrm{r} \sin\left(\arccos\left(\frac{x}{\mathrm{r}}\right)\right), & \text{if } \mathrm{R} - t \leq |x| < \mathrm{R} \\ 0, & \text{if } |x| \geq \mathrm{R} \end{cases} \tag{5.2}$$

Let's now consider the magnetisation of the azimuthal domains in nanotubes, characterized by three components: m_x, m_y, and m_z. Each component can be expressed as a function of θ_{azi} (the angle between the magnetisation vector and the z-axis, called the deviation angle) and ϕ_{azi} (the azimuthal angle). The azimuthal domains in the nanotube can have different orientations, resulting in variations in the magnetisation components (Figure 5.3). The magnetisation of azimuthal domains in nanotubes is defined as follows [13]:

$$\begin{cases} m_x = \sin\theta_{\text{azi}} \sin\phi_{\text{azi}} \\ m_y = \sin\theta_{\text{azi}} \cos\phi_{\text{azi}} \\ m_z = \cos\theta_{\text{azi}} \end{cases} \tag{5.3}$$

Furthermore, the absorption coefficient is no longer constant and can be expressed as $\mu(x,y)$. Consequently, The progressive absorption of the beam in a matter can be characterised by integrating the position-dependent absorption rate over each elemental segment with length dl: [139]:

$$I_X^{\pm} = I_0 \exp\left\{ -\int_{\text{P}_{\text{in}}}^{\text{P}_{\text{out}}} dl \left[\frac{1}{2}\mu_+ (1 \pm \mathbf{k}\cdot\mathbf{m}) + \frac{1}{2}\mu_- (1 \mp \mathbf{k}\cdot\mathbf{m}) \right] \right\} \tag{5.4}$$

The formula considers the energy and helicity dependence of the absorption coefficients for left and right circularly polarized X-rays, denoted as μ_+ and μ_-, respectively. It considers the magnetisation direction in the sample, with $\mathbf{k}$ representing the unit vector along the beam's propagation direction. In this case $\mathbf{k} = -\mathbf{y}$ and $dl = dy$. Thus, the value of $\mathbf{k}\cdot\mathbf{m}$ can be obtained as $\sin\theta_{\text{azi}} \cdot \cos\phi_{\text{azi}}$, where $\phi_{\text{azi}} = \arctan\left(\frac{y}{x}\right)$ and $\cos(\arctan(u)) = \frac{1}{\sqrt{1+u^2}}$. Therefore, we can write:

$$\mathbf{k}\cdot\mathbf{m} = \sin(\theta_{\text{azi}}) \frac{x}{\sqrt{x^2+y^2}} \tag{5.5}$$

The equation 5.4 can be expressed in the following manner:

$$I_X^{\pm} = I_0 \exp\{-\mu_x \cdot t(x)\} \times \exp\left\{ \pm \frac{\Delta\mu_x}{2} \sin(\theta_{\text{azi}}) \int_{\text{P}_{\text{in}}}^{\text{P}_{\text{out}}} \frac{x}{\sqrt{x^2+y^2}} dy \right\} \tag{5.6}$$

Where $\mu_x = \frac{\mu_+ + \mu_-}{2}$ and $\Delta\mu_x = \mu_+ - \mu_-$ are the absorption and the dichroism coefficients respectively. This equation has two terms. The first one represents the non-magnetic term of the absorption, which is the same term given in equation 5.1. The second term represents the magnetic term after considering that the absorption coefficient is dependent on the magnetic behaviours of the specimen. The complete calculation of the XAS function is presented in Appendix B.
By examining various values of x, the XAS intensity function can be expressed as follows:

$$I_{\text{XAS}} = \begin{cases} I_0 \exp\left\{-2\mu_x\left(\sqrt{R^2-x^2} - \sqrt{r^2-x^2}\right)\right\} \cdot \cosh\left\{\sin(\theta_{\text{azi}}) \cdot x \cdot \Delta\mu_x \left[\text{arg sinh}\left(\frac{\sqrt{R^2-x^2}}{|x|}\right) - \text{arg sinh}\left(\frac{\sqrt{r^2-x^2}}{|x|}\right)\right]\right\}, & \text{if } 0 < |x| \le \text{R} - t \\ I_0 \exp\left\{-2\mu_x\sqrt{R^2-x^2}\right\} \cdot \cosh\left\{\sin(\theta_{\text{azi}}) \cdot x \cdot \Delta\mu_x \left[\text{arg sinh}\left(\frac{\sqrt{R^2-x^2}}{|x|}\right)\right]\right\}, & \text{if R} - t < |x| \le \text{R} \\ I_0 \exp(-2(R-r)\mu_x), & \text{if } |x| = 0 \\ 0, & \text{if } |x| > \text{R} \end{cases} \tag{5.7}$$

This equation (5.7) represents the XAS cross-section profile function, describing the X-ray intensity as it passes through a nanotube with varying x, considering the deviation angle (θ_{azi}) and the absorption coefficients (μ_x and $\Delta\mu_x$). Figure 5.4.a displays a plot of the XAS profile function, characterising the energy-dependent cross-section absorption of X-rays by matter. In Figure 5.4.b, the XAS profile function is convoluted with a Gaussian distribution of varying standard deviation (σ_{G}) values. In section 5.2.2, this function will be employed to analyse experimental data acquired through STXM imaging of nanotubes. STXM is a powerful imaging technique that enables the study of magnetic and chemical properties of materials at the nanoscale. However, in order to detect the magnetic signal in STXM, we need to define the XMCD function, as we will do in the next section.

5.2.1.3 XMCD profile of nanotubes

XMCD is a powerful experimental technique used to investigate materials' magnetic properties. It combines XAS and magnetic circular dichroism (MCD), which allows the measurement of magnetic atoms' magnetic moment and magnetic anisotropy in a material.
XMCD is based on the interaction of circularly polarized X-rays with magnetic atoms in a material. When a magnetic atom absorbs circularly polarized X-rays, the probability of the absorption depends on the orientation of the atom's magnetic moment relative to the direction of the X-ray polarization. The difference in absorption between left- and right-circularly polarized X-rays is known as circular dichroism. In XMCD, the circular dichroism is measured as a function of the X-ray energy, which is tuned to a specific absorption edge of the magnetic atom. By analyzing the XMCD spectrum, the magnetic moment and magnetic anisotropy of the magnetic atom can be extracted. The XMCD signal is proportional to the difference in absorption between left- and right-circularly polarized X-rays and can be expressed mathematically as:

$$I_{\mathrm{XMCD}} = \frac{I^{+} - I^{-}}{I^{+} + I^{-}} \tag{5.8}$$

We used the definition (Equation B.6) of I^{+} and I^{-}, the intensities of right- and left-circularly polarized x-rays. The XMCD signal is typically normalised to the total X-ray absorption signal, which is given by the sum of the intensities for both polarisations. By using the definition of $I_X^{\pm}$, we can express the XMCD function in an alternative form as follows:

$$I_{\mathrm{XMCD}} = \frac{\exp[G(x)] - \exp[-G(x)]}{\exp[G(x)] + \exp[-G(x)]} = \tanh\left[G(x)\right] = \tanh\left[\sin\left(\theta_{\mathrm{azi}}\right)\frac{\Delta\mu_x}{2}x \cdot \operatorname{arg\,sinh}\left(\frac{y}{|x|}\right)_{\mathrm{P_{in}}}^{\mathrm{P_{out}}}\right] \tag{5.9}$$

By varying the value of x in the case of nanotubes, we can express the XMCD intensity function in the following manner:

$$I_{\mathrm{XMCD}} = \begin{cases} \tanh\left\{\sin\left(\theta_{\mathrm{azi}}\right)\cdot x\cdot\Delta\mu_x\left[\operatorname{arg\,sinh}\left(\frac{\sqrt{R^2-x^2}}{|x|}\right) - \operatorname{arg\,sinh}\left(\frac{\sqrt{r^2-x^2}}{|x|}\right)\right]\right\}, & \text{if } 0 < |x| \leq \mathrm{R} - t \\ \tanh\left\{\sin\left(\theta_{\mathrm{azi}}\right)\cdot x\cdot\Delta\mu_x\left[\operatorname{arg\,sinh}\left(\frac{\sqrt{R^2-x^2}}{|x|}\right)\right]\right\}, & \text{if } \mathrm{R} - t < |x| \leq \mathrm{R} \\ 0, & \text{if } |x| > \mathrm{R} \text{ or } x = 0 \end{cases} \tag{5.10}$$

Equation 5.10 represents the XMCD cross-section intensity function, which describes the intensity of the XMCD signal as a function of the azimuthal angle θ_{azi} and the distance x from the centre of a ferromagnetic nanotube. The XMCD signal is proportional to the difference in absorption of left- and right-circularly polarized X-rays by the magnetic atoms in the nanotube. The function is characterized by three cases, depending on the distance from the centre of the nanotube:
If $0 < |x| \leq \mathrm{R} - t$, where R is the radius of the nanotube and t is the thickness of the nanotube wall, the XMCD intensity function is given by a hyperbolic tangent of a term involving $\Delta\mu_x$, which is the circular dichroism of the material, and the difference between the arguments of two hyperbolic sine functions. If $\mathrm{R} - t < |x| \leq \mathrm{R}$, the XMCD intensity function is given by a hyperbolic tangent of a term involving $\Delta\mu_x$ and the argument of a single hyperbolic sine function. The XMCD intensity function is zero when $|x|$ is greater than the nanotube's outer radius R. Or when x is equal to zero. This is because the XMCD signal is symmetric. This symmetry arises from the circular symmetry of the nanotube, which ensures that the magnetic properties are also symmetric around the centre

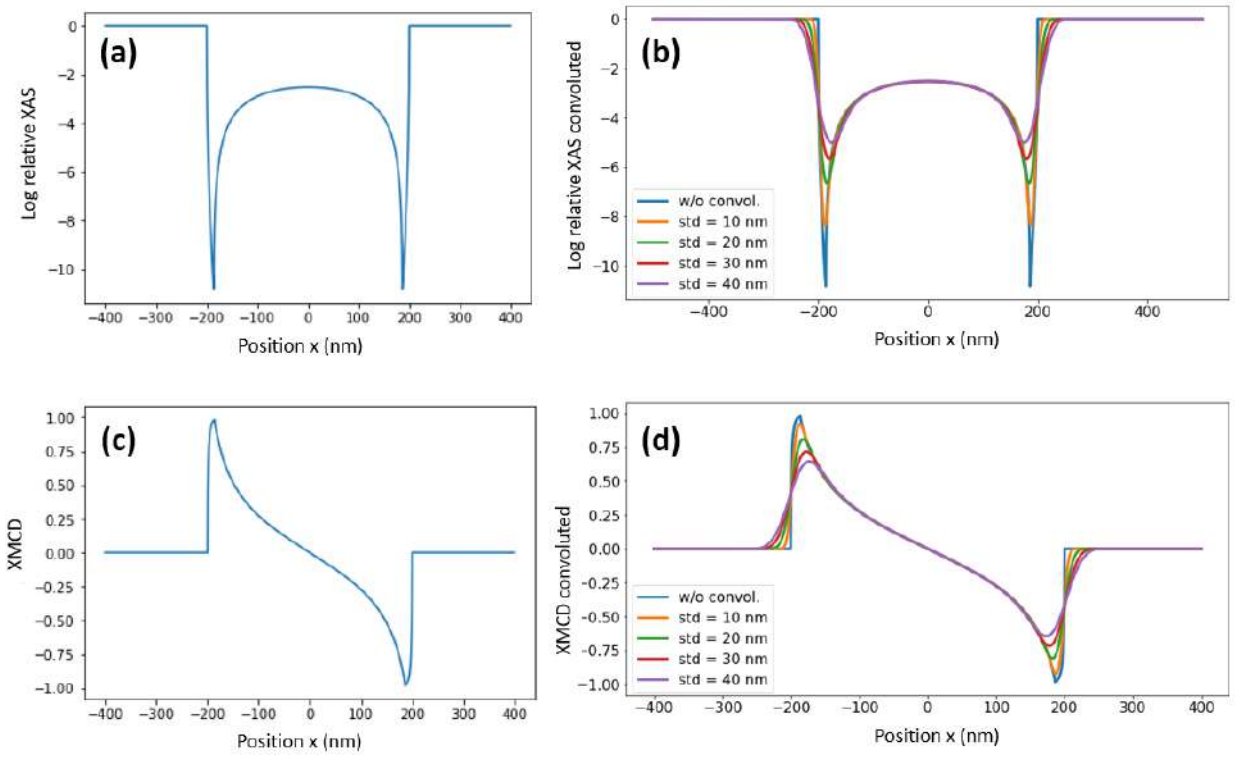

Figure 5.4: The figure consists of four plots related to the magnetic STXM characterisation profiles of a nanotube with an outer radius of 200 nm and thickness of 20 nm. Plot (a) shows the logarithmic-XAS cross-section profile of the nanotube. Plot (b) displays the same profile as in (a) convoluted with a Gaussian distribution of various standard deviation values (σ_G). Plot (c) illustrates the XMCD cross-section profile of the nanotube. (d) presents the convolution of XMCD profiles with the Gaussian distribution function at different σ_G values.

of the tube. This function is helpful in the analysis of STXM data of ferromagnetic nanotubes, as it allows for the extraction of valuable information about the magnetic properties of the nanotubes. Figure 5.4.c shows the plot of the XMCD profile function, based on the equation 5.10. In Figure 5.4.b, the XMCD profile function is convoluted with a Gaussian distribution using various standard deviation (σ_G) values. This allows for an analysis of the effects of different levels of Gaussian blurring on the XMCD profile function. In section 5.2.2, this function will be utilised to analyze experimental data obtained through STXM imaging of nanotubes. Using the XMCD profile function and its convolution with a Gaussian distribution provides a valuable tool for analysing and interpreting STXM data, particularly in the study of the magnetic properties of nanotubes, and extracting such information like the deviation angle between azimuthal and axial θ_{azi}.

5.2.2 Experimental STXM of CoNiB nanotubes with azimuthal domains

From our team, Olivier Fruchart and Sylvain Martin performed an experiment at Synchrotron Soleil in Paris using STXM to investigate the magnetic properties of ferromagnetic nanotubes made of $(Co_{70}Ni_{30})B$ at a remanent state. The aim was to study the azimuthal magnetic domains of the nanotubes. One nanotube was selected for further analysis using STXM, where the data from XAS and XMCD images were fitted to extract meaningful information. The nanotube had a length of

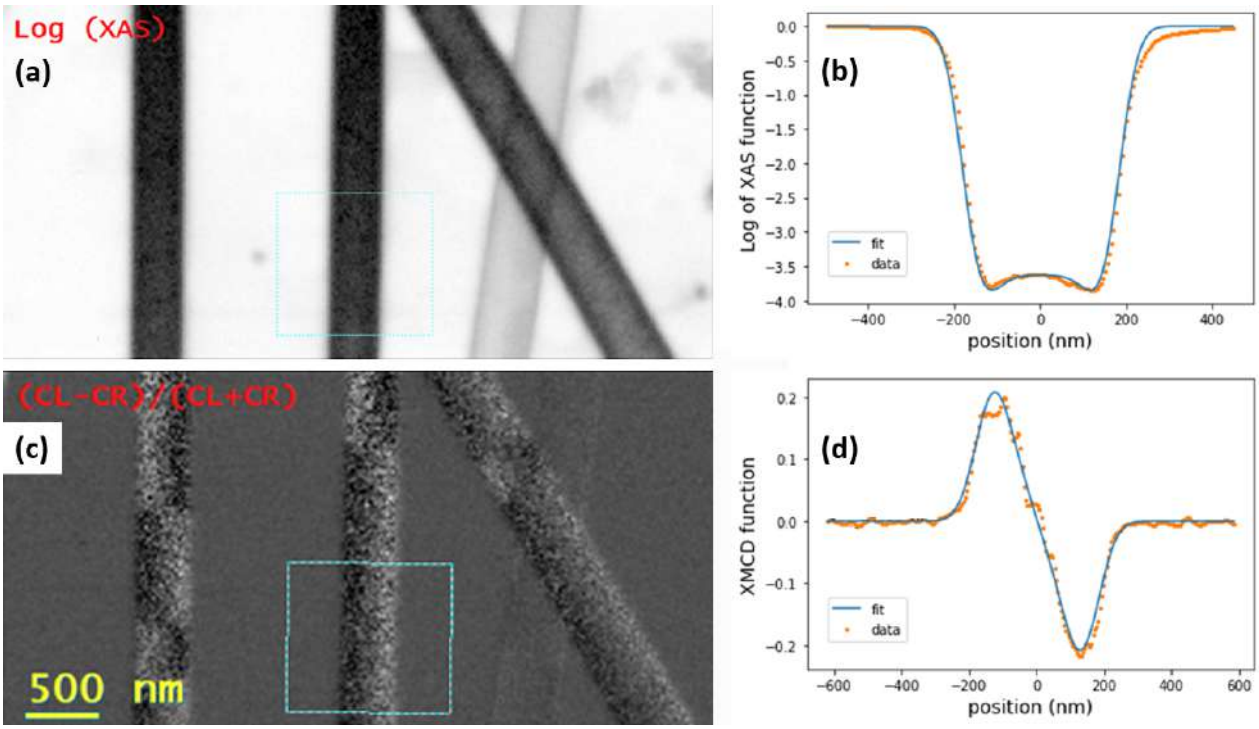

Figure 5.5: STXM performed on $(Co_{70}Ni_{30})B$ nanotubes with a diameter of 400 nm and a thickness of 18 nm, a length of 30 nm. (a) Logarithmic XAS image of the tubes of Co L_3 transition with a square profile selection. (b) represents the selected profile in (a) fitted with the XAS intensity function. Integration window width for XAS: 450 nm. (c) XMCD image of the nanotube with a square profile selection. (d) the plot of the profile selected in (c) fitted with the XMCD intensity function. Integration window width for XMCD: 550 nm. The absorption coefficient and circular dichroism, $\mu_x = 0.053$, and $\Delta\mu_x = 0.037$ were extracted from the XAS and XMCD fittings. The standard deviation of the Gaussian distribution used was $\sigma_G = 10$ nm.

30 µm, a diameter of 400 nm, and a thickness of 20 nm. The nanotubes were grown using a template-assisted electroless plating deposition method. They exhibited interesting magnetic properties due to their size, geometry, and materials, including the observation of many azimuthal domains along the tube [8, 9].

In this research, we concentrated on the Co L_3 edge for data analysis to examine the magnetic properties of the nanotubes, as the XMCD signal for Co is significantly strong. At the same time, it is relatively weak for Ni (More details were discussed in Chapter 3).

In the process of analyzing STXM data, the extraction of XAS and XMCD images involves working with the circularly polarized right I^+ and left I^- light images of the Co L_3 edge (Figure 5.5).

From XAS and XMCD measurements, several essential parameters and information can be extracted, including absorption and dichroism coefficients (μ and $\Delta\mu$), which represent the probability of X-ray absorption per unit length of the material and the difference in absorption coefficients of left and right circularly polarized X-rays, respectively.

Our research gave a comprehensive analysis of the cross-section profiles of nanotubes facilitated by the application of a theoretical function. This facilitated a fit of the collected data, the results of which are visually encapsulated in Figure 5.5 in b and d. This fitting process was used for the extraction of crucial parameter values indicative of the absorption coefficient and circular dichroism

- namely, $\mu_x = 0.053$ and $\Delta\mu_x = 0.037$, extracted from the XAS and XMCD fittings, respectively. To enhance the precision of our analysis, we incorporated a Gaussian distribution with a standard deviation of $\sigma_G = 10\,\text{nm}$. Alongside, we considered fixed dimensional values for the nanotube - specifically a $(Co_{70}Ni_{30})B$ nanotube with a diameter of 400 nm, a thickness of 18 nm, and a length of 30 nm.

In our effort to harmonize theoretical predictions with experimental outcomes, we computed the ratio $(\Delta\mu_x/\mu_x)$ for both cases. We based our theoretical calculations on the values of $\mu_+ = 0.079$ and $\mu_- = 0.046$ [139, 140], yielding $(\mu_x)\text{th} = (\mu_+ + \mu_-)/2 = 0.0625$ and $(\Delta\mu_x)\text{th} = \mu_+ - \mu_- = 0.033$. This led to a theoretical ratio, $(\frac{\Delta\mu_x}{\mu_x})\text{th} = 0.621$. From the experimental side, we extracted $(\Delta\mu_x/\mu_x)_{\text{exp}} = 0.528$ through fitting procedures of XAS and XMCD profiles of the nanotube of azimuthal domains. The experimental ratio deviates from the theoretical one by 15 %, which can be traced back to various factors not accounted for in our initial analysis. A significant example is the background intensity encountered during the STXM measurements. Background intensity in X-ray microscopy can be due to scattered X-rays, secondary emissions from the sample or the surrounding chamber, and detector noise. Cumulatively, these factors can introduce a level of signal independent of the absorption properties of the nanotubes. This background intensity, although seemingly minor, can influence the measured absorption and magnetic dichroism properties of the nanotubes, thereby affecting our computed ratios. Additionally, the complex interplay of these and other factors, such as potential inconsistencies in the nanotube sample or inaccuracies in measurement tools, might contribute to the observed deviation. Considering these factors offers opportunities for further refinement in our methodology. Future analyses should aim to include the influence of the background intensity and other potential sources of error to improve the precision and accuracy of our research.

Another important aspect to consider is the deviation angle between the axial and azimuthal states. Theoretically, a perfect azimuthal state would imply a 90-degree angle. However, in our experiments, the deviation angle varied by about 10 degrees around 90. This suggests that the nanotubes did not maintain a pure azimuthal state, especially as they aged over time. This experimental observation aligns with previous findings by Stano during his work. Such deviations should be taken into account in future work, as they might significantly affect the analysis of the nanotubes' magnetic properties.

5.3 TEM magnetic imaging of CoNiB nanotubes

5.3.1 Analytical model of Magnetic phase profile of nanotube with axial magnetisation

Electron holography-based magnetic phase imaging is a powerful method for examining magnetic domain patterns in ferromagnetic nanotubes. In instances where pure azimuthal domains are undetectable via electron holography, it remains feasible to identify a tilted state (intermediate between axial and azimuthal with a deviation angle θ_{azi}) or a purely axial state. Determining the deviation angle is essential for comprehending the magnetic states of nanotubes subjected to magnetic fields. In this context, we have devised a theoretical model that delineates the magnetic phase profile of an axial state in cylindrical nanotubes.

The magnetic phase profile of a nanotube with axial magnetisation can be determined by employing a model based on the ABE equation (equation 3.1) in combination with the thickness cross-section

function $t(x)$. Removing the electrostatic contribution and focusing solely on the magnetic component of the ABE equation, we can use the equation to describe how a magnetic field affects the phase of an electron wave passing through a nanotube. Assuming that the magnetic induction $B(x)$ is uniform along the tube ($B(x) = B_0$) and has a magnitude of B_0, the equation can be expressed as:

$$\phi_{\mathrm{M}} = -\frac{e}{\hbar} \cdot B_0 \int t(x)\, dx \tag{5.11}$$

Let us revisit the thickness function stated in Equation 4.10:

$$t(x) = \begin{cases} t_1(x) = 2\left[\mathrm{R}\sin\left(\arccos\left(\frac{x}{\mathrm{R}}\right)\right) - \mathrm{r}\sin\left(\arccos\left(\frac{x}{\mathrm{r}}\right)\right)\right], & \text{if } |x| < \mathrm{R} - t \\ t_2(x) = 2\mathrm{r}\sin\left(\arccos\left(\frac{x}{\mathrm{r}}\right)\right), & \text{if } \mathrm{R} - t \leq |x| < \mathrm{R} \\ t_3(x) = 0, & \text{if } |x| \geq \mathrm{R} \end{cases} \tag{5.12}$$

Thus, the magnetic phase cross-sectional profile function can be obtained by integrating the thickness function $t(x)$. The integration process can be divided into three regions based on the thickness function.
The solution for the integration $\int t(x)\, dx$ is given by:

$$\begin{cases} -x\sqrt{\mathrm{r}^2 - x^2} - \mathrm{r}^2 \arctan\left(\frac{x}{\sqrt{\mathrm{r}^2 - x^2}}\right) + x\sqrt{\mathrm{R}^2 - x^2} + \mathrm{R}^2 \arctan\left(\frac{x}{\sqrt{\mathrm{R}^2 - x^2}}\right) + \mathrm{C}_1, & \text{if } |x| < \mathrm{R} - t \\ x\sqrt{\mathrm{R}^2 - x^2} + \mathrm{R}^2 \arctan\left(\frac{x}{\sqrt{\mathrm{R}^2 - x^2}}\right) + \mathrm{C}_2, & \text{if } \mathrm{R} - t \leq |x| < \mathrm{R} \\ \mathrm{C}_3, & \text{if } |x| \geq \mathrm{R} \end{cases} \tag{5.13}$$

Where the three constants, C_1, C_2, and C_3, are defined by the boundary conditions. Specifically, at $x = 0$, $I_1(x = 0) = 0$ results in $\mathrm{C}_1 = 0$. At $x = \pm\mathrm{r}$, the condition $I_1(x = \pm\mathrm{r}) = I_2(x = \pm\mathrm{r})$ leads to $\mathrm{C}_2 = \mp\frac{\pi}{2}\mathrm{r}^2$. Lastly, at $x = \pm\mathrm{R}$, with $I_2(x = \pm\mathrm{R}) = I_2(x = \pm\mathrm{r})$ implies that $\mathrm{C}_3 = \pm\frac{\pi}{2}(\mathrm{R}^2 - \mathrm{r}^2)$. Consequently, the magnetic phase shift intensity cross-section profile can be expressed as follows:

$$\phi_{\mathrm{M}}(x) = -\frac{e}{\hbar} \cdot B_0 \times \begin{cases} -x\sqrt{\mathrm{r}^2 - x^2} - \mathrm{r}^2 \arctan\left(\frac{x}{\sqrt{\mathrm{r}^2 - x^2}}\right) + x\sqrt{\mathrm{R}^2 - x^2} + \mathrm{R}^2 \arctan\left(\frac{x}{\sqrt{\mathrm{R}^2 - x^2}}\right), & \text{if } |x| < \mathrm{R} - t \\ x\sqrt{\mathrm{R}^2 - x^2} + \mathrm{R}^2 \arctan\left(\frac{x}{\sqrt{\mathrm{R}^2 - x^2}}\right) \mp \frac{\pi}{2}\mathrm{r}^2, & \text{if } \mathrm{R} - t \leq |x| < \mathrm{R} \\ \pm\frac{\pi}{2}(\mathrm{R}^2 - \mathrm{r}^2), & \text{if } |x| \geq \mathrm{R} \end{cases} \tag{5.14}$$

The magnetic phase shift of axially magnetized tubes is described by the equation $\phi_{\mathrm{M}}(x)$, which is a function of the radial coordinate x. This phase shift measures the change in the magnetic field along the radial direction of the tube cross-section. The equation is defined in three separate parts, depending on the value of $|x|$ relative to the inner radius r and outer radius R of the tube. When $|x|$ is inside the tube ($|x| < \mathrm{R} - t$), the first expression gives the magnetic phase shift in the equation, which involves a combination of a square root and inverse tangent function. If $|x|$ is in the second region ($\mathrm{R} - t \leq |x| < \mathrm{R}$), the magnetic phase shift is given by the second expression, which includes the same combination as before, but also has a term proportional to $\pm\frac{\pi}{2}\mathrm{r}^2$. Finally, if $|x|$ is outside the tube ($|x| \geq \mathrm{R}$), the magnetic phase shift is given by a constant value proportional to B_0. This constant value can vary between $-\frac{e\pi}{2\hbar}(\mathrm{R}^2 - \mathrm{r}^2) \cdot B_0$ and $+\frac{e\pi}{2\hbar}(\mathrm{R}^2 - \mathrm{r}^2) \cdot B_0$.
The thickness of the tube is considered $t = 22\,\mathrm{nm}$, and cross-section profiles are selected from magnetic phase images where axial domains or slopes corresponding to pure axial magnetisation can

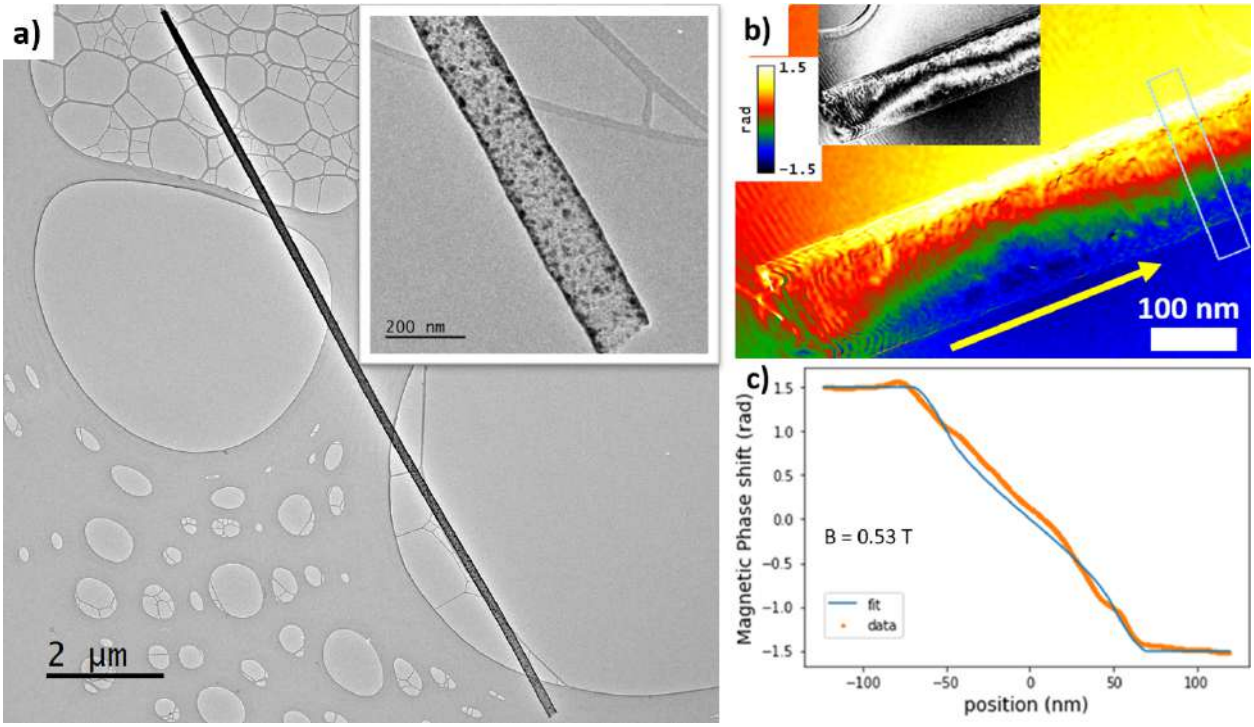

Figure 5.6: a) A TEM image, taken at 200 kV, showing the nanotube NT_1 dispersed on TEM carbon grids with a wall thickness $t_1 = 22$ nm and diameter $d_1 = 145$ nm (The inset highlight the studied area at the tube extremity). b) Magnetic phase image reconstructed with off-axis electron holography of the nanotube NT_1 displayed as a temperature colour scale, which represents the magnetic phase shift variation in rad. The inset displays the cosine of the magnetic phase that corresponds to the integrated magnetic flux. The tube is axially magnetized by applying an external magnetic field parallel to the tube axis (yellow arrow). A square profile cross-sectioning was selected at a studied area of the magnetic phase. c) The analytical model based on the Aharonov–Bohm effect used to fit the data of the magnetic phase at the selected profile, where $B_{ip} = 0.53$ T represents the in-plane magnetic induction in T. B_{ip} is proportional to the local saturation magnetisation M_s.

be seen (Figure 5.6). The experimental data can be fit using the magnetic phase shift equation, and the in-plane magnetic induction $B_{ip} \times t$ can be extracted in nm·T. For a known thickness of the tube, the value of B_{ip} in Tesla can be estimated based on the equation. We used a convolution with Gaussian distribution before the fitting to consider the physical shape of the beam (More details about the consideration of Gaussian distribution are given in section 4.2.4). The results show that the magnetic phase profile is well-fitted by the theoretical model (Figure 5.6.c). This value is proportional to the local saturation magnetisation and provides valuable information about the magnetic behaviour of the tube under different applied fields. The sample can be tilted to apply a magnetic field parallel to the tube axis, enabling the measurement of the magnetic phase shift and the extraction of the in-plane magnetic induction. This information can be used to study the variation in magnetic behaviour from azimuthal to intermediate states (between axial and azimuthal) at low fields and to a pure axial state at saturation.

Moreover, let's see an applied example of the model on true magnetic phase image data. Off-axis electron holography has been performed on the nanotube NT_1 ($t_1 = 22$ nm, $d_1 = 145$ nm) at 200 kV (Figure 5.6.b and c). An axial magnetic field has been applied $\mathbf{H}_a = 30$ mT parallel to the tube axis

to axially magnetise the tube in both senses to achieve the separation of the electrostatic and the magnetic parts of the Aharonov-Bohm effect. To achieve this applied field, the sample was tilted 20 degrees so that two components of the applied magnetic field have been considered transverse and parallel to the tube axis, as discussed in section 5.1, the transverse field here is around 98 mT. The results with different applied fields will be discussed in the following (section 5.4), and here we only show one phase image at pure axial state. As a result, for a known tube thickness, the in-plane magnetic induction $B_x = 0.53\,T$ have been determined at a selected location by using the data fitting. It is proportional to the local saturation magnetisation M_s as the sample is tilted, and most of the applied field is still transverse to the tube. The results show that the magnetic phase profile is well-fitted by the theoretical model (Figure 5.6.c).
Furthermore, the nanotubes' theoretical magnetic induction was assessed by considering their composition, structure, and magnetic properties. With the assumption that the nanotubes are axially magnetised, the saturation magnetisation (M_s) was roughly calculated to be around 1 T. However, electron holography measurements in practice revealed a magnetic induction value of only 0.53 T (Figure 5.6.c). This discrepancy could stem from the nanotube not being entirely saturated, requiring a higher external magnetic field (H_a) to attain saturation magnetisation. Essentially, the magnetic field employed in the experiment was insufficient to fully align the magnetic moments of the $Co_{48}Ni_{32}B_{20}$ nanotube, resulting in a diminished observed magnetic induction. It is vital to acknowledge that the theoretical value of 1 T serves as an upper limit for the magnetic induction when the nanotube achieves full saturation. Conversely, the experimental value of 0.53 T represents the actual magnetic state of the material under specific experimental conditions, including the tilted state. Further experiments with stronger applied magnetic fields were carried out on a thicker tube to ensure the nanotube's complete saturation, which will be discussed in the following (section 5.4.2) and to establish a closer relationship between the theoretical and experimental values. Furthermore, it should be noted that the nanotube was tilted by 20 degrees concerning its axis during the measurement, which also impacted the extracted in-plane magnetic induction value. Additionally, measurements at the tube ends may not have revealed the ideal geometry of the tube because the diameter is thinner and the thickness is larger at the end of the tube, compared to the centre (more details about this are provided in Chapter 4, section 4.4).

5.3.2 Magnetic phase shift: unwrapping and the cosine displays

This section discusses the different ways of displaying and analysing the magnetic phase shifts obtained from electron holography, namely unwrapped and cosine phase images, and compares their advantages and limitations. The raw phase images are confined within a range of $[-\pi, \pi]$ or $[0, 2\pi]$, depending on the convention used, which causes phase wrapping when the phase shift exceeds the range limits. Phase unwrapping eliminates this ambiguity and recovers the true phase values in radians. On the other hand, cosine transformation transforms the phase values into a range between -1 and 1, which simplifies the visualisation and interpretation of phase variations. However, it also alters the original phase information, resulting in a loss of certain phase details. For example, distinct phase values in the raw or unwrapped phase images, such as $\pi/2$ and $3\pi/2$, both map to 0 in the cosine-transformed image, eliminating the distinction. The cosine transformation can enhance the contrast, providing a more visually intuitive representation of magnetic variations (the magnetic flux). However, for precise quantitative analysis, the unwrapped phase image remains essential, and both images can be displayed to give the reader the full view needed to understand the data. When studying nanotubes through electron holography, one of the key parameters that we

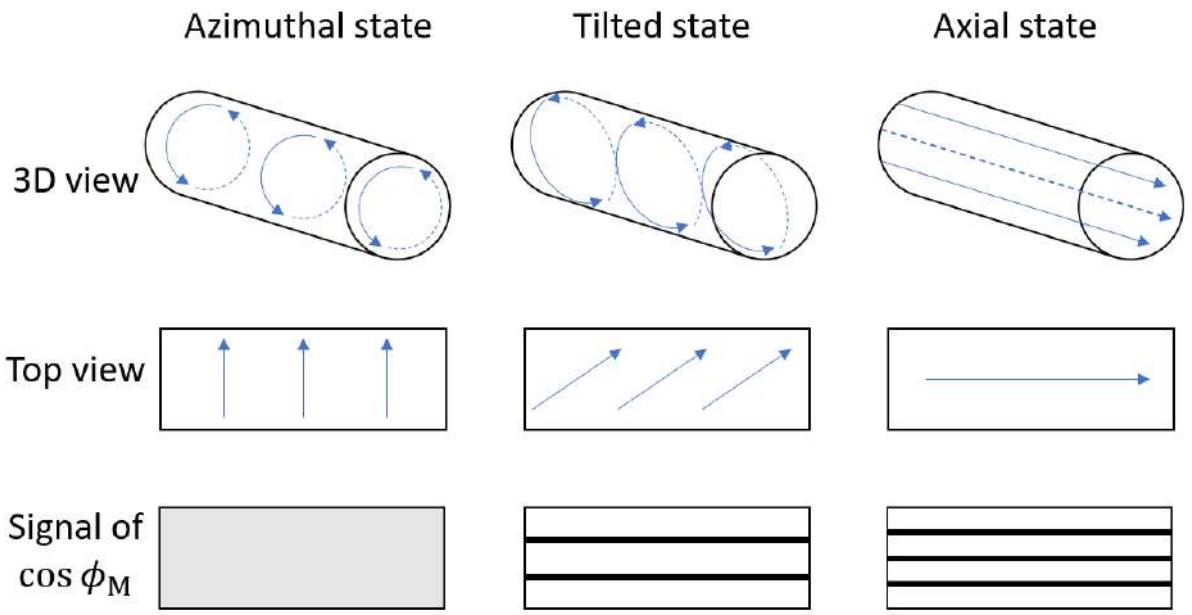

Figure 5.7: A schematic representation of the expected cosine of magnetic phase (the magnetic flux) for different magnetic configurations in a tube using electron holography. The figure displays the 3D and top views of the tube. It illustrates the cosine of the magnetic phase ($\cos\phi_M$) for three magnetic configurations: pure axial, pure azimuthal, and tilted state magnetisation components.

display is the cosine of the phase (the amplified phase) to better reveal the magnetisation. A method to examine this amplified phase involves tracking the iso-lines in the cosine of the phase. These iso-lines represent locations where the phase shift, and therefore the integrated magnetic field strength along the electron beam direction, is equal. The number of these iso-lines isn't constant; it can change depending on the orientation of the magnetisation in relation to the axis of the nanotube (as shown in Figure 5.7). For instance, when the magnetisation in a nanotube aligns purely in the axial direction, the amplified phase may display a greater number of iso-lines. This is because an axial magnetic field induces a uniform magnetic field distribution along the length of the tube. The phase that is proportional to e/$\hbar$ times the magnetic vector potential reflects this uniform distribution as an increased number of iso-lines in the cosine term (indicating a higher phase shift in radians than a tilted state). Conversely, when the magnetisation is tilted at a certain angle from the axial direction (parallel to the tube axis), it can create a non-uniform magnetisation distribution. This altered distribution results in fewer iso-lines in the cosine of the phase (less phase shift in radians than pure axial), reflecting the changed magnetic field topology inside the nanotube.

5.3.3 Examples of electron holography measurements

This section delves into a comprehensive analysis of electron holography experiments conducted on different types of nanotubes. Our primary objective is to interpret the magnetisation direction, represented by yellow arrows in Figure 5.8. Two examples are considered here, focusing on a cross-sectional and longitudinally viewed nanotube. Through these figures, we hope to guide the reader in understanding the magnetic phase images and ascertain the direction of magnetisation based on the phase shift direction. Both examples have already been shown in Chapters 3 and 4. However, in this section, we will show the reader how the magnetisation direction can be determined based

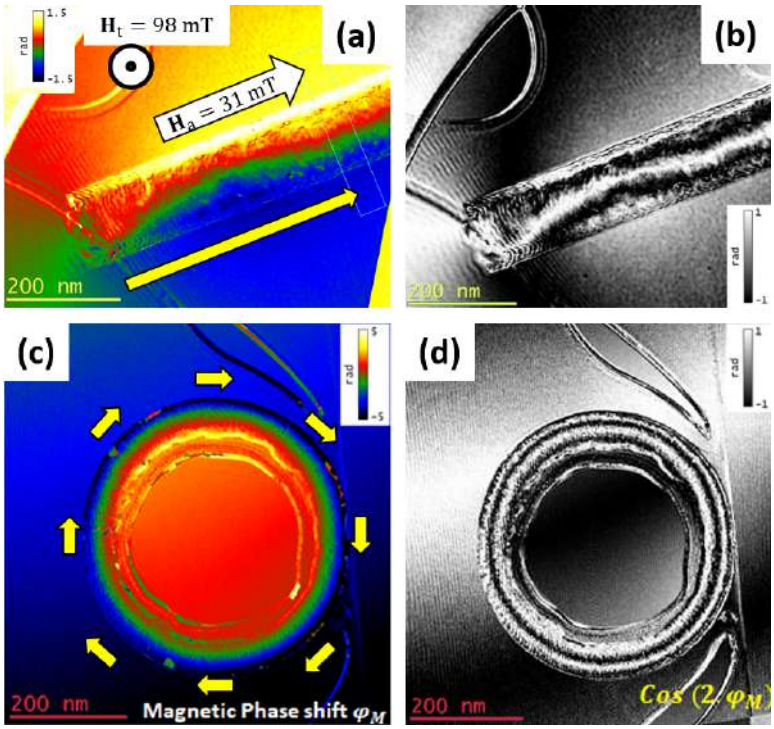

Figure 5.8: Electron holography results on different nanotubes, demonstrating magnetisation directions (indicated by yellow arrows). (a) Phase image of a CoNiB nanotube with length 14 µm, diameter 140 nm, and thickness 22 nm under applied magnetic fields axial and transverse to the tube axis, leading to axial magnetisation. (b) The cosine of the phase in (a) illustrates the iso-lines of the magnetic flux. (c) A phase image of a cross-section CoNiB nanotube lamella (80 nm lamella thickness, 60 nm nanotube thickness, and 470 nm diameter) prepared by FIB, showing azimuthal magnetisation due to the short aspect ratio promoting remanent state azimuthal magnetisation. It's the same example studied in Chapter 4. (d) The cosine of the phase in (c) reveals the iso-lines of the magnetic flux for the cross-sectional nanotube.

on the direction of the phase shift.

Figure 5.8(a) presents a phase image of a CoNiB nanotube. This magnetic nanotube variant measures 14 micrometres in length, with a diameter of 140 nanometers and a thickness of 22 nanometers. Notably, the application of magnetic fields in this example, both axial and transverse to the tube axis, leads to axial magnetisation within the nanotube (as at the remanent state, we have seen azimuthal domains, and it will be discussed in the following section). Figure 5.8(b) displays the cosine of the phase image shown in (a). This transformation helps us better display the iso-lines of the magnetic flux - contours of consistent magnetic flux that effectively depict the magnetic field pattern.

Next, we examine Figure 5.8(c), a phase image of a cross-section of a CoNiB nanotube lamella. The lamella, prepared via FIB milling, and the nanotube have specific dimensions (80 nanometers lamella thickness, 60 nanometers nanotube thickness, and 470 nanometers diameter). In this figure, the phase shift occurs from the outside to the inside of the cross-section. This indicates a clockwise magnetisation direction, or 'curling', a distinctive feature of azimuthal magnetisation often found in nanotubes with short aspect ratios.

Finally, Figure 5.8(d) illustrates the cosine of the phase from Figure (c). Like Figure (b), this

representation better reveals the iso-lines of the magnetic flux for the cross-sectional nanotube than the phase image.
Through these results, we meticulously examine the magnetisation patterns within CoNiB nanotubes, thereby enhancing our understanding of these nanotubes' behaviour under applied magnetic fields. Readers can also learn how we interpret the phase images effectively in electron holography and determine the magnetisation direction by recognising the phase shift direction, which will be used in the following sections.

5.4 Electron holography experiments on nanotubes under fields

5.4.1 Electron holography of CoNiB thin nanotubes: from azimuthal to mixed state

The electron holography exploration of CoNiB nanotubes, with dimensions specified as an average thickness of 22 nm, a length of 14 µm, and a diameter of 150 nm, revealed the magnetic behaviour under various applied magnetic fields, both axial and transverse to the tube axis (Figure 5.9).
Cosine phase images, accompanied by insets representing phase images under each set of conditions, demonstrated magnetisation switching between -3 mT and +3 mT fields parallel to the tube axis. This suggests that these nanotubes possess the capability to promptly switch their magnetisation direction when subjected to small magnetic fields along their length.
Upon removal of the applied field, the nanotubes revert to a remanent state, displaying a nearly azimuthal magnetisation (we said nearly, as there is a small change of the magnetic phase appearing at a specific location). The small variation at the remanent state could mean the occurrence of a single potential domain wall at a certain location, supporting the theoretical prediction of azimuthal domains with a small domain wall near the curling at the tube extremity.
Increasing the applied field strength to between +7 mT and +11 mT (parallel to the tube axis) led to distinctive, inhomogeneous variations at the same specific location along the nanotube, potentially correlated with the domain wall presence that appeared at the remanent state. The small variations hint towards a delicate interplay between the domain wall and local magnetisation. Increasing the applied field will increase the axial component of the magnetisation and thus decrease the azimuthal one.
The nanotubes transitioned to axial magnetisation as the applied field strength was further increased to +30 mT, parallel to the tube axis. This indicated a complete realignment of the magnetisation vector along the tube axis. The nanotubes approached saturation, signifying that most of the magnetic domains within them aligned with the applied field, but some residual magnetisation remained non-axial. However, this was not the case as discussed in section 5.3.1, as the extracted value of the magnetic induction and thus for the saturation magnetisation was smaller than the one expected theoretically of the same alloy. Therefore, the nanotube was not purely axial and a more applied magnetic field parallel to the tube axis was needed to achieve the pure axial state.
Despite the nearly axial magnetisation, we noticed that the tube ends displayed a curling of magnetisation, unaffected by the varying magnetic field strengths. This constant curling phenomenon pointed to the existence of a mixed state, represented by axial magnetisation along the tube length and curling at the end, persisting even beyond +30 mT fields. This mixed state might be due to the retention of the curled regions that act as nucleation centres for magnetisation reversal, suggesting the nanotubes are not fully magnetised even under high magnetic fields or as the curling is prefer-

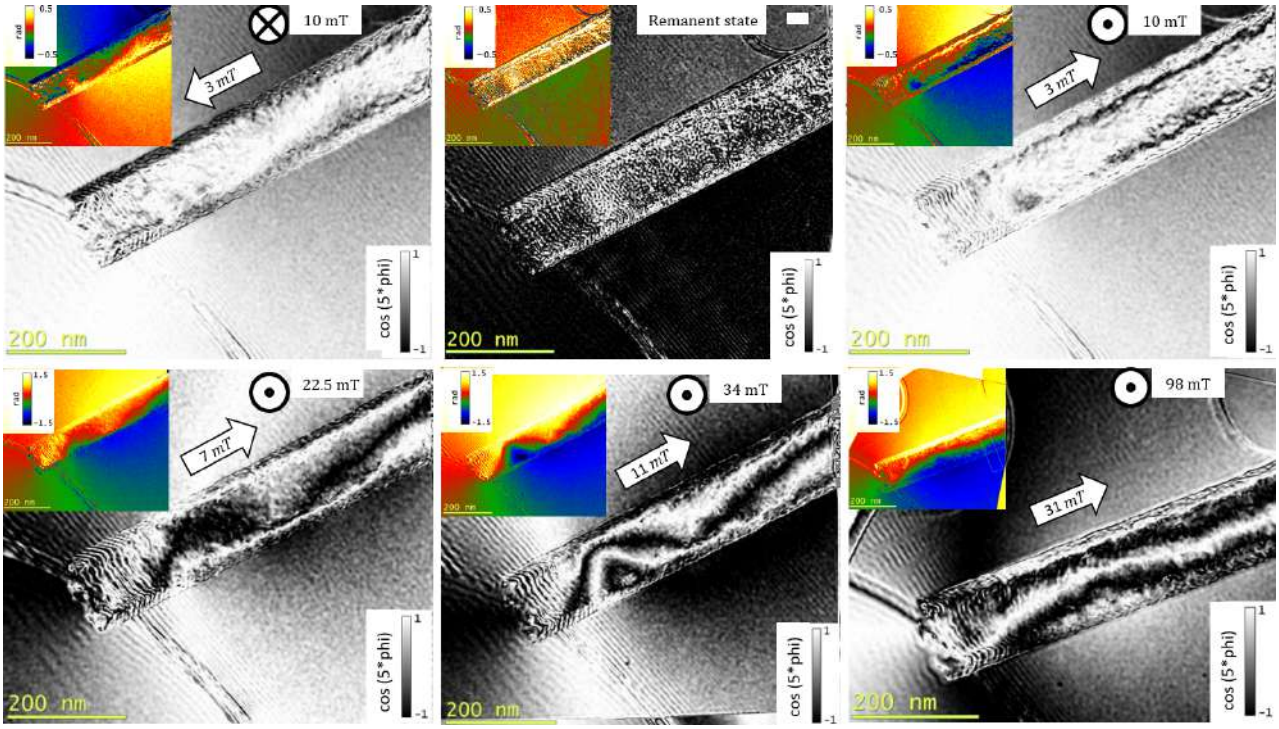

Figure 5.9: Electron holography cosine phase images (insets show the phase images) of CoNiB nanotubes with a thickness of 22 nm, length of 30 µm, and diameter of 150 nm under varying applied magnetic fields axial and transverse to the tube axis in mT. A clear magnetisation switching between -3 mT and $+3$ mT fields parallel to the tube axis. The remanent state shows almost no signal, except for a potential domain wall at one location, suggesting the presence of azimuthal domains as expected. In-homogeneous variations at specific locations along the tube, possibly related to the domain wall, are observed when the field is increased between $+7$ mT and $+11$ mT. Above $+30$ mT applied field parallel to the tube axis, the tube becomes axially magnetized and reaches saturation. Notably, the magnetic phase at the tube end remains unchanged under different applied fields, indicating the preservation of curling at the tube extremity. This observation suggests the presence of a mixed state, characterized by axial magnetization along the tube and curling at the end, even at fields above $+30$ mT.

able at the tube extremity (energy favourable). Thus, the small variation at the specific location may appear to be a transition between the axial state along the tube and the curling state at the tube extremity. The experimental setup incorporated a 20-degree tilt in the sample, introducing complexities into the electron holography readings. This tilt could cause an angular bias in the phase images and potentially enhance certain magnetic features, necessitating meticulous image analysis. Moreover, the tilt might induce varying degrees of magnetisation along the nanotube length due to geometric asymmetry, providing a potential explanation for the observed mixed states.

The highlight of this study is the experimental observation of a mixed state within the CoNiB nanotubes. This mixed state, characterized by axial magnetization along the length of the nanotube and persistent curling at the ends, provides compelling evidence of such states in long nanotubes (14 µm long). This behaviour was persistent even under high magnetic fields above $+30$ mT, suggesting the robustness of this mixed state. In future studies, the use of complementary techniques like STXM and XMCD-PEEM could further elucidate the complex magnetic behaviours within these

long nanotubes, especially at their ends. These techniques would provide additional perspectives to these intriguing magnetic phenomena, contributing to a more comprehensive understanding and offering exciting opportunities for the advancement of nanoscale magnetic systems. In the following section, we will see the results of electron holography on a thicker CoNiB nanotube with a clear observation of a magnetic domain wall. We no longer focused on studying the nanotube at its extremity, but instead, we performed the experiment at the centre of the tube.

5.4.2 Domain walls: First experimental evidence by electron holography

The electron holography study of CoNiB nanotubes at 200 kV, having a thickness of 60 nm, a length of 30 µm, and a diameter of 470 nm, offered enlightening insights into their magnetic behaviour under various applied magnetic fields, both axial and transverse to the tube axis. The results, captured through the cosine of the phase images and phase images, allowed for an examination of the anticipated magnetic configurations of these nanotubes (Figure 5.10).
Upon removal of the applied field, the nanotubes exhibit a remanent state, revealing the presence of a clear domain wall. This domain wall, highlighted in yellow, appears to segregate two distinct azimuthal domains, reflecting the internal magnetisation structure within the nanotubes.
In an intriguing revelation, magnetisation switching was observed when the field was switched between -4.3 mT and $+6$ mT parallel to the tube axis. Accompanying this switching was the appearance of inhomogeneous variations, or intermediate states, along the nanotube, particularly at the location of the domain wall. These variations suggest that the domain wall in this field range is not fully axial or azimuthal, hinting at a possible tilted state. In such a state, the nanotube's magnetisation is neither fully aligned with the tube's length nor fully circumferential but instead forms a hybrid configuration.
The nanotubes transitioned to a saturated axial magnetisation when subjected to fields exceeding $+36$ mT parallel to the tube axis. In this state, all the magnetic domains within the nanotube are aligned parallel to the tube's length, indicating the nanotube's pure axial magnetisation. Additionally, different values in nm.T at different locations and fields were quantified based on the Aharanov-Bohm effect in the case of axial magnetisation. These values represent the in-plane magnetic induction times the specimen thickness. The higher value in nm.T means the higher axial component of the magnetisation compared to the azimuthal one.
An important consideration in this experiment is the application of a transverse component of the magnetic field. The presence of a lateral field could potentially perturb the uniformity of the axial magnetisation, leading to a more complex magnetisation pattern. This could create unique spatial magnetisation profiles within the nanotubes and possibly affect the magnetisation switching process. Moreover, a 20-degree tilt in the sample was incorporated into the experimental setup. This tilt could introduce an angular bias in the phase images, requiring careful interpretation to accurately deduce the magnetisation state. This tilt could also lead to varying local magnetic fields experienced by different parts of the nanotube due to the geometrical asymmetry. Such variations could, in turn, induce a more intricate magnetisation pattern within the nanotubes and potentially shed more information on the observed states and domain wall, as present in the following section.
One of our primary goals was to identify the optimal experimental conditions for achieving the highest coherence and good signal quality in electron holography. This was particularly crucial given the significant thickness of the nanotube (more than 100 nm the specimen thickness), which presents challenges for obtaining high-quality data, especially in Lorentz mode. Further analysis of the obtained results points to several intricate details of the magnetisation states and the domain

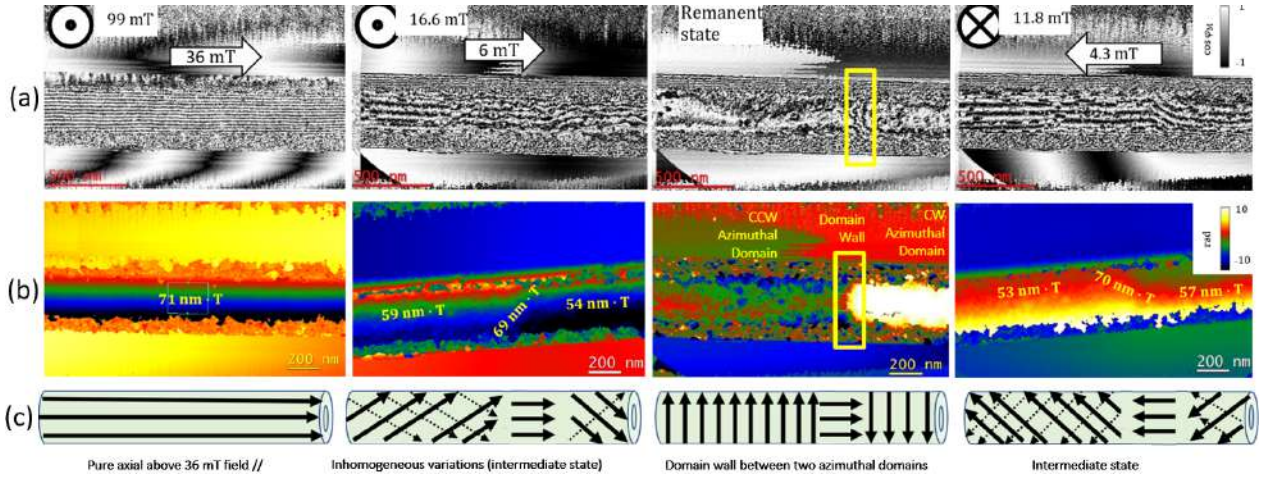

Figure 5.10: Electron holography analysis of CoNiB nanotubes (thickness: 60 nm, length: 30 µm, diameter: 470 nm) under varying axial and transverse magnetic fields (in mT), displaying (a) the cosine of the phase images, (b) the phase images, and (c) the anticipated magnetic configurations. The remanent state reveals a distinct domain wall between two azimuthal domains (highlighted in yellow). Magnetisation switching is observed between -4.3 mT and $+6$ mT fields parallel to the tube axis, accompanied by inhomogeneous variations (intermediate states) along the tube at the domain wall location. This suggests the domain wall is neither fully axial nor azimuthal at smaller fields. Axial magnetisation saturation is achieved at fields exceeding $+36$ mT parallel to the tube axis. Different values in nm.T at different locations and fields were quantified based on the Aharanov-Bohm effect. These values represent the magnetic induction times the specimen thickness.

wall dynamics in the CoNiB nanotubes. For instance, the observed inhomogeneous variations along the tube at smaller fields, particularly around the domain wall location, allude to the complex magnetisation processes involved. This may be indicative of an onion state, a magnetic configuration where opposing azimuthal magnetisations are separated by a central axial domain wall but with a high component of the transverse magnetisation due to the transverse applied magnetic fields component. The presence of such an onion state might offer a pathway for controlled magnetisation switching at the nanoscale, which is particularly significant for applications in spintronic devices. It's noteworthy that the onion state is a metastable state and can be transformed to other states (*e.g.*, vortex or single domain state) under the influence of external magnetic fields. As in this case, the onion state (the intermediate state) at smaller fields transfer to the domain wall at the remanent state, and the pure axial state above 36 mT field parallel to the tube axis.
As we mentioned earlier, the tilt of the sample introduced an additional layer of complexity in the data interpretation. The associated angular bias might have resulted in an overestimation or underestimation of the magnetisation components along different directions. Therefore, a more meticulous analysis, possibly involving corrections for this tilt angle, would be essential for an accurate representation of the magnetisation states. Moreover, by considering the tilt of the sample into account, the type of the domain wall will be solved and clarified.
Further scrutiny of the domain wall, which seems to play a pivotal role in the observed magnetic behaviour, could be useful. Its nature, whether it's of the Neel or Bloch type, its size and dynamics under the influence of applied fields could have significant implications on the magnetisation processes in these nanotubes. In light of these observations, the adoption of advanced micromagnetic simulations might provide a more comprehensive understanding of the observed magnetic phenomena. Such further investigations could help in understanding the domain wall characteristics in these nanotubes, ultimately enabling their effective utilization in various nanomagnetic applications.
In conclusion, the electron holography analysis of CoNiB nanotubes has revealed important features of their complex magnetic behaviour, such as the existence of distinct magnetisation states and domain walls. We have seen the first experimental evidence of a domain wall in long tubes by electron holography. Further investigations could focus on manipulating these magnetic states dynamically, providing an exciting opportunity for active control of nanoscale magnetisation. In the following section, we will discuss the type and size of the discovered domain wall combined with a comparison with micromagnetic simulation.

5.4.3 Domain wall type and width

Néel walls are more theoretically likely to be found in cylindrical nanotubes with azimuthal magnetic domains. This can be attributed to the inherent geometry of these nanostructures and the nature of the magnetisation orientation.
When the orientation of magnetic vectors needs to change in cylindrical nanotubes with azimuthal domains, such as in a domain wall, the system aims to minimize the magnetic energy. In this respect, Néel walls are favoured, as they allow magnetisation vectors to rotate in the plane of the nanotube, thereby following its natural curve and maintaining the minimized magnetic energy state. Bloch walls, on the other hand, require the magnetisation vectors to rotate out of the plane of the nanotube. This arrangement is less energetically favourable in the context of cylindrical nanotubes, as it would induce a greater amount of magnetic energy into the system. Hence, Bloch's walls are not completely ruled out.

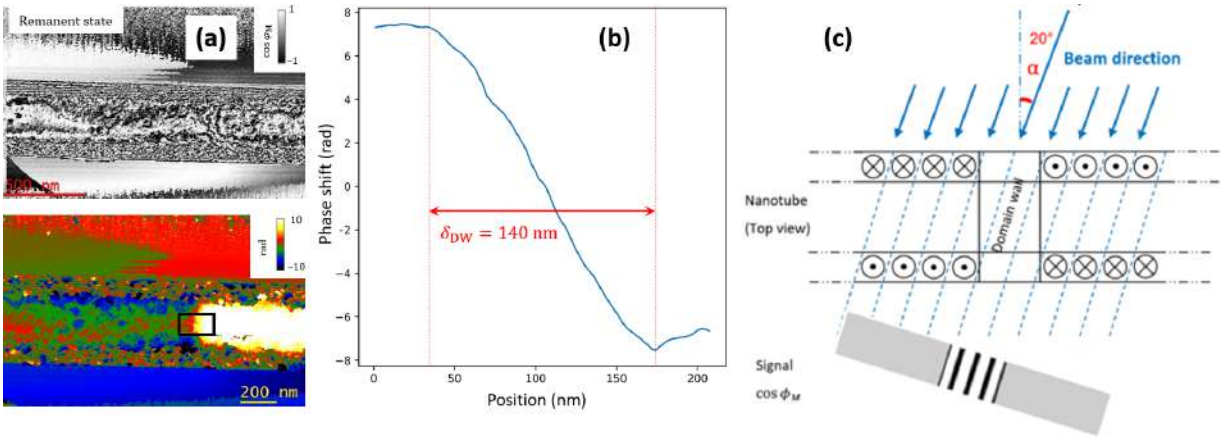

Figure 5.11: (a) The domain wall at remanent state showing phase shift signal parallel to the tube axis, indicating unexpected transverse magnetization direction unless accounting for a 20-degree tilt in the nanotube. The square selection represents a profile selection at the domain wall location. (b) Profile plot selected in (a), revealing a domain wall width δ_{DW} of approximately 140 nm. (c) Schematic illustration demonstrating how considering the nanotube tilt can alter the detected signal of the cosine of the magnetic phase shift.

This study presents compelling findings on the unique characteristics of a domain wall in a cylindrical nanotube. Notably, at the remanent state, the domain wall shows a phase shift signal parallel to the tube axis, indicating an unanticipated transverse magnetization direction. Theoretically, this observation is not anticipated unless a 20-degree tilt in the nanotube's orientation is taken into account. A square selection marked in the image indicates the exact location of the domain wall, thus offering a detailed look at the magnetic state within this region. A subsequent profile plot of the chosen area uncovers the width of the domain wall, denoted as δ_{DW}, which measures approximately 140 nanometers (Figure 5.11). This data provides valuable quantitative insight into the spatial extent of magnetic transitions within the nanotube. Further, we offer a schematic illustration that underlines the significant influence of the nanotube's tilt on the detected signal from the cosine of the magnetic phase shift (Figure 5.11.c). The transverse component of the magnetization arises as a result of the summation of the axial component at the domain wall location and the azimuthal one near the domain wall location, leading to a resultant transverse magnetization component.

The behaviour of magnetic domain walls within cylindrical CoNiB nanotubes, particularly in this case with a wall thickness of 60 nm and a diameter of 470 nm, provides significant insight into the nanotube's magnetic characteristics. The width of the Néel domain wall, where magnetisation vectors rotate in the plane of the wall, is chiefly influenced by the exchange stiffness and circumferential magnetic anisotropy of the CoNiB nanotube. Given the cylindrical geometry of the nanotube, the Néel wall's width can be relatively small, typically in the range of 10 to 120 nm, due to magnetisation vectors aligning with the tube's circumference, thereby minimising magnetic energy. Conversely, a Bloch wall, in which the magnetisation vectors rotate out of the plane of the wall, requires more energy due to the out-of-plane magnetisation rotation, potentially leading to larger domain wall widths compared to a Néel wall.

Notably, the theoretically anticipated domain wall width may not always correspond with experimental results due to various factors, such as the tilt of the nanotube and the material's intrinsic properties. The nanotube in the present study was tilted at 20°, which could potentially distort

the measurement of the domain wall width as observed in electron holography phase images, introducing an out-of-plane component to the magnetic signal. The Néel domain wall width in our experiment was about 140 nm. However, this value was affected by the 20° tilt of the nanotube. Without the tilt, the domain wall width would be smaller, around 100-120 nm. However, to accurately determine the domain wall width, we need to use micromagnetic simulation.
In the study of magnetic domain walls in nanotubes, micromagnetic simulations have proven to be an indispensable tool in predicting and analysing the complex magnetic configurations that arise [8]. These simulations provide a detailed picture of the magnetisation configurations and the expected phase contrast of the magnetic domain walls within the nanotube. This analysis becomes particularly valuable when examining the distinctive characteristics of Néel and Bloch walls. In a Néel wall, micromagnetic simulations typically show a dipolar variation in the magnetic phase signal at the location of the domain wall (Figure 5.12.c). This signature is exhibited as a two-colour variation, with the colours representing the magnetisation direction and strength. The contrasting colours denote the transition of the magnetization vectors across the domain wall, indicating the 'flip' from one magnetic domain to another. This dipolar variation aligns well with the theoretical expectation for a Néel wall where the in-plane rotation of the magnetization vectors minimises the magnetic energy and provides a clear, distinct transition in the phase contrast signal.
On the other hand, Bloch walls present a more complex picture in micromagnetic simulations. Due to the out-of-plane rotation of magnetization vectors in Bloch walls, a quadrupolar variation in the phase contrast signal is typically observed due to the quadrupolar nature of the magnetic charges (Figure 5.12.b). This signal presents itself as a four-colour variation in the phase contrast, reflecting the more intricate rotation of magnetisation vectors. The quadrupolar variation provides a visual representation of the magnetisation rotation out of the plane of the wall and back into the plane as you move across the Bloch wall. Furthermore, this quadrupolar variation in phase contrast also has implications for the magnetic energy within the Bloch wall. The out-of-plane rotation in the Bloch wall requires more energy compared to the in-plane rotation in the Néel wall. As we did not perform micromagnetic simulations of the electron holography data, we consider the same micromagnetic simulations software used by our team (FeeLLGood) and considered by Stano in his thesis [8].
Finally, it's important to note that micromagnetic simulations hold significant relevance due to the inherent three-dimensional nature of cylindrical nanotubes. In these systems, the magnetic configurations are fundamentally three-dimensional, extending through the full volume of the nanotube (Figure 5.12.a). However, experimental phase images often only provide a two-dimensional representation, capturing a 'slice' of the magnetization configurations. This discrepancy presents a unique challenge in interpreting experimental data, as the two-dimensional images may not fully capture the complexity of the three-dimensional magnetic configurations within the nanotube. Micromagnetic simulations are invaluable in this regard as a critical tool in translating these two-dimensional phase images into three-dimensional magnetic configurations.

5.5 Conclusion and outlook

Throughout this chapter, we explored the magnetic domain walls in ferromagnetic CoNiB nanotubes. Our exploration primarily leveraged high-resolution electron microscopy techniques, particularly electron holography, supplemented by synchrotron-based STXM. These investigative methods allowed us to delve deep into the magnetic properties of the nanotubes, providing a compre-

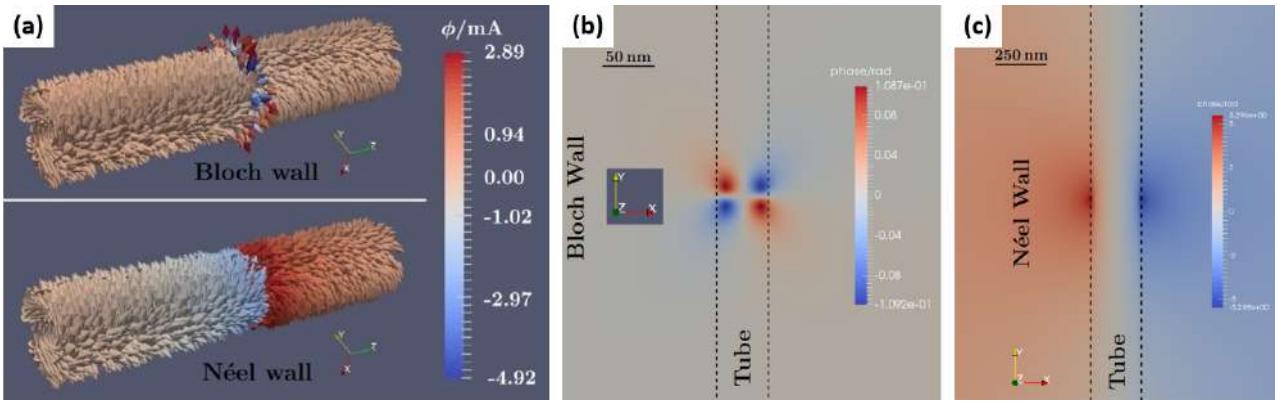

Figure 5.12: (a) represents a 3D micromagnetic model of a nanotube illustrating two opposing azimuthal domains, separated by both a Bloch and a Néel wall. The model serves as a detailed demonstration of the magnetic configuration within the tube, providing a clear visualization of the different domain walls. (b) and (c) display the results from electron holography simulations of the magnetic phase maps for Bloch and Néel walls, respectively, positioned between two opposite azimuthal domains within the nanotube. The simulations conducted for the Bloch wall, as shown in (b), were performed on a tube with reduced dimensions, resulting in a distinct contrast range. Notably, the phase contrast in the Bloch wall simulation is substantially diminished, approximately six times weaker than that of the Néel wall under analogous geometric conditions, as illustrated in (c). This variance, in contrast, is a critical factor when examining and comparing these two unique types of domain walls. This simulation and the images are adapted from [8].

hensive perspective of their domain wall structure and dynamics. Both techniques were applied by using analytical models to fit the experimental data and extract essential parameters, such as the absorption coefficients, the dichroism, the deviation angle between axial and azimuthal and the in-plane magnetic induction.

Our experimental evidence presented a clear picture of magnetic domain walls in these ferromagnetic CoNiB nanotubes. The interplay of the Néel and Bloch domain walls, identified in these structures, was of particular interest. We found that the Néel wall, with its theoretical expectation, was manifest in these nanotubes, demonstrating the role of nanoscale confinement and system dimensionality in dictating magnetic behaviour.

The domain wall width was another aspect of our focus. Our findings, particularly the measured domain wall width in a tilted nanotube, underscored the importance of understanding the influence of external factors, like tilt, in such measurements. This discovery emphasizes the need for further experimental and computational analyses for accurate characterisation of nanoscale magnetic phenomena.

Through electron holography simulations, we examined the magnetic phase maps of Bloch and Néel walls in nanotubes, highlighting the substantial contrast difference between the two. The simulations, however, also underlined the challenges in imaging 3D magnetic configurations and translating them into 2D representations, and vice versa.

Looking ahead, our research opens multiple avenues for exploration. While we have begun to understand the behaviour of domain walls in nanotubes, many questions remain. How does the magnetic behaviour evolve with variations in the geometry, composition, or external conditions like temperature and applied magnetic field? How can we improve our imaging techniques to

better capture and interpret the nanoscale magnetic phenomena?

Chapter 6

General conclusion and perspectives

6.1 General conclusion and perspectives (English)

6.1.1 Conclusion

This thesis explored the multifaceted exploration of CoNiB ferromagnetic nanotubes, combining thorough investigations into their structural and magnetic properties. The primary objective was to deepen our understanding of 3D nanomagnetism and unlock potential applications in solid-state, low-power memory systems. The chapters of this thesis built a comprehensive outlook on the challenges and potentialities of studying nanoscale magnetic phenomena, explaining the interplay between curvature effects and core-shell interfaces in these nanotubes.

Chapter 2, “Theoretical background and state of the art” laid the groundwork by explaining the fundamental principles, the unique features and applications of magnetic nanotubes. This introductory exploration was instrumental in comprehending the results investigated in the succeeding chapters.

Chapter 3, "Methods and Instrumentation," delved into the experimental techniques pivotal to investigating nanotubes, including TEM, STEM, off-axis electron holography, STXM, EDX, and EELS. Understanding these techniques’ capabilities and limitations was crucial for interpreting the data accurately and drawing reliable conclusions.

Chapter 4, "Structural and Chemical Analysis of Nanotubes," emphasized the importance of precise measurements for nanotubes and the implications of compositional heterogeneities, as demonstrated by the detected boron segregation. The chapter underscored the value of accurate determinations in paving the way for a comprehensive understanding of other parameters, thereby enhancing our overall comprehension of nanomaterials.

Chapter 5, "Magnetic Imaging of CoNiB Ferromagnetic Nanotubes," provided groundbreaking insights into the landscape of magnetic domain walls in ferromagnetic CoNiB nanotubes. Through cutting-edge electron microscopy techniques, primarily electron holography and synchrotron-based STXM, we furnished the first experimental evidence of these domain walls. We identified the interplay between Néel and Bloch domain walls, which highlighted the influence of nanoscale confinement and system dimensionality on magnetic behaviour. We also noted how external factors, like tilt, affect the measurements of the domain wall width, emphasizing the necessity for continual refinement of our experimental and computational methods.

This thesis also involved magnetic flux mapping and quantification during magnetic reversal, establishing a field requirement for axial magnetization. The application of smaller fields demonstrated domain wall transformations, motion, and partial magnetization rotation along the nanotube axis.

These findings were cross-verified using micromagnetic modelling translated into phase images, contributing to our holistic understanding of the nature and width of domain walls.

While significant strides were made in understanding ferromagnetic nanotubes, the path forward involves the further refinement of methodologies and revealing how variations in geometry, composition, or external conditions, such as temperature and applied magnetic field, influence magnetic behaviour. This will necessitate not only technological advancements but also innovative approaches to accurately capture and interpret nanoscale magnetic phenomena.

Looking ahead, the knowledge obtained through this thesis has vast implications for practical applications, especially in advancing technologies like magnetic memory devices and spintronics. As we delve deeper into understanding these nanomagnetic phenomena, they will be pivotal in shaping the future of nanotechnology. Our research journey to date has been a stepping stone towards unravelling the complexities of nanomagnetic phenomena, and there is still much to explore and understand in the exciting world of nanomagnetism.

6.1.2 Perspectives

The results of this thesis and the understanding garnered about CoNiB ferromagnetic nanotubes and their magnetic properties set a firm foundation for several research directions, especially the first expedited evidence of the domain wall in a long tube that can be used in applications (As usually long tubes are needed for application instead of the short nanorings used in many other studies). Future work on this topic could focus on different perspectives that are worthy of attention.

Firstly, the investigation of 3D magnetic configurations could be significantly enhanced by using other advanced investigative techniques, such as holography tomography. This technique could provide a comprehensive three-dimensional overview of the sample, allowing for a more in-depth study of the azimuthal domains. The wealth of information obtained from this analysis could improve our understanding of the intricacies of the 3D nanomagnetic phenomena.

Secondly, our focus so far has primarily been on static analysis, evaluating the variation of magnetic configuration at different fields. However, studying the dynamics and the propagation of spin waves in the nanotube system could be equally enlightening. The speed of domain wall motion is an essential factor in understanding the overall behaviour of the magnetic system. A time-resolved study of this high-speed domain wall motion could unravel dynamic properties that are critical to the nanotubes' potential practical applications.

Thirdly, an essential step to enhance the understanding and visualization of the magnetic phenomena in these nanotubes would be to perform micromagnetic simulations of the magnetic phase images obtained from electron holography. This approach could allow us to translate 3D magnetic configurations into 2D magnetic phase images and vice versa. This simulation could also consider various specific conditions, such as the tilting of the sample during holography, adding more depth and precision to our understanding of the nanotubes' magnetic properties.

Lastly, a crucial aspect for future study is the exploration of the potential application of these ferromagnetic nanotubes in spintronic applications. This could range from their potential use in magnetic sensors to their incorporation into magnetic racetrack memories. This promising area needs further exploration and development. The distance to practical implementation of these devices in the market might still be large, but every step of research brings us closer to that goal.

6.2 Conclusion générale et perspectives (Français)

6.2.1 Conclusion

Cette thèse a exploré les multiples facettes des nanotubes ferromagnétiques CoNiB, combinant des investigations approfondies de leurs propriétés structurelles et magnétiques. L'objectif principal était d'approfondir notre compréhension du nanomagnétisme en 3D et d'ouvrir la voie à des applications potentielles dans les systèmes de mémoire à faible consommation d'énergie et à l'état solide. Les chapitres de cette thèse ont construit de manière synergique une vision globale des défis et des potentialités de l'étude des phénomènes magnétiques à l'échelle nanométrique, en éclairant l'interaction entre les effets de courbure et les interfaces cœur-coquille dans ces nanotubes.
Chapitre 2, "Contexte théorique et état de l'art", a jeté les bases en expliquant les principes fondamentaux, les caractéristiques uniques et les applications des nanotubes magnétiques. Cette exploration introductive a été essentielle pour comprendre les résultats étudiés dans les chapitres suivants.
Le chapitre 3, "Méthodes et Instrumentation", a exploré les techniques expérimentales essentielles à l'étude des nanotubes, y compris TEM, STEM, holographie électronique hors-axe, STXM, EDX et EELS. Comprendre les capacités et les limites de ces techniques était crucial pour interpréter les données avec précision et tirer des conclusions fiables.
Le chapitre 4, "Analyse Structurelle et Chimique des Nanotubes", a souligné l'importance des mesures précises pour les nanotubes et les implications des hétérogénéités compositionnelles, comme démontré par la ségrégation de bore détectée. Le chapitre a souligné l'importance de leur détermination précise pour permettre la compréhension globale d'autres paramètres, améliorant ainsi notre compréhension générale des nanomatériaux.
Le chapitre 5, "Imagerie Magnétique des Nanotubes Ferromagnétiques CoNiB", a fourni des informations sur les parois de domaines magnétiques dans les nanotubes ferromagnétiques CoNiB. Grâce à des techniques de microscopie électronique de pointe, principalement l'holographie électronique et le STXM basé sur le rayonnement synchrotron, nous avons fourni la première preuve expérimentale de la structure de ces parois de domaine. Nous avons identifié l'interaction entre les parois de domaine de Néel et de Bloch, mettant en évidence l'influence de la confinement nanométrique et de la dimensionnalité du système sur le comportement magnétique. Nous avons également noté comment les facteurs externes, comme l'inclinaison du tube durant l'imagerie, affectent les mesures de la largeur de la paroi de domaine, soulignant la nécessité d'un affinement continu de nos méthodes expérimentales et computationnelles.
Cette thèse a également impliqué la cartographie et la quantification du flux magnétique pendant le renversement d'aimantation, déterminant le champ de saturation pour l'aimantation axiale. L'application de champs plus petits a montré des transformations de parois de domaine, des mouvements, et une rotation partielle de l'aimantation le long de l'axe du nanotube. Ces résultats ont été vérifiés par modélisation micromagnétique traduite en images de phase, contribuant à notre compréhension globale de la nature et de la largeur des parois de domaine.
Bien que des progrès significatifs aient été réalisés dans la compréhension des nanotubes ferromagnétiques, la voie à suivre implique un affinement supplémentaire des méthodologies et l'approfondissement de l'influence des variations de géométrie, de composition, ou des conditions externes, comme la température et le champ magnétique appliqué, sur le comportement magnétique. Cela nécessitera non seulement des avancées technologiques, mais aussi des approches innovantes pour capter et interpréter avec précision les phénomènes magnétiques à l'échelle nanométrique.

En regardant vers l'avenir, les connaissances acquises grâce à cette thèse ont de vastes implications pour les applications pratiques, en particulier dans l'avancement des technologies comme les dispositifs de mémoire magnétique et la spintronique. Alors que nous approfondissons notre compréhension de ces phénomènes nanomagnétiques, ils seront essentiels pour façonner l'avenir de la nanotechnologie. Notre parcours de recherche jusqu'à présent a constitué un passage important pour comprendre la complexité des phénomènes nanomagnétiques, et il reste encore beaucoup à explorer et à comprendre dans le monde passionnant du nanomagnétisme.

6.2.2 Perspectives

Les résultats de cette thèse et la compréhension acquise sur les nanotubes ferromagnétiques CoNiB et leurs propriétés magnétiques constituent une base solide pour plusieurs orientations de recherche, en particulier la première étude du déplacement des parosi de domaine dans un long tube, qui peut être utilisée dans les applications (car habituellement, ce sont les longs tubes qui sont nécessaires pour les applications, plutôt que les courts nanorings utilisés dans de nombreuses autres études). Les travaux futurs sur ce sujet pourraient se concentrer sur différentes perspectives qui méritent attention.

Premièrement, l'investigation des configurations magnétiques 3D pourrait être significativement améliorée en utilisant d'autres techniques d'investigation avancées, comme la tomographie holographique. Cette technique pourrait fournir un aperçu tridimensionnel complet de l'échantillon, permettant une étude plus approfondie des domaines azimutaux. La richesse des informations obtenues à partir de cette analyse pourrait améliorer notre compréhension des subtilités des phénomènes nanomagnétiques en 3D.

Deuxièmement, notre focus jusqu'à présent a été principalement sur l'analyse statique, évaluant la variation de la configuration magnétique sous différents champs statiques. Cependant, l'étude de la dynamique et de la propagation des ondes de spin dans le système de nanotubes pourrait être tout aussi éclairante. La vitesse de déplacement de la paroi de domaine est un facteur essentiel pour comprendre le comportement global du système magnétique. Une étude résolue en temps de ce mouvement rapide de la paroi de domaine pourrait révéler des propriétés dynamiques qui sont cruciales pour les applications pratiques potentielles des nanotubes.

Troisièmement, une étape essentielle pour améliorer la compréhension et la visualisation des phénomènes magnétiques dans ces nanotubes serait de réaliser des simulations micromagnétiques des images de phase magnétique obtenues par holographie électronique. Cette approche pourrait nous permettre de traduire les configurations magnétiques 3D en images de phase magnétique 2D et vice versa. Cette simulation pourrait également prendre en compte diverses conditions spécifiques, comme l'inclinaison de l'échantillon pendant l'holographie, ajoutant plus de précision à notre compréhension des propriétés magnétiques des nanotubes.

Enfin, un aspect crucial pour les études futures est l'exploration de l'application potentielle de ces nanotubes ferromagnétiques dans les applications spintroniques. Cela pourrait aller de leur utilisation potentielle dans les capteurs magnétiques à leur incorporation dans les mémoires à défilement re registre. Ce domaine prometteur nécessite une exploration et un développement supplémentaires. La distance à parcourir pour une mise en œuvre pratique de ces dispositifs sur le marché pourrait encore être grande, mais chaque étape de la recherche nous rapproche de cet objectif.

Appendix A

The calculation of the density of materials

A.1 Appendix A: Density Calculation of CoNiB Nanotubes

The accurate determination of material density is a crucial aspect of material characterization, given its influence on a wide range of physical and mechanical properties. For polycrystalline alloys, the density notably affects mechanical strength, thermal conductivity, and electrical resistivity. In this appendix, we present an estimation of the density of polycrystalline CoNiB nanotubes based on their atomic fractions, denoted as x_B, x_{Ni}, and x_{Co}. These atomic fractions represent the proportion of each atom type in the alloy and have been determined from the EDX and EELS measurements to be 20%, 32%, and 48% for B, Ni, and Co, respectively (Chapter 4, section 4.3.2). This calculation employs the rule of mixtures for ideal mixtures and serves as an essential first step towards the complete material characterization and determination of the thickness based on the density value.
The formula to calculate the density of the material is:

$$\rho = \frac{\sum_i (m_i \cdot V_i)}{V} \tag{A.1}$$

Where ρ is the density of the material, m_i is the mass of the i-th constituent element, V_i is the volume of the i-th constituent element, and V is the total volume of the material.
Before proceeding with the calculation, it is vital to define a few parameters. The atomic weights of Boron (B), Nickel (Ni), and Cobalt (Co) are denoted as A_B, A_{Ni}, and A_{Co}, and are 10.81 g/mol, 58.69 g/mol, and 58.93 g/mol, respectively. The elemental densities, denoted as ρ_B, ρ_{Ni}, and ρ_{Co}, represent the mass of one cubic centimetre ($1\,cm^3$) of each element, given in grams per cubic centimetre (g/cm^3). The respective values for B, Ni, and Co are $2.34\,g/cm^3$, $8.90\,g/cm^3$, and $8.86\,g/cm^3$. With these parameters defined, we can now proceed to the density calculation.
The mass and volume fractions are calculated based on the assumption of an ideal mixture:

1. Convert the atomic fractions into mass fractions:

$$m_B = \frac{x_B \cdot A_B}{x_B \cdot A_B + x_{Ni} \cdot A_{Ni} + x_{Co} \cdot A_{Co}} = 0.046$$
$$m_{Ni} = \frac{x_{Ni} \cdot A_{Ni}}{x_B \cdot A_B + x_{Ni} \cdot A_{Ni} + x_{Co} \cdot A_{Co}} = 0.315$$
$$m_{Co} = \frac{x_{Co} \cdot A_{Co}}{x_B \cdot A_B + x_{Ni} \cdot A_{Ni} + x_{Co} \cdot A_{Co}} = 0.639$$

2. Compute the volume fractions:

$$V_{\mathrm{B}} = \frac{m_{\mathrm{B}}/\rho_{\mathrm{B}}}{m_{\mathrm{B}}/\rho_{\mathrm{B}} + m_{\mathrm{Ni}}/\rho_{\mathrm{Ni}} + m_{\mathrm{Co}}/\rho_{\mathrm{Co}}} = 0.205$$
$$V_{\mathrm{Ni}} = \frac{m_{\mathrm{Ni}}/\rho_{\mathrm{Ni}}}{m_{\mathrm{B}}/\rho_{\mathrm{B}} + m_{\mathrm{Ni}}/\rho_{\mathrm{Ni}} + m_{\mathrm{Co}}/\rho_{\mathrm{Co}}} = 0.365$$
$$V_{\mathrm{Co}} = \frac{m_{\mathrm{Co}}/\rho_{\mathrm{Co}}}{m_{\mathrm{B}}/\rho_{\mathrm{B}} + m_{\mathrm{Ni}}/\rho_{\mathrm{Ni}} + m_{\mathrm{Co}}/\rho_{\mathrm{Co}}} = 0.430$$

3. Finally, the overall density is obtained by combining these quantities:

$$\rho_{\mathrm{total}} = \frac{m_{\mathrm{B}} + m_{\mathrm{Ni}} + m_{\mathrm{Co}}}{V_{\mathrm{B}} + V_{\mathrm{Ni}} + V_{\mathrm{Co}}} = 7.90 \pm 0.5\,\mathrm{g/cm^3}$$

In conclusion, the estimated density of the polycrystalline CoNiB nanotubes, based on the given atomic fractions, atomic weights, and elemental densities, is $7.90 \pm 0.5\,\mathrm{g/cm^3}$ approximately. This estimation serves as a preliminary figure and might not precisely reflect the true density, given the various factors influencing this property, including atomic packing, grain boundary distribution, and the presence of any defects or impurities. The deviation between the estimated and the actual density could reach up to 5-10%.

A more precise determination of density could be achieved through experimental methods like X-ray diffraction for obtaining detailed crystal structure and atomic spacing information, as well as transmission electron microscopy for nano-scale structural characterisation. In addition, computational approaches such as density functional theory (DFT) can be utilized for theoretical predictions and validations. The most accurate determination of density would likely emerge from a combination of experimental measurements and theoretical computations.

Appendix B

The calculation of the XAS profile function

In this appendix, we provide a detailed presentation of the XAS function calculation, as briefly outlined in the main text (Section 5.2.1.2). It was shown that the relative logarithmic intensity of XAS $\log\frac{I(x)}{I_0}$, in the absence of magnetic consideration, can be formulated as:

$$\log\frac{I(x)}{I_0}=\begin{cases}-2\mu_x\left[\mathrm{R}\sin\left(\arccos\left(\frac{x}{\mathrm{R}}\right)\right)-\mathrm{r}\sin\left(\arccos\left(\frac{x}{\mathrm{r}}\right)\right)\right], & \text{if } |x|<\mathrm{R}-t\\ 2\mu_x\mathrm{r}\sin\left(\arccos\left(\frac{x}{\mathrm{r}}\right)\right), & \text{if } \mathrm{R}-t\leq|x|<\mathrm{R}\\ 0, & \text{if } |x|\geq\mathrm{R}\end{cases} \tag{B.1}$$

Furthermore, we revisited the concept of magnetisation in azimuthal domains of nanotubes, encompassing three key components: m_x, m_y, and m_z. Each of these components is defined as a function of the deviation angle θ_{azi} and the azimuthal angle ϕ_{azi}. As discussed in the main text, the magnetisation of these domains can be written as:

$$\begin{cases}m_x=\sin\theta_{\mathrm{azi}}\sin\phi_{\mathrm{azi}}\\ m_y=\sin\theta_{\mathrm{azi}}\cos\phi_{\mathrm{azi}}\\ m_z=\cos\theta_{\mathrm{azi}}\end{cases} \tag{B.2}$$

Furthermore, we have seen that when considering azimuthal domains, the absorption coefficient μ varies and is best expressed as $\mu(x,y)$. This implies that the beam's progressive absorption within a material is accounted for by integrating the absorption rate, which depends on the position, across each small segment of length dl, as proposed by Jamet et al. [139]:

$$I_X^{\pm}=I_0\exp\left\{-\int_{\mathrm{P_{in}}}^{\mathrm{P_{out}}}dl\left[\frac{1}{2}\mu_+\left(1\pm\mathbf{k}\cdot\mathbf{m}\right)+\frac{1}{2}\mu_-\left(1\mp\mathbf{k}\cdot\mathbf{m}\right)\right]\right\} \tag{B.3}$$

The energy and helicity dependency of absorption coefficients for left and right circularly polarized X-rays, μ_+ and μ_-, respectively, were considered in the main text formula. This formula also considers the magnetisation direction in the sample, with $\mathbf{k}$ representing the unit vector along the beam's propagation direction. For clarity, $\mathbf{k}=-\mathbf{y}$ and $dl=dy$ in our case. Hence, $\mathbf{k}\cdot\mathbf{m}$ equals $\sin\theta_{\mathrm{azi}}\cdot\cos\phi_{\mathrm{azi}}$, with $\phi_{\mathrm{azi}}=\arctan\left(\frac{y}{x}\right)$ and $\cos\left(\arctan\left(u\right)\right)=\frac{1}{\sqrt{1+u^2}}$. Therefore, we present the following equation:

$$\mathbf{k}\cdot\mathbf{m}=\sin\left(\theta_{\mathrm{azi}}\right)\frac{x}{\sqrt{x^2+y^2}} \tag{B.4}$$

Therefore, We have noted that the equation B.4 can be reformatted as follows:

$$I_X^{\pm} = I_0 \exp\{-\mu_x \cdot t(x)\} \times \exp\left\{ \pm \frac{\Delta\mu_x}{2} \sin(\theta_{\text{azi}}) \int_{\text{P}_{\text{in}}}^{\text{P}_{\text{out}}} \frac{x}{\sqrt{x^2+y^2}} dy \right\} \tag{B.5}$$

Where $\mu_x = \frac{\mu_+ + \mu_-}{2}$ and $\Delta\mu_x = \mu_+ - \mu_-$.
To solve the integral $\int \frac{1}{\sqrt{x^2+y^2}} dy$, we can use the definition of the inverse hyperbolic sine function, $\arg\sinh(x) = \ln\left(x + \sqrt{x^2+1}\right)$, which give the solution of the integral, as $\int \frac{1}{\sqrt{x^2+y^2}} dy = \arg\sinh\left(\frac{y}{|x|}\right)$. Therefore, the equation B.5 becomes:

$$I_X^{\pm} = I_0 \exp\{-\mu_x \cdot t(x)\} \times \exp\left\{ \pm \sin(\theta_{\text{azi}}) \frac{\Delta\mu_x}{2} x \cdot \arg\sinh\left(\frac{y}{|x|}\right)_{\text{P}_{\text{in}}}^{\text{P}_{\text{out}}} \right\} \tag{B.6}$$

A new function $G^{\pm}(x)$ is introduced to incorporate the chirality aspect and simplify the analysis.

$$G^{\pm}(x) = \pm \sin(\theta_{\text{azi}}) \frac{\Delta\mu_x}{2} x \cdot \arg\sinh\left(\frac{y}{|x|}\right)_{\text{P}_{\text{in}}}^{\text{P}_{\text{out}}} = \pm G(x) \tag{B.7}$$

The value of $\arg\sinh\left(\frac{y}{|x|}\right)_{\text{Pin}}^{\text{P}_{\text{out}}}$ can be defined based on the value of x. By using the identity $\cosh(x) = \frac{\exp(u)+\exp(-u)}{2}$, the XAS profile intensity can be expressed as:

$$I_{\text{XAS}} = \frac{I^+ + I^-}{2} = I_0 \exp\left\{-\mu_x \cdot t(x)\right\} \times \frac{1}{2}\left\{\exp[G(x)] + \exp[-G(x)]\right\} = I_0 \exp\left\{-\mu_x \cdot t(x)\right\} \times \cosh[G(x)] \tag{B.8}$$

By examining various values of x, the XAS intensity function can be expressed as follows:

$$I_{\text{XAS}} = \begin{cases} I_0 \exp\left\{-2\mu_x\left(\sqrt{R^2-x^2} - \sqrt{r^2-x^2}\right)\right\} \cdot \cosh\left\{\sin(\theta_{\text{azi}}) \cdot x \cdot \Delta\mu_x \left[\arg\sinh\left(\frac{\sqrt{R^2-x^2}}{|x|}\right) - \arg\sinh\left(\frac{\sqrt{r^2-x^2}}{|x|}\right)\right]\right\}, & \text{if } 0 < |x| \le \text{R} - t \\ I_0 \exp\left\{-2\mu_x\sqrt{R^2-x^2}\right\} \cdot \cosh\left\{\sin(\theta_{\text{azi}}) \cdot x \cdot \Delta\mu_x \left[\arg\sinh\left(\frac{\sqrt{R^2-x^2}}{|x|}\right)\right]\right\}, & \text{if R} - t < |x| \le \text{R} \\ I_0 \exp(-2(R-r)\mu_x), & \text{if } |x| = 0 \\ 0, & \text{if } |x| > \text{R} \end{cases} \tag{B.9}$$

This equation (B.9) encapsulates the XAS cross-section profile function, characterising the X-ray intensity as it traverses a nanotube with a variable x. This equation, pivotal to our discussions, will be applied in the main text (Section 5.2.1.2). The explorations undertaken in this appendix serve to deepen our understanding and interpretation of the calculations and theories put forth in the main body of the text.

Bibliography

[1] Liu Chang, Min Wang, Lei Liu, Siwei Luo, Pan Xiao, and Hycorelle Co. A brief introduction to giant magnetoresistance. Cornell Univ., ArXiv. /abs/1412.7691, 2014.

[2] Puja Dey and Jitendra Nath Roy. Tunnelling magnetoresistance (TMR). In Puja Dey and Jitendra Nath Roy, editors, Spintronics: Fundamentals and Applications, pages 103–125. Springer, 2021.

[3] D. C. Ralph and M. D. Stiles. Spin transfer torques. J. Magn. Magn. Mater., 320(7):1190–1216, 2008.

[4] J. E. Hirsch. Spin hall effect. Phys. Rev. Lett., APS, 83(9):1834–1837, 1999.

[5] Jairo Sinova, Sergio O. Valenzuela, J. Wunderlich, C.H. Back, and T. Jungwirth. Spin hall effects. Rev. Mod. Phys., APS, 87(4):1213–1260, 2015.

[6] K. Uchida, S. Takahashi, K. Harii, J. Ieda, W. Koshibae, K. Ando, S. Maekawa, and E. Saitoh. Observation of the spin seebeck effect. Nature, 455(7214):778–781, 2008.

[7] Stuart S. P. Parkin, Masamitsu Hayashi, and Luc Thomas. Magnetic domain-wall racetrack memory. Science, 320(5873):190–194, 2008.

[8] Michal Staňo. Magnetic microscopy of domains and domain walls in ferromagnetic nanotubes. PhD thesis, Université Grenoble Alpes, 2017.

[9] M. Staňo, S. Schaefer, A. Wartelle, M. Rioult, R. Belkhou, A. Sala, T. O. Menteş, A. Locatelli, L. Cagnon, B. Trapp, S. Bochmann, S. Martin, E. Gautier, J.-C. Toussaint, W. Ensinger, and O. Fruchart. Flux-closure domains in high aspect ratio electroless-deposited CoNiB nanotubes. SciPost Phys., 5(4):038, 2018.

[10] R. Hertel. Ultrafast domain wall dynamics in magnetic nanotubes and nanowires. J. Phys.: Condens. Matter, 28(48):483002, 2016.

[11] Denys Makarov and Denis D. Sheka. Curvilinear micromagnetism: From fundamentals to applications, 2022. Springer.

[12] Amalio Fernández-Pacheco, Robert Streubel, Olivier Fruchart, Riccardo Hertel, Peter Fischer, and Russell P. Cowburn. Three-dimensional nanomagnetism. Nature Communications, 8(1):15756, 2017.

[13] Michal Staňo and Olivier Fruchart. Magnetic nanowires and nanotubes. In Handbook of Magnetic Materials, volume 27, pages 155–267. Elsevier, 2018.

[14] M. P. Proenca, C. T. Sousa, J. Escrig, J. Ventura, M. Vazquez, and J. P. Araujo. Magnetic interactions and reversal mechanisms in co nanowire and nanotube arrays. Journal of Applied Physics, 113(9):093907, 2013.

[15] M. Poggio. 17 - determining magnetization configurations and reversal of individual magnetic nanotubes. In Manuel Vázquez, editor, Magnetic Nano- and Microwires (Second Edition), Woodhead Publishing Series in Electronic and Optical Materials, pages 491–517. 2020.

[16] J. M. D. Coey. Magnetism and Magnetic Materials. Cambridge University Press, 2010.

[17] Stephen Blundell. Magnetism in Condensed Matter. Oxford University Press, 2001.

[18] Carmen-Gabriela Stefanita. Magnetism: Basics and Applications. Springer, 2012.

[19] André Thiaville and Yoshinobu Nakatani. Domain-wall dynamics in nanowiresand nanostrips. In Burkard Hillebrands and André Thiaville, editors, Spin Dynamics in Confined Magnetic Structures III, Topics in Applied Physics, pages 161–205. Springer, 2006.

[20] S. Jamet, N. Rougemaille, J. C. Toussaint, and O. Fruchart. 25 - head-to-head domain walls in one-dimensional nanostructures: An extended phase diagram ranging from strips to cylindrical wires. In Manuel Vázquez, editor, Magnetic Nano- and Microwires, Woodhead Publishing Series in Electronic and Optical Materials, pages 783–811. Woodhead Publishing, 2015.

[21] Yoshinobu Nakatani, André Thiaville, and Jacques Miltat. Head-to-head domain walls in soft nano-strips: a refined phase diagram. Journal of Magnetism and Magnetic Materials, 290-291:750–753, 2005.

[22] Michael Schöbitz. Current-induced of magnetic bloch-point domain wall dynamics in cylindrical nanowires. PhD thesis, Université Grenoble Alpes, 2021.

[23] Peter Fischer, Dédalo Sanz-Hernández, Robert Streubel, and Amalio Fernández-Pacheco. Launching a new dimension with 3d magnetic nanostructures. APL Materials, 8(1):010701, 2020.

[24] Frank Hagelberg. Magnetism in Carbon Nanostructures. Cambridge University Press, 2017.

[25] Riccardo Hertel. Computational micromagnetism of magnetization processes in nickel nanowires. J. Magn. Magn. Mater., 249(1):251–256, 2002.

[26] S. Da Col, S. Jamet, N. Rougemaille, A. Locatelli, T. O. Mentes, B. Santos Burgos, R. Afid, M. Darques, L. Cagnon, J. C. Toussaint, and O. Fruchart. Observation of bloch-point domain walls in cylindrical magnetic nanowires. Phys. Rev. B, 89(18):180405, 2014.

[27] P. Landeros and Álvaro S. Núñez. Domain wall motion on magnetic nanotubes. Journal of Applied Physics, 108(3):033917, 2010.

[28] Riccardo Hertel. Curvature-induced magnetochirality. SPIN, World Scientific Publishing Co., 03(3):1340009, 2013.

[29] D. Letellier, O. Sandre, C. Ménager, V. Cabuil, and M. Lavergne. Magnetic tubules. Materials Science and Engineering: C, 5(2):153–162, 1997.

[30] K. Žužek Rožman, D. Pečko, S. Šturm, U. Maver, P. Nadrah, M. Bele, and S. Kobe. Electrochemical synthesis and characterization of fe70pd30 nanotubes for drug-delivery applications. Materials Chemistry and Physics, 133(1):218–224, 2012.

[31] Chen Sun and Valery L. Pokrovsky. Magnetic properties of a long, thin-walled ferromagnetic nanotube. Journal of Magnetism and Magnetic Materials, 355:121–130, 2014.

[32] Marcus Wyss. Nanoscale magnetic imaging of ferromagnetic nanostructures. PhD thesis, University of Basel, 2018.

[33] J. Escrig, P. Landeros, D. Altbir, and E. E. Vogel. Effect of anisotropy in magnetic nanotubes. Journal of Magnetism and Magnetic Materials, 310(2):2448–2450, 2007.

[34] J. Escrig, P. Landeros, D. Altbir, E. E. Vogel, and P. Vargas. Phase diagrams of magnetic nanotubes. Journal of Magnetism and Magnetic Materials, 308(2):233–237, 2007.

[35] P. Landeros, S. Allende, J. Escrig, E. Salcedo, D. Altbir, and E. E. Vogel. Reversal modes in magnetic nanotubes. Appl. Phys. Lett., 90(10):102501, 2007.

[36] P. Landeros, O. J. Suarez, A. Cuchillo, and P. Vargas. Equilibrium states and vortex domain wall nucleation in ferromagnetic nanotubes. Phys. Rev. B, 79(2):024404, 2009.

[37] Jehyun Lee, Dieter Suess, Thomas Schrefl, Kyu Hwan Oh, and Josef Fidler. Magnetic characteristics of ferromagnetic nanotube. Journal of Magnetism and Magnetic Materials, 310(2):2445–2447, 2007.

[38] M. Wyss, A. Mehlin, B. Gross, A. Buchter, A. Farhan, M. Buzzi, A. Kleibert, G. Tütüncüoglu, F. Heimbach, A. Fontcuberta i Morral, D. Grundler, and M. Poggio. Imaging magnetic vortex configurations in ferromagnetic nanotubes. Phys. Rev. B, 96(2):024423, 2017.

[39] Riccardo Hertel and Jürgen Kirschner. Magnetic drops in a soft-magnetic cylinder. Journal of Magnetism and Magnetic Materials, 278(3):L291–L297, 2004.

[40] Z. K. Wang, H. S. Lim, H. Y. Liu, S. C. Ng, M. H. Kuok, L. L. Tay, D. J. Lockwood, M. G. Cottam, K. L. Hobbs, P. R. Larson, J. C. Keay, G. D. Lian, and M. B. Johnson. Spin waves in nickel nanorings of large aspect ratio. Phys. Rev. Lett., APS, 94(13):137208, 2005.

[41] A. P. Chen, N. A. Usov, J. M. Blanco, and J. Gonzalez. Equilibrium magnetization states in magnetic nanotubes and their evolution in external magnetic field. Journal of Magnetism and Magnetic Materials, 316(2):e317–e319, 2007.

[42] A. P. Chen, K. Y. Guslienko, and J. Gonzalez. Magnetization configurations and reversal of thin magnetic nanotubes with uniaxial anisotropy. Journal of Applied Physics, 108(8):083920, 2010.

[43] Ai-Ping Chen, Julian M. Gonzalez, and Konstantin Y. Guslienko. Magnetization configurations and reversal of magnetic nanotubes with opposite chiralities of the end domains. Journal of Applied Physics, 109(7):073923, 2011.

[44] Denis D. Sheka, Oleksandr V. Pylypovskyi, Pedro Landeros, Yuri Gaididei, Attila Kákay, and Denys Makarov. Nonlocal chiral symmetry breaking in curvilinear magnetic shells. Commun. Phys., Nature Publishing Group, 3(1):1–7, 2020.

[45] A. Buchter, J. Nagel, D. Rüffer, F. Xue, D. P. Weber, O. F. Kieler, T. Weimann, J. Kohlmann, A. B. Zorin, E. Russo-Averchi, R. Huber, P. Berberich, A. Fontcuberta i Morral, M. Kemmler, R. Kleiner, D. Koelle, D. Grundler, and M. Poggio. Reversal mechanism of an individual ni nanotube simultaneously studied by torque and SQUID magnetometry. Phys. Rev. Lett., APS, 111(6):067202, 2013.

[46] Dongdong Li, Richard S. Thompson, Gerd Bergmann, and Jia G. Lu. Template-based synthesis and magnetic properties of cobalt nanotube arrays. Advanced Materials, 20(23):4575–4578, 2008.

[47] Michael Zimmermann, Thomas Norbert Gerhard Meier, Florian Dirnberger, Attila Kákay, Martin Decker, Sebastian Wintz, Simone Finizio, Elisabeth Josten, Jörg Raabe, Matthias Kronseder, Dominique Bougeard, Jürgen Lindner, and Christian Horst Back. Origin and manipulation of stable vortex ground states in permalloy nanotubes. Nano Lett., 18(5):2828–2834, 2018.

[48] J. A. López-López, D. Cortés-Ortuño, and P. Landeros. Role of anisotropy on the domain wall properties of ferromagnetic nanotubes. Journal of Magnetism and Magnetic Materials, 324(13):2024–2029, 2012.

[49] N. A. Usov, A. Zhukov, and J. Gonzalez. Domain walls and magnetization reversal process in soft magnetic nanowires and nanotubes. Journal of Magnetism and Magnetic Materials, 316(2):255–261, 2007.

[50] Julien Bachmann, Juan Escrig, Kristina Pitzschel, Josep M. Montero Moreno, Jing Jing, Detlef Görlitz, Dora Altbir, and Kornelius Nielsch. Size effects in ordered arrays of magnetic nanotubes: Pick your reversal mode. Journal of Applied Physics, 105(7):07B521, 2009.

[51] S. Allende, J. Escrig, D. Altbir, E. Salcedo, and M. Bahiana. Angular dependence of the transverse and vortex modesin magneticnanotubes. Eur. Phys. J. B, 66(1):37–40, 2008.

[52] Ole Albrecht, Robert Zierold, Sebastián Allende, Juan Escrig, Christian Patzig, Bernd Rauschenbach, Kornelius Nielsch, and Detlef Görlitz. Experimental evidence for an angular dependent transition of magnetization reversal modes in magnetic nanotubes. Journal of Applied Physics, 109(9):093910, 2011.

[53] S. Allende and R. Arias. Transverse domain wall propagation in modulated cylindrical nanostructures and possible geometric control. Phys. Rev. B, 83(17):174452, 2011.

[54] Daeyeon Lee, Robert E. Cohen, and Michael F. Rubner. Heterostructured magnetic nanotubes. Langmuir, American Chemical Society, 23(1):123–129, 2007.

[55] I. Betancourt, G. Hrkac, and T. Schrefl. Micromagnetic simulation of domain wall dynamics in permalloy nanotubes at high frequencies. Journal of Applied Physics, 104(2):023915, 2008.

[56] Robert Streubel, Jehyun Lee, Denys Makarov, Mi-Young Im, Daniil Karnaushenko, Luyang Han, Rudolf Schäfer, Peter Fischer, Sang-Koog Kim, and Oliver G. Schmidt. Magnetic microstructure of rolled-up single-layer ferromagnetic nanomembranes. Advanced Materials, 26(2):316–323, 2014.

[57] Vlad-Andrei Antohe, Emeline Nysten, Juan Manuel Martínez-Huerta, Pedro Miguel Pereira de Sá, and Luc Piraux. Annealing effects on the magnetic properties of highly-packed vertically-aligned nickel nanotubes. RSC Adv., 7(30):18609–18616, 2017.

[58] M. P. Proenca, J. Ventura, C. T. Sousa, M. Vazquez, and J. P. Araujo. Angular first-order reversal curves: an advanced method to extract magnetization reversal mechanisms and quantify magnetostatic interactions. J. Phys.: Condens. Matter, 26(11):116004, 2014.

[59] M. P. Proenca, K. J. Merazzo, L. G. Vivas, D. C. Leitao, C. T. Sousa, J. Ventura, J. P. Araujo, and M. Vazquez. Co nanostructures in ordered templates: comparative FORC analysis. Nanotechnology, IOP Publishing, 24(47):475703, 2013.

[60] Jose Angel Fernandez-Roldan, Dieivase Chrischon, Lucio Strazzabosco Dorneles, Oksana Chubykalo-Fesenko, Manuel Vazquez, and Cristina Bran. A comparative study of magnetic properties of large diameter co nanowires and nanotubes. Nanomaterials, 8(9):692, 2018.

[61] Y. Velázquez-Galván, J. M. Martínez-Huerta, J. De La Torre Medina, Y. Danlée, L. Piraux, and A. Encinas. Dipolar interaction in arrays of magnetic nanotubes. J. Phys.: Condens. Matter, 26(2):026001, 2013.

[62] Sachin Pathak, Jongill Hong, Jai Chaudhary, and Manish Sharma. Magneto-optical kerr effect characterization of electrodeposited y-junction magnetic nanostructures. Journal of Applied Physics, APS, 117(17):17A751, 2015.

[63] M. R. Tabasum, F. Zighem, J. De La Torre Medina, A. Encinas, L. Piraux, and B. Nysten. Magnetic force microscopy investigation of arrays of nickel nanowires and nanotubes. Nanotechnology, IOP Publishing, 25(24):245707, 2014.

[64] Tao Wang, Ying Wang, Fashen Li, Chongtao Xu, and Dong Zhou. Morphology and magnetic behaviour of an fe3o4 nanotube array. J. Phys.: Condens. Matter, 18(47):10545, 2006.

[65] F. S. Li, D. Zhou, T. Wang, Y. Wang, L. J. Song, and C. T. Xu. Fabrication and magnetic properties of FeCo alloy nanotube array. Journal of Applied Physics, 101(1):014309, 2007.

[66] A. Kozlovskiy, A. Zhanbotin, M. Zdorovets, I. Manakova, A. Ozernoy, K. Kadyrzhanov, and V. Rusakov. Study of ni/fe nanotube properties. Nuclear Instruments and Methods in Physics Research Section B: Beam Interactions with Materials and Atoms, 365:663–667, 2015.

[67] P Diehle, J Caron, A Kovács, J Ungermann, and R E Dunin-Borkowski. Towards electron holographic tomography of three-dimensional magnetization distributions in ferromagnetic nanotubes. Poster presented at the 3rd International Conference on Frontiers of Aberration Corrected Electron Microscopy "PICO", 2015.

[68] Daniel Rüffer, Rupert Huber, Paul Berberich, Stephan Albert, Eleonora Russo-Averchi, Martin Heiss, Jordi Arbiol, Anna Fontcuberta i Morral, and Dirk Grundler. Magnetic states of an individual ni nanotube probed by anisotropic magnetoresistance. Nanoscale, 4(16):4989–4995, 2012.

[69] K. Baumgaertl, F. Heimbach, S. Maendl, D. Rueffer, A. Fontcuberta i Morral, and D. Grundler. Magnetization reversal in individual py and CoFeB nanotubes locally probed via anisotropic magnetoresistance and anomalous nernst effect. Appl. Phys. Lett., 108(13):132408, 2016.

[70] A. Mehlin, B. Gross, M. Wyss, T. Schefer, G. Tütüncüoglu, F. Heimbach, A. Fontcuberta i Morral, D. Grundler, and M. Poggio. Observation of end-vortex nucleation in individual ferromagnetic nanotubes. Phys. Rev. B, APS, 97(13):134422, 2018.

[71] Dhananjay Tiwari, Martin Christoph Scheuerlein, Mahdi Jaber, Eric Gautier, Laurent Vila, Jean-Philippe Attané, Michael Schöbitz, Aurelien Masseboeuf, Tim Hellmann, Jan P. Hofmann, Wolfgang Ensinger, and Olivier Fruchart. Electrical characterization of the azimuthal anisotropy of (NixCo1x)b-based ferromagnetic nanotubes. Journal of Magnetism and Magnetic Materials, page 170715, 2023.

[72] César Magén, Javier Pablo-Navarro, and José María De Teresa. Focused-electron-beam engineering of 3d magnetic nanowires. Nanomaterials, 11(2):402, 2021.

[73] Mariana P. Proenca, Célia T. Sousa, João Ventura, and João P. Araújo. 6 - cylindrical magnetic nanotubes: Synthesis, magnetism and applications. In Manuel Vázquez, editor, Magnetic Nano- and Microwires (Second Edition), Woodhead Publishing Series in Electronic and Optical Materials, pages 135–184. Woodhead Publishing, 2020.

[74] S. Schaefer, E.-M. Felix, F. Muench, M. Antoni, C. Lohaus, J. Brötz, U. Kunz, I. Gärtner, and W. Ensinger. NiCo nanotubes plated on pd seeds as a designed magnetically recollectable catalyst with high noble metal utilisation. RSC Advances, 6(74):70033–70039, 2016.

[75] D. Richardson and F. M. F. Rhen. The diverse nanostructure of electroless plated CoNiFeB alloy: Thin film, nanotubes and nanoparticles. Physics Procedia, 75:1158–1166, 2015.

[76] David B. Williams and C. Barry Carter. Transmission Electron Microscopy: A Textbook for Materials Science. Springer US, 2 edition, 2009.

[77] Zhu Yimei. Springer Handbook: Modern Techniques for Characterizing Magnetic Materials. 2005.

[78] Peter W. Hawkes and John C. H. Spence. Springer Handbook of Microscopy. 2019.

[79] R. F. Egerton. Electron energy-loss spectroscopy in the TEM. Rep. Prog. Phys., IOP Publishing, 72(1):016502, 2008.

[80] M. De Graef. Magnetic imaging and its applications to Materials. Academic Press, 2001.

[81] Y. Aharonov and D. Bohm. Significance of electromagnetic potentials in the quantum theory. Phys. Rev., APS, 115(3):485–491, 1959.

[82] Y. Aharonov and D. Bohm. Further considerations on electromagnetic potentials in the quantum theory. Phys. Rev., APS, 123(4):1511–1524, 1961.

[83] Hannes Lichte and Michael Lehmann. Electron holography: basics and applications. Rep. Prog. Phys., 71(1):016102, 2007.

[84] Rafal E. Dunin-Borkowski, András Kovács, Takeshi Kasama, Martha R. McCartney, and David J. Smith. Electron holography. In Peter W. Hawkes and John C. H. Spence, editors, Springer Handbook of Microscopy, Springer Handbooks, pages 767–818. Springer International Publishing, 2019.

[85] G. Möllenstedt and H. Düker. Beobachtungen und messungen an biprisma-interferenzen mit elektronenwellen. Z. Physik, 145(3):377–397, 1956.

[86] Akira TONOMURA, Tsuyoshi MATSUDA, Junji ENDO, Hideo TODOKORO, and Tsutomu KOMODA. Development of a field emission electron microscope. Journal of Electron Microscopy, 28(1):1–11, 1979.

[87] Martin J. Hÿtch, Rafal E. Dunin-Borkowski, Michael R. Scheinfein, Johan Moulin, Cécilie Duhamel, Frédéric Mazaleyrat, and Yannick Champion. Vortex flux channeling in magnetic nanoparticle chains. Phys. Rev. Lett., APS, 91(25):257207, 2003.

[88] C. Gatel, A. Lubk, G. Pozzi, E. Snoeck, and M. Hÿtch. Counting elementary charges on nanoparticles by electron holography. Phys. Rev. Lett., APS, 111(2):025501, 2013.

[89] T. Kasama, P. Barpanda, R. E. Dunin-Borkowski, S. B. Newcomb, M. R. McCartney, F. J. Castaño, and C. A. Ross. Off-axis electron holography of pseudo-spin-valve thin-film magnetic elements. Journal of Applied Physics, 98(1):013903, 2005.

[90] Yang Yang, Nana Niu, Chao Li, Yuan Yao, Guangzhe Piao, and Richeng Yu. Electron holography characterization as a method for measurements of diameter and mean inner potential of hollow nanomaterials. Nanoscale, 4(23):7460–7463, 2012.

[91] Florian Winkler, Amir H. Tavabi, Juri Barthel, Martial Duchamp, Emrah Yucelen, Sven Borghardt, Beata E. Kardynal, and Rafal E. Dunin-Borkowski. Quantitative measurement of mean inner potential and specimen thickness from high-resolution off-axis electron holograms of ultra-thin layered WSe2. Ultramicroscopy, 178:38–47, 2017.

[92] Matthias Wanner, David Bach, Dagmar Gerthsen, Ralph Werner, and Bernd Tesche. Electron holography of thin amorphous carbon films: Measurement of the mean inner potential and a thickness-independent phase shift. Ultramicroscopy, 106(4):341–345, 2006.

[93] W. D. Rau, P. Schwander, F. H. Baumann, W. Höppner, and A. Ourmazd. Two-dimensional mapping of the electrostatic potential in transistors by electron holography. Phys. Rev. Lett., APS, 82(12):2614–2617, 1999.

[94] Martha R. McCartney, Nipun Agarwal, Suk Chung, David A. Cullen, Myung-Geun Han, Kai He, Luying Li, Hua Wang, Lin Zhou, and David J. Smith. Quantitative phase imaging of nanoscale electrostatic and magnetic fields using off-axis electron holography. Ultramicroscopy, 110(5):375–382, 2010.

[95] Martin Hÿtch, Florent Houdellier, Florian Hüe, and Etienne Snoeck. Nanoscale holographic interferometry for strain measurements in electronic devices. Nature, 453(7198):1086–1089, 2008.

[96] P. Simon, H. Lichte, P. Formanek, M. Lehmann, R. Huhle, W. Carrillo-Cabrera, A. Harscher, and H. Ehrlich. Electron holography of biological samples. Micron, 39(3):229–256, 2008.

[97] Hannah Ochner, Sven Szilagyi, Sabine Abb, Joseph Gault, Carol V. Robinson, Luigi Malavolti, Stephan Rauschenbach, and Klaus Kern. Low-energy electron holography imaging of conformational variability of single-antibody molecules from electrospray ion beam deposition. Proceedings of the National Academy of Sciences, 118(51):e2112651118, 2021.

[98] K. Aoyama and Q. Ru. Electron holographic observation for biological specimens: electron holography of bio-specimens. J. Microsc, 182:177–185, 1996.

[99] David C. Joy, Y. S. Zhang, X. Zhang, T. Hashimoto, R. D. Bunn, L. Allard, and T. A. Nolan. Practical aspects of electron holography. Ultramicroscopy, 51(1):1–14, 1993.

[100] Alex Harscher and Hannes Lichte. Experimental study of amplitude and phase detection limits in electron holography. Ultramicroscopy, 64(1):57–66, 1996.

[101] Christophe Gatel, Francisco Javier Bonilla, Anca Meffre, Etienne Snoeck, Bénédicte Warot-Fonrose, Bruno Chaudret, Lise-Marie Lacroix, and Thomas Blon. Size-specific spin configurations in single iron nanomagnet: From flower to exotic vortices. Nano Lett., ACS, 15(10):6952–6957, 2015.

[102] C. Gatel, X. Fu, V. Serin, M. Eddrief, V. Etgens, and B. Warot-Fonrose. In depth spatially inhomogeneous phase transition in epitaxial MnAs film on GaAs(001). Nano Lett., ACS, 17(4):2460–2466, 2017.

[103] Youhui Gao, Daisuke Shindo, Yuping Bao, and Kannan Krishnan. Electron holography of core-shell coCoO spherical nanocrystals. Appl. Phys. Lett., 90(23):233105, 2007.

[104] R. E. Dunin-Borkowski, M. R. Mccartney, B. Kardynal, S. S. P. Parkin, M. R. Scheinfein, and D. J. Smith. Off-axis electron holography of patterned magnetic nanostructures. Journal of Microscopy, 200(3):187–205, 2000.

[105] Rafal E. Dunin-Borkowski, Takeshi Kasama, Alexander Wei, Steven L. Tripp, Martin J. Hÿtch, Etienne Snoeck, Richard J. Harrison, and Andrew Putnis. Off-axis electron holography of magnetic nanowires and chains, rings, and planar arrays of magnetic nanoparticles. Microscopy Research and Technique, 64(5):390–402, 2004.

[106] Joshua F. Einsle, Christophe Gatel, Aurélien Masseboeuf, Robin Cours, Muhammad A. Bashir, Mark Gubbins, Robert M. Bowman, and Etienne Snoeck. In situ electron holography of the dynamic magnetic field emanating from a hard-disk drive writer. Nano Res., 8(4):1241–1249, 2015.

[107] Thibaud Denneulin, Florent Houdellier, and Martin Hÿtch. Differential phase-contrast dark-field electron holography for strain mapping. Ultramicroscopy, 160:98–109, 2016.

[108] Akira Tonomura, Tsuyoshi Matsuda, Junji Endo, Tatsuo Arii, and Kazuhiro Mihama. Holographic interference electron microscopy for determining specimen magnetic structure and thickness distribution. Phys. Rev. B, APS, 34(5):3397–3402, 1986.

[109] Etienne Snoeck and Christophe Gatel. Magnetic mapping using electron holography. In Transmission Electron Microscopy in Micro-Nanoelectronics, pages 107–134. John Wiley & Sons, Ltd, 2012.

[110] Joachim Stöhr and Hans Christoph Siegmann. Magnetism: From Fundamentals to Nanoscale Dynamics. Springer Series in Solid-State Sciences. Springer-Verlag, 2006.

[111] R. Sharif, S. Shamaila, F. Shaheen, S. Naseem, J. Y. Chen, M. Khaleeq-ur Rahman, K. Hussain, and X. F. Han. Nanotube wall thickness dependent magnetization reversal properties of NiFe nanotubes. Journal of Applied Physics, 113(2):024315, 2013.

[112] Walter Giurlani, Enrico Berretti, Massimo Innocenti, and Alessandro Lavacchi. Measuring the thickness of metal coatings: A review of the methods. Coatings, Multidisciplinary Digital Publishing Institute, 10(12):1211, 2020.

[113] Friedrich Lenz. Zur streuung mittelschneller elektronen in kleinste winkel. Zeitschrift für Naturforschung A, 9(3):185–204, 1954.

[114] R. E. Burge and G. H. Smith. A new calculation of electron scattering cross sections and a theoretical discussion of image contrast in the electron microscope. Proc. Phys. Soc., IOP Publishing, 79(4):673–690, 1962.

[115] C. E. Hall and T. Inoue. Experimental study of electron scattering in electron microscope specimens. Journal of Applied Physics, 28(11):1346–1348, 1957.

[116] Elmar Zeitler and Gunter F. Bahr. A photometric procedure for weight determination of submicroscopic particles quantitative electron microscopy. Journal of Applied Physics, 33(3):847–853, 1962.

[117] I. Pozsgai. Thickness determination by measuring electron transmission in the TEM at 200kv. Ultramicroscopy, 68(1):69–75, 1997.

[118] I. Pozsgai. Mass thickness determination and microanalysis of thin films in the TEM—revisited. Ultramicroscopy, 107(2):191–195, 2007.

[119] R. F. Egerton and S. C. Cheng. Measurement of local thickness by electron energy-loss spectroscopy. Ultramicroscopy, 21(3):231–244, 1987.

[120] T. Malis, S. C. Cheng, and R. F. Egerton. EELS log-ratio technique for specimen-thickness measurement in the TEM. Journal of Electron Microscopy Technique, 8(2):193–200, 1988.

[121] K. Iakoubovskii, K. Mitsuishi, Y. Nakayama, and K. Furuya. Thickness measurements with electron energy loss spectroscopy. Microscopy Research and Technique, 71(8):626–631, 2008.

[122] M. R. McCartney and M. Gajdardziska-Josifovska. Absolute measurement of normalized thickness, t/i, from off-axis electron holography. Ultramicroscopy, 53(3):283–289, 1994.

[123] P. M. Kelly, A. Jostsons, R. G. Blake, and J. G. Napier. The determination of foil thickness by scanning transmission electron microscopy. physica status solidi (a), 31(2):771–780, 1975.

[124] Samuel M. Allen. Foil thickness measurements from convergent-beam diffraction patterns. Philosophical Magazine A, 43(2):325–335, 1981.

[125] G. Cliff and G. W. Lorimer. The quantitative analysis of thin specimens. Journal of Microscopy, 103(2):203–207, 1975.

[126] M. Watanabe and D. B. Williams. The quantitative analysis of thin specimens: a review of progress from the cliff-lorimer to the new -factor methods. Journal of Microscopy, 221(2):89–109, 2006.

[127] G. H. Smith and R. E. Burge. A theoretical investigation of plural and multiple scattering of electrons by amorphous films, with special reference to image contrast in the electron microscope. Proc. Phys. Soc., IOP Publishin, 81(4):612–632, 1963.

[128] Huai-Ruo Zhang, Ray F. Egerton, and Marek Malac. Local thickness measurement through scattering contrast and electron energy-loss spectroscopy. Micron, 43(1):8–15, 2012.

[129] R. F. Egerton. Electron Energy-Loss Spectroscopy in the Electron Microscope. Springer Science & Business Media, 2011.

[130] Angus I. Kirkland and Sarah J. Haigh. Nanocharacterisation. Royal Society of Chemistry, 2015.

[131] S Schaefer, E.-M Felix, F Muench, M Antoni, C Lohaus, J Brötz, U Kunz, I Gärtner, and W Ensinger. Nico nanotubes plated on pd seeds as a designed magnetically recollectable catalyst with high noble metal utilisation. RSC Advances, 6:70033–70039, 2016.

[132] Shankar Dutt, Pavel Apel, Nikolay Lizunov, Christian Notthoff, Qi Wen, Christina Trautmann, Pablo Mota-Santiago, Nigel Kirby, and Patrick Kluth. Shape of nanopores in track-etched polycarbonate membranes. Journal of Membrane Science, 638:119681, 2021.

[133] P. Yu Apel, I. V. Blonskaya, S. N. Dmitriev, O. L. Orelovitch, and B. Sartowska. Structure of polycarbonate track-etch membranes: Origin of the "paradoxical" pore shape. Journal of Membrane Science, 282:393–400, 2006.

[134] D. R. G. Mitchell. Determination of mean free path for energy loss and surface oxide film thickness using convergent beam electron diffraction and thickness mapping: a case study using si and p91 steel. Journal of Microscopy, 224(2):187–196, 2006.

[135] Y. Y. Yang and R. F. Egerton. Tests of two alternative methods for measuring specimen thickness in a transmission electron microscope. Micron, 26(1):1–5, 1995.

[136] D. Rez, P. Rez, and I. Grant. Dirac–fock calculations of x-ray scattering factors and contributions to the mean inner potential for electron scattering. Acta Cryst A, International Union of Crystallography, 50(4):481–497, 1994.

[137] A. Sanchez and M. A. Ochando. Calculation of the mean inner potential. 18(1):33, 1985.

[138] E. R Kutelia, O. G Dzimtseshvili, T. A Dzigrashvili, D. M Tsivtsivadze, and P. D Kervalishvili. Determination of the mean inner potential of single-crystal lattices of boron-containing materials and its relation to the work function. Journal of the Less Common Metals, 117(1):283–286, 1986.

[139] Ségolène JAMET, Sandrine Da Col, Nicolas Rougemaille, Alexis Wartelle, Andrea Locatelli, T.O. Mentes, B. Santos Burgos, Raja Afid, Laurent Cagnon, Sebastian Bochmann, Julien Bachmann, Olivier Fruchart, and Jean-Christophe Toussaint. Quantitative analysis of shadow x-ray magnetic circular dichroism photo-emission electron microscopy. Phys. Rev. B Condens., APS, 92(14):144428, 2015.

[140] Reiko Nakajima, J. Stöhr, and Y. U. Idzerda. Electron-yield saturation effects in l-edge x-ray magnetic circular dichroism spectra of fe, co, and ni. Phys. Rev. B, APS, 59(9):6421–6429, 1999.